Summer 8-15-2013

A Study on the Structure and Photodetachment Dynamics of Copper Based Molecular Anions Using Photoelectron Spectroscopy

Nicholas Stephen Holtgrewe
Washington University in St. Louis

WASHINGTON UNIVERSITY IN ST. LOUIS

Department of Chemistry

Dissertation Examination Committee:
Richard Mabbs, Chair
Dewey Holten
Cynthia Lo
Richard Loomis
Jacob Schaefer
Yan Mei Wang

A Study on the Structure and Photodetachment Dynamics of Copper Based Molecular Anions Using Photoelectron Spectroscopy

by

Nicholas Stephen Holtgrewe

A dissertation presented to the
Graduate School of Arts and Sciences
of Washington University in
partial fulfillment of the
requirements for the degree
of Doctor of Philosophy

August 2013

St. Louis, Missouri

Table of Contents

List of Figures

List of Tables

List of Abbreviations

AEA	adiabatic electron affinity
α	Morse parameter defining curvature of potential
β	anisotropy parameter
c	speed of light in vacuum
D_e	dissociation energy (including zero point energy)
DBS	dipole bound state
DFT	density functional theory
E	energy
E_{res}	energy of resonance
EA	electron affinity
eBE	electron binding energy
eKE	electron kinetic energy
e	electronic charge
ε	laser polarization
FC	Franck-Condon
FCF	Franck-Condon factor
FWHM	full width half maximum
Γ	width of resonance / irreducible representation
HOMO	highest occupied molecular orbital
h	Planck's constant
$\hbar$	reduced Planck's constant
hν	photon energy
I	intensity
IP	ionization potential
J	total electronic angular momentum for atomic species
KE	kinetic energy
k	force constant
L	total electronic orbital angular momentum

LUMO	lowest unoccupied molecular orbital
lbe	loosely bound electron
ℓ	electronic orbital angular momentum
Λ	projection of total electronic orbital angular momentum on internuclear axis
λ	wavelength of light
M_{fi}	electric dipole matrix element
MCP	microchannel plate
MO	molecular orbital
MP2	Møller–Plesset perturbation theory (2^{nd} order)
m_e	rest mass of electron
m_ℓ	projection of angular momentum on z-axis
m_s	projection of electronic spin angular momentum
$\hat{\mu}$	dipole moment operator
μ	dipole moment
μ_{red}	reduced mass
Ω	projection of total electronic angular momentum on internuclear axis
PAD	photoelectron angular distribution
PE	potential energy
ψ	wavefunction
q	charge of particle
$R_{n\ell}$	radial wavefunction
r	bond length / distance of electron from the nucleus
r_e	equilibrium bond length
S	total electronic spin angular momentum
s	electronic spin angular momentum
Σ	projection of total electronic spin angular momentum on internuclear axis / total spin angular momentum
σ	total absorption cross section
TDDFT	time-dependent density functional theory
TOF	time-of-flight
TRPES	time-resolved photoelectron spectroscopy

t	time
τ	lifetime of temporary bound electronic resonance
θ	angle between laser polarization and electron velocity vector / angle between the dipole moment and the electron's position vector
V(r)	potential as a function of bond length
VDE	vertical detachment energy
VMI	velocity map imaging
v	velocity / vibrational quantum number
ν	photon frequency / vibrational frequency
XPES	X-ray photoelectron spectroscopy
x	displacement from the equilibrium bond length
x_e	anharmonicity constant
$Y_{\ell m_\ell}$	spherical harmonic for central potential
Z_{eff}	effective charge of the nucleus

Acknowledgments

A sincere thanks to my advisor, Professor Richard Mabbs, for taking me into his laboratory and devoting much time and commitment to develop me into the scientist I am today. I have learned an appreciable amount of information from him the past 5 years, both in the classroom and the laboratory. I certainly could not have completed this long journey had it not been for his support and belief in me.

I appreciate the financial support from Washington University, in particular the Dean's Dissertation Fellowship that provided support while writing this thesis. In addition, this work could not have been completed without the funding from the NSF (Grant CHE 0748738).

Thanks to the USC Center for Computational Studies of Electronic Structure and Spectroscopy of Open-Shell and Electronically Excited Species iopenshell facilities for allowing us to run calculations on their servers.

I would like to acknowledge my dissertation committee, Professors Richard Mabbs, Richard Loomis, Dewey Holten, Jacob Schaefer, Cynthia Lo, and Yan Mei Wang. Thank you for your time and insight.

I would especially like to thank Professor Richard Loomis for all his advice and commitment to teaching throughout my years at Washington University.

Many thanks to previous and current group members, Dr. Matthew Van Duzor, Dr. Foster Mbaiwa, Dr. Jie Wei, Josh Lasinski, and Diep Dao. Thanks for your camaraderie over the years and for all the fruitful discussions, scientific or not. In particular, thanks to Dr. Matthew Van Duzor for building the photoelectron spectroscopy instrument to run all our experiments.

Lastly, I would like to extend my sincere thanks to my supportive family and friends, for one cannot complete such a monumental achievement without their encouragement. Thanks to my parents, Stephen and Victoria, and grandparents, Cosimo, Bernice, and Marlene, for raising me into the person I am today.

To the late Bernice Catanzaro, for all those scientific newspaper clippings you used to mail me while I was studying chemistry in undergrad. In a time when email was rampant, it always put a smile on my face. Thanks for those memories.

Nicholas Stephen Holtgrewe

Washington University in St. Louis
August 2013

ABSTRACT OF THE DISSERTATION

A Study on the Structure and Photodetachment Dynamics of Copper Based Molecular Anions Using Photoelectron Spectroscopy

by

Nicholas Stephen Holtgrewe

Doctor of Philosophy in Chemistry

Washington University in St. Louis, 2013

Professor Richard Mabbs, Chair

This dissertation represents a study of the effects of electron molecule interactions in the detachment and dissociation dynamics of copper based molecular anions. Results are presented on the photodetachment of small copper oxide CuO_n^- (n = 1, 2) and copper fluoride CuF_n^- (n = 1, 2) molecular anions. Effects of different resonances are explored using the photoelectron angular distributions (PADs) and the relative intensity variations in vibrational channel cross sections. The specific resonances studied include dipole bound resonances, in which the electric dipole moment of the neutral molecule captures the outgoing electron, and electronic Feshbach resonances, in which the anion undergoes absorption to an excited anion state (lying energetically above the neutral) followed by relaxation via autodetachment into the electronic continuum. In addition to electron scattering resonances, the effects of dissociation dynamics on linear CuO_2^- are studied, wherein the linear anion isomer was found to dissociate to Cu^- fragments. This dissociation process is interpreted with experimental data acquired from nanosecond photoelectron images and a femtosecond time resolved study.

Chapter 1

Introduction

The fundamental principle of spectroscopy is the study of the interaction between light and matter. Absorption of a photon ($h\nu$) by atoms or molecules can induce a number of alterations to the system such as electronic transitions, vibrations, removal of electrons, and bond dissociations, and we can use this knowledge to study and characterize selected chemical systems. The removal of electrons by absorption of a photon and subsequent analysis of their kinetic energies is known as photoelectron spectroscopy and it can take two basic forms, photoionization and photodetachment. The former refers to electron removal from a neutral species and the latter electron removal from an anion, or negatively charged species. By definition, the ionization potential (IP) is referred to as the energy required for removal of an electron from a neutral species, and the electron affinity (EA) is the energy required for a neutral to bind an electron:

$$A^- \xrightarrow{EA} A \xrightarrow{IP} A^+ \tag{1.1}$$

The work presented in this dissertation is the result of the photodetachment from negatively charged ionic species. The use of anion photoelectron spectroscopy allows us to study neutral species in different ways that overcome limits of conventional absorption spectroscopies. In this sense, the field of anion spectroscopy provides a wealth of

information to the scientific community including molecular (anion and neutral) geometries, vibrational frequencies, EAs, anharmonicity constants, dissociation energies, etc. The purpose of this chapter is to provide the reader with information on the fundamentals of negative ion photoelectron spectroscopy providing the foundation for understanding work presented in subsequent chapters.

1.1 Photodetachment

The basic scheme for photodetachment can be seen in Equation 1.1.1:

$$A^- \xrightarrow{h\nu} A + e^- \tag{1.1.1}$$

For an anionic species to lose the electron, sufficient energy ($h\nu$) must be inputted to detach the electron. This energy barrier is known as the EA, and in anion photoelectron spectroscopy it is common to refer to the EA as the electron binding energy (eBE) of the anionic species. These two variables are related due to the conservation of energy in the form:

$$h\nu = eBE + eKE \tag{1.1.2}$$

where $h\nu = hc/\lambda$ is the photon energy of wavelength λ and frequency ν, c is the speed of light in a vacuum, and eKE is the electron kinetic energy. Due to the electron having significantly less mass that any atomic nuclei, it becomes a good approximation to assume all the excess energy from the photon absorption is converted to electronic kinetic energy for the departing electron, otherwise known as the zero recoil approximation. Figure 1.1 provides a general scheme for photodetachment from a single charged atomic anion. The anion usually starts in a ground electronic state (X), where all electrons reside in their lowest energetic orbitals, and if absorption of a photon of energy $h\nu$ exceeds the

eBE of the anion, an electron will be ejected with a specific velocity proportional to the eKE. The velocity of the outgoing photoelectron is one of the many variables used to label specific neutral electronic and vibrational states, for example, the neutral ground electronic state (X′) listed in Figure 1.1. In the non-relativistic limit, the speed of the electron is related to the energy of the electron through the well known relation: eKE = $^1/_2 m_e v^2$, where m_e is the rest mass of the ejected electron at velocity v.

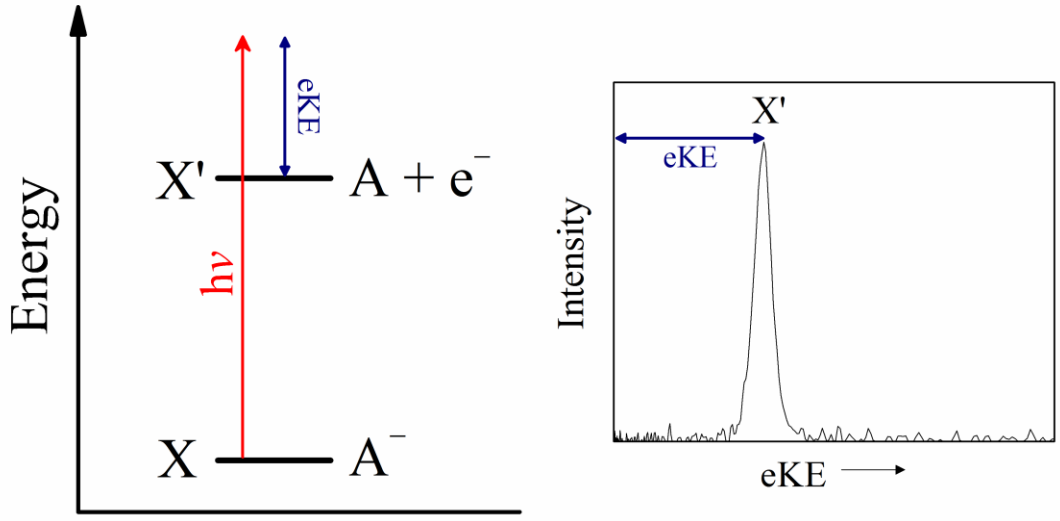

Figure 1.1: Basic energy diagram for photodetachment from an atomic anion (A^-). The anion resides in its anionic ground state (X) and upon excitation by a photon (hν) transitions to a neutral ground state (X′), whereby the photoelectron is ejected with the excess photon energy in the form of kinetic energy (eKE). The corresponding photoelectron spectrum is located to the right. It is common to label peaks in photoelectron spectra by the neutral state terminology.

1.2 Image Analysis

An example of a raw image of detachment from Cu^- and its corresponding speed distribution are shown in Figure 1.2(a). We employ the use of a velocity map imaging (VMI) arrangement [1] for detection of photoelectrons. Electrons photoejected with the same velocity vector will hit the detector at the same radial distance from the center of

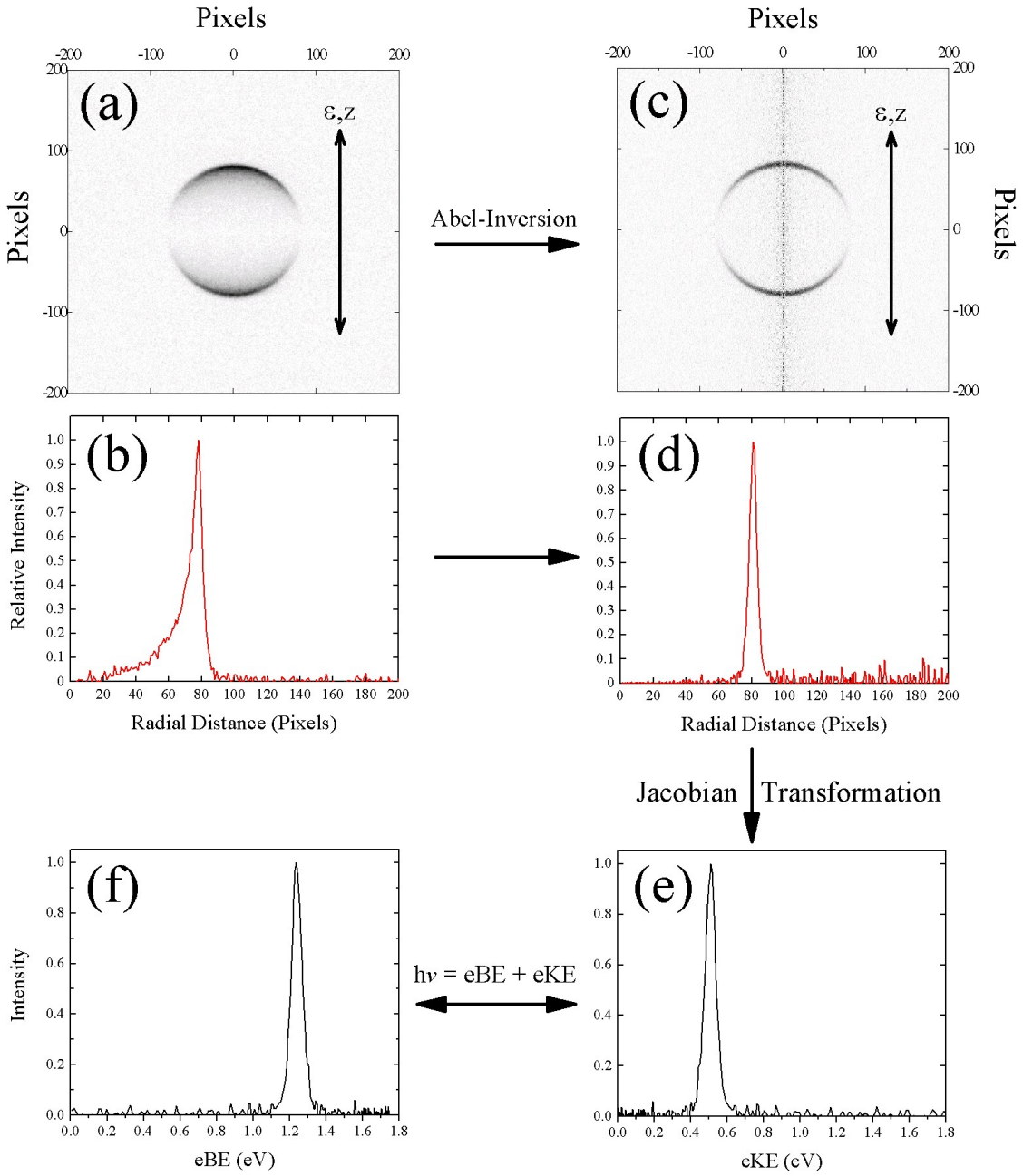

Figure 1.2: Image analysis from raw image to energy spectra: **(a)** Raw image of Cu^- at 710 nm, ε is the laser polarization aligned parallel with the lab frame z-axis. **(b)** Raw image speed distribution. **(c)** Abel-inverted reconstructed image. Image represents the central slice from the reconstructed 3-dimensional photoelectron sphere. **(d)** Reconstructed image speed distribution. **(e)** Plot of the intensity as a function of electron kinetic energy (eKE). Using the appropriate Jacobian transformation, the velocity domain from the reconstructed image can be converted to the energy domain. **(f)** Plot of the intensity as a function of electron binding energy (eBE). The eBE of Cu^- 4s orbital is 1.236 eV.

the detector, regardless of its origin within the interaction region. The concept will be explored in more detail in Chapter 2. This produces ring-like images on a two dimensional (2D) detector, from which a three dimensional (3D) momentum space distribution of electrons can be extracted through mathematical analysis.

Reconstruction of this 3D image is completed using either the algorithm of Hansen and Law [2] or the Basis Set Expansion (BASEX) program [3], which call for cylindrical symmetry about the laboratory z-axis defined by the polarization (ε) of our detachment laser beam [Figure 1.2]. The reconstructed image represents the central slice of the (newly reconstructed) 3D sphere, from which data such as energy spectra and angular profiles are extracted. An example reconstructed image and its corresponding speed distribution are shown in Figure 1.2(c,d). Through the appropriate Jacobian transformation this velocity domain can be converted into the energy domain [Figure 1.2], allowing easier interpretation in terms of neutral energy states.

1.2.1 Photoelectron Angular Distributions

The nascent photoelectron can be ejected at various angles from the laser polarization axis depending on a variety of factors. The angular profile, consisting of intensity as a function of the angle between the velocity vector and ε (I(θ)), is known as the photoelectron angular distribution (PAD). This can be a powerful tool for determination of the type of parent orbital, especially in atomic species [4,5], and also a useful detection method for electronic scattering resonances [6-9].

I(θ) for a one photon, one electron detachment process for linearly polarized light is shown in Equation 1.2.1:

$$\frac{d\sigma}{d\Omega} = I(\theta) = \frac{\sigma}{4\pi}[1 + \beta P_2(\cos\theta)] \quad (1.2.1)$$

where σ is the total absorption cross section, β is the anisotropy parameter, θ is the angle between the ejected electron velocity vector and the laser polarization, and $P_2(\cos\theta) = {}^1\!/_2(3\cos^2\theta - 1)$ is the second Legendre polynomial. For linearly polarized light β is constrained to take values between −1 and +2, indicating perpendicular or parallel polarized distributions respectively. β is also dependent on the kinetic energy of the ejected electron [5], a property that we can use to our advantage. Deviations from a parallel distribution of electrons are a result of interfering photoelectron partial waves, an effect of electron ejection from higher orbital angular momentum orbitals ($\ell \neq 0$), or resonance effects, caused by temporary anion states to be discussed in a later section.

Figure 1.3 shows the PAD for detachment from a Cu^- 4s orbital. Beginning with the reconstructed speed distribution obtained from the raw image, a radial range is selected for analysis, typically the full width half maximum (FWHM) of the selected peak, and the radially integrated intensity is monitored as a function of angle θ. This distribution can be fit with Eq. 1.2.1 and a value for β can then be extracted.

The $\cos^2\theta$ distribution in the PAD shown in Figure 1.3 can be interpreted through analysis of the electric dipole matrix element M_{fi}:

$$M_{fi} = \langle \psi_f | \hat{\mu} | \psi_i \rangle \quad (1.2.2)$$

where M_{fi} must be non-zero for a transition to occur, ψ_f and ψ_i represent the final and initial electronic wavefunctions at the moment of the transition, and $\hat{\mu} = -e\hat{r}$ is the dipole moment operator. For polarized light oriented along our laboratory frame z-axis, $\hat{\mu} = -ez$ and Eq. 1.2.2 can be rewritten as

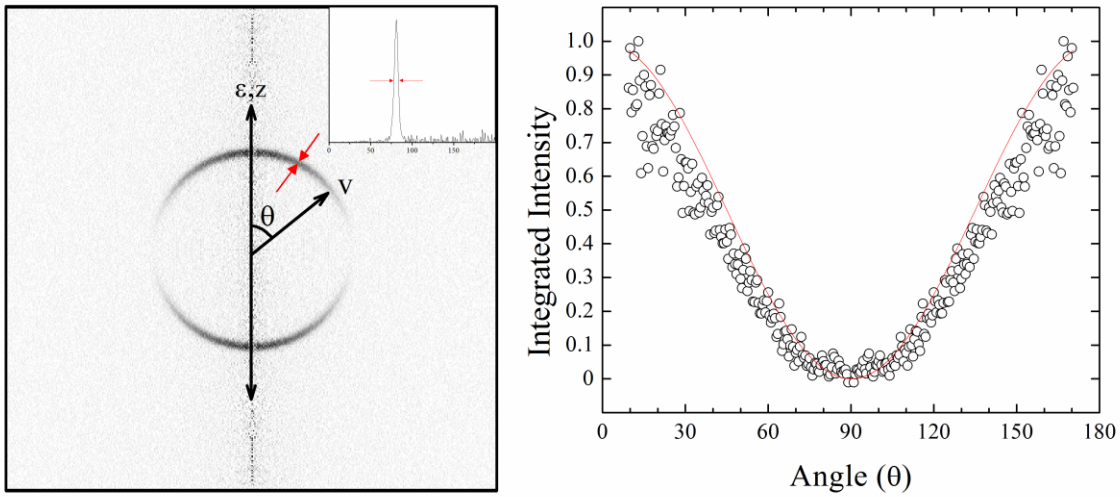

Figure 1.3: (left) Reconstructed image showing the laser polarization (ε) axis and the electron velocity vector (v), along with the angle between them (θ). Also shown is the corresponding speed distribution in the top right corner. Typical radial ranges (red arrows) are selected by using the transition peak full-width half maximum (FWHM). (right) Integrated intensity for a specific radial range (FWHM) as a function of angle θ. The $\cos^2\theta$ distribution shown as a solid red curve.

$$M_{fi} = -e \langle \psi_f | z | \psi_i \rangle \tag{1.2.3}$$

The electronic wavefunctions are characterized by quantum numbers such as orbital angular momentum (ℓ) and its projection onto the z-axis (m_ℓ). For Cu^-, the outermost electron resides in a well defined hydrogen-like 4s-orbital approximately represented by a hydrogenic (one electron) wavefunction

$$\psi_{\ell m_\ell} = R_{n\ell}(x,y,z) Y_{\ell m_\ell}(\theta,\phi) \tag{1.2.4}$$

where $R_{n\ell}(x,y,z)$ is the radial wavefunction and $Y_{\ell m_\ell}(\theta,\phi)$ is the angular function represented by a spherical harmonic for a central potential. Upon detachment the electron undergoes a transition to a free electron state, whose angular dependence however can likewise be described by spherical harmonics.

Due to conservation of angular momentum, the orbital angular momentum of the detached electron changes according to the selection rule associated with a one photon,

one electron transition, $\Delta\ell=\pm1$. Considering the case of ejection from an s-orbital, $\ell=0$, implies the outgoing electron will contain one unit of orbital angular momentum ($\ell=1$), as ℓ cannot have negative values. The projection of ℓ onto the quantization axis (m_ℓ) can take integer values between $+\ell$ and $-\ell$, making $m_\ell=\pm1,0$ for $\ell=1$; however, the linear laser polarization constrains m_ℓ to remain unchanged ($\Delta m_\ell=0$). Since the initial state of the electron has $\ell=0$, $m_\ell=0$, the final state therefore must have quantum numbers $\ell=1$, $m_\ell=0$. The spherical harmonics associated with these initial and final states are $Y_{00}(\theta,\phi)=(^1/_{4\pi})^{1/2}$ and $Y_{10}(\theta,\phi)=(^3/_{4\pi})^{1/2}\cos\theta$, respectively. The only term in both wavefunctions that is dependent on angle θ is the spherical harmonic associated with the electron's final state. The intensity distribution of the electronic transition is directly proportional to the square of the free electron wavefunction, and therefore the square of its spherical harmonic

$$I(\theta) \propto |\psi_f|^2 \propto Y_{10}(\theta,\phi) \propto \cos^2\theta \qquad (1.2.5)$$

where it is shown that the intensity has $\cos^2\theta$ dependence on electron distribution about the laser polarization axis, demonstrated by photodetachment from a Cu^- 4s orbital.

1.3 Molecular Anions

Atomic systems are useful to introduce the fundamental concepts but in order to start observing practical chemical applications we need to step beyond the simplistic single atom approach and into the realm of polyatomics. Negative ion photoelectron spectroscopy constantly deals with transitions between electronic states (neutral←anion), which differ with respect to their electronic configurations.

1.3.1 Term Symbols for Describing Polyatomic Electronic States

The one electron hydrogen atom electronic states can be well characterized by term symbols based on the electron's quantum numbers (n, ℓ, m_ℓ, s, m_s), and this terminology translates well to multi-electron atoms by description based on the total angular momentum [14] due to the reasonable nature of the Hartree Fock approximation, which averages the effect of electron-electron repulsion generating an approximate but spherically symmetric potential. As an example, take the previously discussed transition $Cu \leftarrow Cu^-$, where the Cu^- electronic state valence configuration is $3d^{10}4s^2$, described by its total spin ($S = \Sigma_i s_i = 0$) [italics will represent summation (Σ)], total orbital angular momentum ($L = \Sigma_i \ell_i = 0$), and total angular momentum ($J=|L+S|, \ldots,|L-S|= 0$) giving rise to the term symbol $^1S_0$ ($^{2S+1}L_J$). Likewise, the term symbol associated with the neutral electronic configuration from removal of a 4s electron ($3d^{10}4s^1$) is $^2S_{1/2}$ ($S=\frac{1}{2}$, $L=0$), and allows the $Cu \leftarrow Cu^-$ transition for electron detachment from the 4s orbital to be labeled by the two term symbols: $^2S_{1/2} \leftarrow {}^1S_0$.

Now let us consider a diatomic molecule, a simple case of bonding two atoms. The symmetry of the system is altered, and more pertinently the potential, dictating that these atomic quantum numbers are no longer fit to describe a diatomic with a cylindrical symmetry about its bond axis. Instead, for a cylindrically symmetric potential, the projection of the orbital (Λ), spin (Σ), and total angular momentum (Ω) on the cylindrical symmetry axis serve as labels to characterize the electronic states.

For the case of a high electric field gradient between the two nuclei, the total electronic orbital angular momentum (L) and the total electronic spin angular momentum

(S) couple separately to the internuclear axis, and L is no longer considered to be a good quantum number due to coupling with the electric field within the molecule. However, S remains a good quantum number because it is coupled by the magnetic field generated from the orbital angular momentum of the electrons, and L's projection along the internuclear axis (Λ) also remains a good quantum number. This scheme is better known as Hund's case (a) [17,18], and is only case relevant to the molecules studied in this dissertation. For such a case, the term symbols that can arise take the form $^{2S+1}\Lambda_{\Omega}$ where 2S+1 is the spin multiplicity, Λ is the projection of the total electronic orbital angular momentum on the internuclear axis, and Ω is the projection of the total angular momentum on the bond axis ($\Omega = |\Sigma + \Lambda|$). Λ is allowed to take positive integer values corresponding to the total orbital angular momentum, (i.e. $\Lambda=|\pm m_L|= m_L$) and the projection of the total spin angular momentum (Σ) is allowed to take all integer steps of the total spin angular momentum (i.e. $\Sigma = -S, \ldots, +S$). The terms used for the value of Λ are as follows: $\Lambda=0$: Σ (not to be confused with projection of total spin angular momentum), $\Lambda=1$: Π, $\Lambda=2$: Δ, etc.

As an example for diatomic and linear molecular term symbols, the ground electronic state symbols for neutral CuO will be derived from its valence configuration. The valence ground state neutral electronic configuration for CuO is $[\text{core}](3d\sigma)^2(3d\pi)^4(3d\delta)^4(2p\sigma)^2(2p\pi)^3$ which shows that there is an unpaired electron in a π-type orbital. The total orbital angular moment associated with this configuration is L=1 and its projection along the internuclear axis $\Lambda=1$, corresponding to term symbol Π. The total spin is calculated based on the number of unpaired electrons, and for this case there is one, $S=\frac{1}{2}$ $\Sigma=\pm\frac{1}{2}$, hence the spin multiplicity is $2(\frac{1}{2}) + 1 = 2$. Lastly, the total angular momentum

projected along the internuclear axis can take multiple values if both L and S are nonzero, $\Omega = |-\frac{1}{2} + 1|, |+\frac{1}{2} + 1| = \frac{1}{2}, \frac{3}{2}$. The two possible term symbols that arise for the ground electronic state of neutral CuO are $^2\Pi_{3/2}$ and $^2\Pi_{1/2}$, with $\Omega=\frac{3}{2}$ being lower in energy as defined by Hund's Rules [19]. The separation of these two states is termed the spin-orbit splitting associated with the CuO $^2\Pi$ electronic state and will be discussed more in Chapter 4.

1.3.2 Modeling Polyatomics: Potentials and Energy Levels

The simplest polyatomic species is the diatomic, two atoms either covalently or ionicly bonded by their valence electrons. A classical analogy of this diatomic molecule is two balls joined by a spring, which can be described by the combination of Newton's second law and Hooke's law:

$$\mu_{red} \frac{d^2x}{dt^2} = -kx \tag{1.3.1}$$

where μ_{red} is the reduced mass of the diatomic, t is time, k is the force constant, and x is the displacement from the equilibrium bond length with respect to the center of mass. A general solution to x(t) for a harmonic oscillator is the superposition of two waves $x(t)=A\sin(\varphi)\cos(\omega t) + A\cos(\varphi)\sin(\omega t)$ where ω is the vibrational frequency, A is the maximum displacement or amplitude of the vibration, and φ is the phase angle. It is well known that the force, emerging from displacement from equilibrium, can be expressed as the derivative of the potential energy. Within the harmonic oscillator approximation, the potential energy takes the form:

$$V(x(t)) = \frac{k}{2}(x(t))^2 \tag{1.3.2}$$

This potential works well for the classical analogy of vibration of two balls and a spring; however, this analogy fails when discussing molecular diatomics due to the quantization of the total energy. Solving the differential equation for the one-dimensional harmonic oscillator Schrödinger equation we obtain discrete vibrational energy levels for diatomic vibrations with the values:

$$E_v = h\nu\left(v + \frac{1}{2}\right) \tag{1.3.3}$$

where v (not to be confused with frequency ν) is the vibrational quantum number and takes integer values. These energy levels along with the corresponding potential energy curve are plotted in Figure 1.4 (dotted lines). Notice the energy levels are spaced by hν and that the ground vibrational level (v = 0) does not correspond to a classical value of E = V(0) = 0. There will always be residual kinetic energy, termed the zero-point energy, a result stemming from the uncertainty principle stating that both momentum and position cannot be simultaneously known. This means the error in the ground vibrational level bond lengths is open to a possible range of values, the breadth of which depends on the narrowness of the potential well.

1.3.2.1 Simple Harmonic Oscillator vs Morse Potentials

While the classical harmonic oscillator is an often reasonable approximation for molecular vibrations, it is important to point out some important differences from real anharmonic diatomic potentials. Phillip M. Morse noticed these differences as changes in the spacing between vibrational level energies, which lead him to propose the following potential [11]:

$$V(r) = D_e[1 - e^{-\alpha(r - r_e)}]^2 \tag{1.3.4}$$

as an anharmonic potential, which leads to discrete vibrational energy levels:

$$E_v = \nu_e\left(v+\frac{1}{2}\right) - x_e\nu_e\left(v+\frac{1}{2}\right)^2 + \ldots \tag{1.3.5}$$

where ν_e is the vibrational frequency in wavenumbers (cm^{-1}) and x_e is the anharmonicity constant, which is the term, along with higher ordered terms, responsible for the unequal energy level spacing for the anharmonic picture. D_e (dissociation energy), r_e (equilibrium bond length), and α (curvature of the well dependent upon ν_e and $x_e\nu_e$) are parameters dependent upon the molecule.

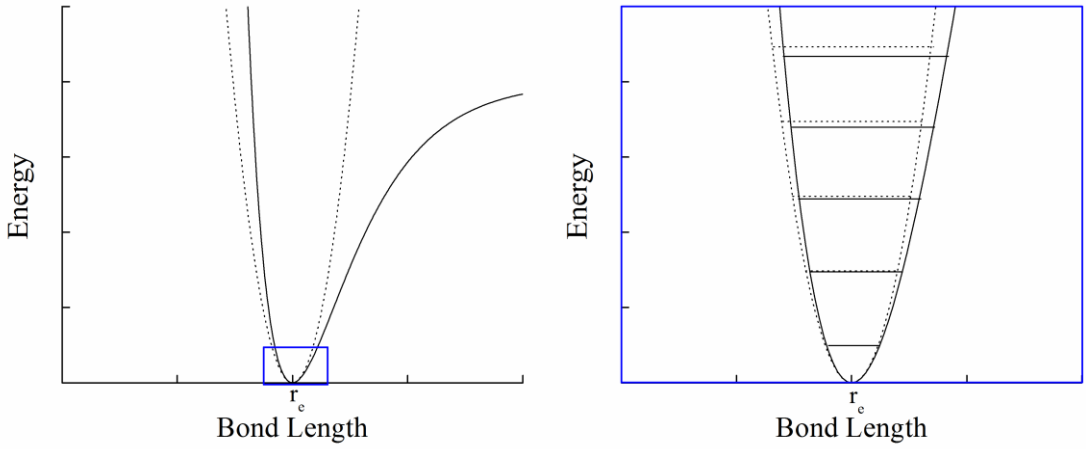

Figure 1.4: (left) Plot of potentials for a harmonic oscillator (dotted line) and an anharmonic oscillator (solid line). (right) Zoomed in region showing the base of both potential wells along with their corresponding vibrational levels. The plot shows that at low energies near the base of the potential well the harmonic approximation is very similar to the anharmonic potential.

Figure 1.4 compares the Morse potential (solid lines) for a diatomic molecule along with its corresponding energy levels as a comparison to the harmonic approximation (dotted lines). A noticeable discrepancy is observed at higher and lower bond displacements. The harmonic approximation is symmetric about the equilibrium bond length, producing an infinite energy barrier to dissociation, whereas the diatomic molecule has a steep energy curve at smaller bond distances due to nuclear-nuclear

repulsion but at higher bond lengths levels off at a certain energy, allowing bond dissociation. The introduction of anharmonicity causes the energy spacing between vibrational levels to decrease as v increases, just as Morse observed.

While the major differences between the harmonic and anharmonic schemes may seem to suggest that the harmonic approximation is a poor representation for diatomic molecules, it is important to point out that at lower energy levels in the potential energy well [Figure 1.4 (right)], the harmonic approximation is similar to the anharmonic scheme.

The Morse potential proves to be a useful tool for describing diatomic molecule potential curves, and is applicable to both neutrals and anionic species when discussing transitions between electronic states.

1.3.3 Photoelectron Transition Strengths in Polyatomics

As explained in Section 1.2.1, the probability of a transition between two electronic states induced by an oscillating electric field is proportional to the square of the transition dipole moment. For a transition between an initial and final electronic state the transition dipole moment can be represented by the integral

$$\mathrm{M_{fi}} = \int \psi'^{*} \hat{\mu} \psi \; \mathrm{d}\tau = \langle \psi' | \hat{\mu} | \psi \rangle \tag{1.3.6}$$

where $\hat{\mu}$ is the dipole moment operator and a prime indicates the final state. Loss of an electron in the initial electronic state causes rearrangement in the molecule's nuclear and electronic geometry in order to account for a rebalancing of charges under the new conditions. An important concept when discussing such geometric rearrangements is the Born-Oppenheimer approximation, which assumes that nuclear and electronic motion can

be separated, essentially suggesting the timescale for nuclear rearrangement (i.e. vibrations, rotations) is long relative to electronic redistribution [12]. Under the assumption that this approximation holds, it allows us to separate the total wavefunction for a molecule into its nuclear (vibrational) and total electronic wavefunctions.

$$\psi_{\text{total}} = \psi_{\text{v}}\psi_{\text{es}} \tag{1.3.7}$$

The square of the vibrational wavefunction $|\psi_{\text{v}}|^2$ can be understood as the probability distribution for nuclear displacement within a specific vibrational energy level. The first four Morse oscillator vibrational wavefunctions with their corresponding probability distributions are plotted in Figure 1.5.

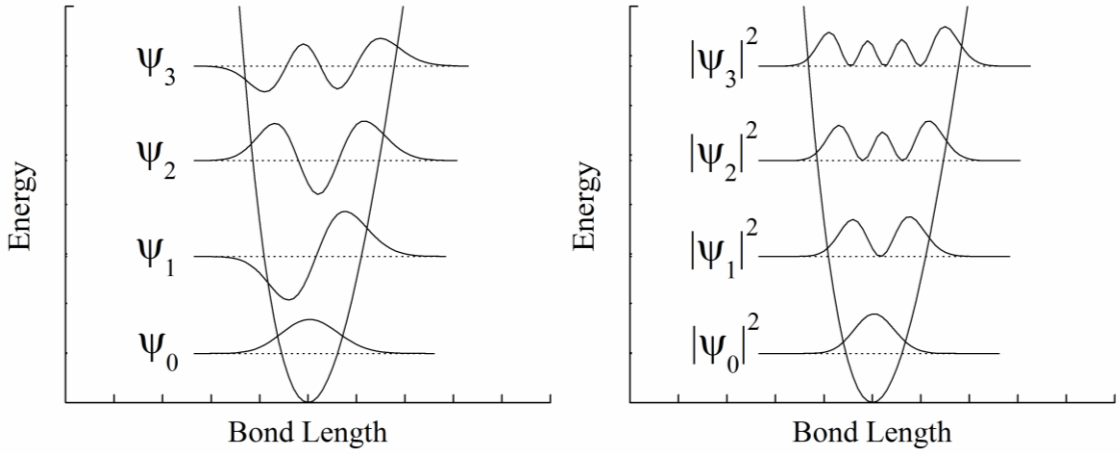

Figure 1.5: (left) The first four vibrational wavefunctions for an anharmonic oscillator. Dotted lines represent the energy of the corresponding vibrational level. (right) Their respective probability distributions.

In anion photoelectron spectroscopy, an allowed dipole transition occurs with absorption of a photon containing sufficient energy to detach the electron, however, the transition outcomes are limited by a multitude of factors. The trivial selection rule is the spin multiplicity [Section 1.3.1] of the atom or molecule must change by ±1 (i.e. the system must lose an electron for a transition to be observed). A more complex selection

rule that governs the strength of vibronic transitions is the Franck-Condon (FC) factor, arising from the vibrational component in Eq 1.3.7, which states that the probability for an electronic transition to occur is dependent on the vertical overlap between the ground and excited state vibrational wavefunctions. A pictorial representation of how FC overlap governs the intensities for vibronic transitions is displayed in Figure 1.6.

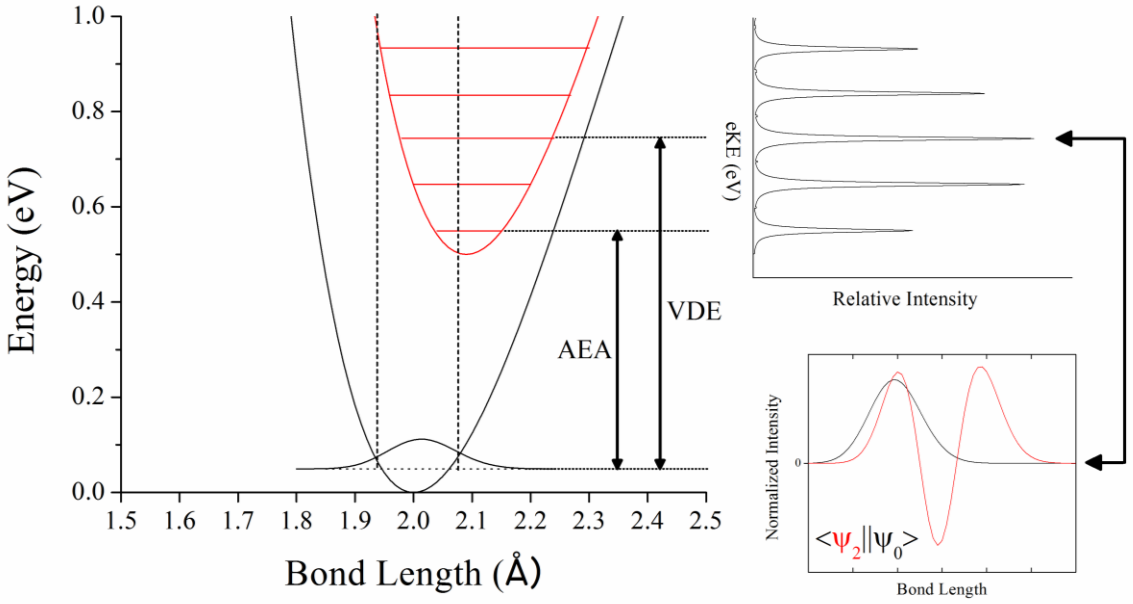

Figure 1.6: Energy diagram with a corresponding Franck-Condon (FC) energy profile. (left) Potential wells for an anion (black) and neutral (red) diatomic, where the neutral equilibrium bond length is lengthened by 0.08 Å. Vertical excitation of the anionic ground state wavefunction (ψ_0) to multiple neutral vibrational levels (horizontal red solid lines) is represented by a FC window (vertical dotted lines), which display the most probable neutral vibrational levels accessed by vertical excitation. (top right) Simulated Franck-Condon profile, with small convolution, for excitation above the neutral ground state. The most probable transition in the FC profile is the vertical detachment energy (VDE), in this case the v'=2 ← v=0 transition. (bottom right) The overlap between the two vibrational wavefunctions for the v'=2 ← v=0 transition. This provides a visual representation for good overlap between the neutral (ψ_2) and anion (ψ_0) wavefunctions, making the FC factor greatest for this specific transition.

Making use of the Born-Oppenheimer approximation in Eq. 1.3.7 and separating the dipole moment operator into its nuclear and electronic components we have

$$\mathrm{M_{fi}} = \langle \psi_{\mathrm{v'}} \psi_{\mathrm{es'}} | \hat{\mu}_{\mathrm{n}} + \hat{\mu}_{\mathrm{e}} | \psi_{\mathrm{v}} \psi_{\mathrm{es}} \rangle \tag{1.3.8}$$

$$\mathrm{M_{fi}} = \langle \psi_{\mathrm{v'}} \psi_{\mathrm{es'}} | \hat{\mu}_{\mathrm{n}} | \psi_{\mathrm{v}} \psi_{\mathrm{es}} \rangle + \langle \psi_{\mathrm{v'}} \psi_{\mathrm{es'}} | \hat{\mu}_{\mathrm{e}} | \psi_{\mathrm{v}} \psi_{\mathrm{es}} \rangle \tag{1.3.9}$$

where $\hat{\mu}_n$ and $\hat{\mu}_e$ are the nuclear and electronic dipole operators. The integrals are separable because the dipole moment operators only depend on their respective nuclear or electronic coordinates. They can further be reduced to the integrals

$$\mathrm{M_{fi}} = \langle \psi_{\mathrm{es'}} \| \psi_{\mathrm{es}} \rangle \langle \psi_{\mathrm{v'}} | \hat{\mu}_{\mathrm{n}} | \psi_{\mathrm{v}} \rangle + \langle \psi_{\mathrm{v'}} \| \psi_{\mathrm{v}} \rangle \langle \psi_{\mathrm{es'}} | \hat{\mu}_{\mathrm{e}} | \psi_{\mathrm{es}} \rangle \tag{1.3.10}$$

The first term on the right-hand side of the equation falls to zero because the two electronic wavefunctions ψ_{es} are orthogonal to each other. The important part of this equation lies in the secondary term on the right-hand side, where the vibrational integral does not have to equal zero because the two vibrational wavefunctions are not eigenfunctions of the same Hamiltonian, hence they are not necessarily orthogonal to each other. Therefore the transition moment becomes

$$\mathrm{M_{fi}} = \langle \psi_{\mathrm{v'}} \| \psi_{\mathrm{v}} \rangle \langle \psi_{\mathrm{es'}} | \hat{\mu}_{\mathrm{e}} | \psi_{\mathrm{es}} \rangle \tag{1.3.11}$$

and the probability for a transition

$$\mathrm{M_{fi}}^2 = \langle \psi_{\mathrm{v'}} \| \psi_{\mathrm{v}} \rangle^2 \langle \psi_{\mathrm{es'}} | \hat{\mu}_{\mathrm{e}} | \psi_{\mathrm{es}} \rangle^2 \tag{1.3.12}$$

where $\langle \psi_{v'} \| \psi_{v} \rangle^2$ is known as the FC factor and it becomes clear that, during the instantaneous transition, the probability, and likewise the intensity of the transition, depends on the vertical overlap of the initial vibrational level wavefunction ψ_v and final vibrational level wavefunction $\psi_{v'}$. The right hand integral contains the foundation for orbital and spin angular momentum selection rules.

During ion production in our experiments, vibrationally cold anions are prepared and it is a good approximation to assume the majority of our anions start in the ground vibrational level ($\psi_v = \psi_0$). An example of the ground state wavefunction overlapped with an excited state wavefunction is shown in Figure 1.6, where the overlapped area represents the quantity of the integral.

Two important terms associated with electronic transitions are the vertical detachment energy (VDE) and the adiabatic electron affinity (AEA), also shown in Figure 1.6. VDE represents the energy associated with the most intense transition in the Franck-Condon profile, while the AEA refers to the energy difference between the anion and neutral ground vibrational levels [13].

1.3.4 Threshold Behavior and Dipole Bound Anions

The distribution of electrons in a molecule or atom is merely a balancing of electrostatic charge between positive nuclei and negative electrons governed by Coulomb's Law. For neutral species, the dominant term in the interaction potential between the photoelectron and residual species (cation) is the Coulombic potential:

$$V_{Coulomb} \propto \frac{Z_{eff}}{r} \tag{1.3.13}$$

where Z_{eff} is the effective charge of the nucleus. Turning our attention towards photodetachment from anions, the residual species is no longer cationic but is neutral. The Coulombic potential vanishes and the centrifugal potential becomes the dominant attractive potential [20]

$$V_{cent} = \frac{\ell(\ell+1)\hbar^2}{2m_e r^2} \tag{1.3.14}$$

where ℓ is the orbital angular momentum of the outgoing electron, m_e is the rest mass of the electron, and r is the distance from the nucleus. Notice the centrifugal potential is heavily dependent on the orbital angular momentum of the departing electron, and without it the term falls to zero. Recall from Section 1.2.1, the change in orbital angular momentum from a transition induced by an oscillating electric field is $\ell = \ell' \pm 1$, where ℓ' is the original orbital angular momentum and ℓ is the final orbital angular momentum associated with the departing electron's partial wave. Figure 1.7 shows the effective potentials for the first few electron partial wave ℓ values. Near detachment threshold, higher orbital motion generates an energetic barrier for the electron know as the "centrifugal barrier", and it is not until the electron receives an adequate amount of kinetic energy that this barrier is overcome. This feature is shown in Figure 1.7 for ℓ=1-3 as the rise in the potential before falling asymptotically to the detachment energy.

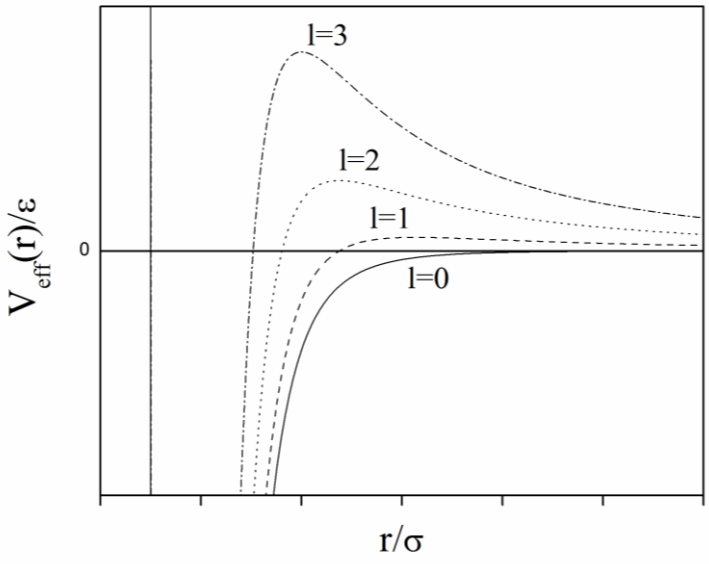

Figure 1.7: Effective potentials for an electron with orbital angular momentum ℓ=0-3 bound to a neutral particle. For ℓ=1-3 a centrifugal barrier arises above the detachment energy ($V_{eff} = 0$).

Wigner derived threshold laws for spherically symmetric potentials associated with cross sectional behavior for a number of two particle interactions [21]. The cross section between a neutral species and electron is strongly dependent on the longest range potential (i.e. Eq 1.3.14), and it was shown for the centrifugal potential that the cross section near threshold follows [21]

$$\sigma_\ell \propto \mathrm{k}^{2\ell+1} \tag{1.3.15}$$

Deviations from this threshold law were observed and reported by Lineberger [22,23] and Brauman [24], and it was determined that dipole effects could have dominating effects on threshold behavior.

1.3.4.1 Dipole Bound States

Early theoretical work by Fermi and Teller [25] and Wightman [26] suggested that an electron could be bound by a dipole moment greater than 1.625 D through solving the Schrodinger equation using the dipole-charge potential

$$\mathrm{V}_{\mathrm{dipole}} = -\frac{\mu e \cos\theta}{\mathrm{r}^2} \tag{1.3.16}$$

where μ is the dipole moment and θ is the angle between the dipole moment and the electron's position vector. It was quickly realized that this point dipole approach had its faults and the critical dipole moment was later refined to μ > 2.0-2.5 D [15,16]. For negative ion photoelectron spectroscopy (assuming a dipole bound state (DBS) exists) absorption of a photon with sufficient energy can excite an electron to a DBS. DBSs typically lie energetically just below the neutral electronic state. It is common to view DBSs as very diffuse orbitals located on the positive end of the dipole moment

surrounding the neutral molecular geometry. The effect of the extra electron in these diffuse orbitals on the neutral geometry is very small and causes little to no perturbation.

Experimentally, many dipole bound molecular anions have been studied through various methods [27-30]. For our purposes, theoretical work suggests that many copper molecular anion species are capable of binding an electron with their dipole moments [31,32], an effect that has an important influence on the results presented in later chapters.

1.4 Time-Resolved Photoelectron Spectroscopy

Detachment from anion electronic states is not always a one photon process, as sometimes the initial photon can act to prepare the anionic species in an excited state that is later probed by a secondary photon. The initially prepared state may evolve in time and probing as a function of time can provide details of the evolution dynamics. These processes are often short but both initially excited and terminal states can be probed within the width of a single laser pulse from nanosecond lasers; however, this method lacks the ability to quantitatively monitor the evolution of the wavepacket as a function of time.

Time-Resolved Photoelectron Spectroscopy (TRPES) employs the use of ultrafast laser systems as a tool for monitoring molecular reaction dynamics in real time with femtosecond resolution [33]. In particular, this can be a very powerful method for observing dissociation dynamics and monitoring the temporal evolution of a wavepacket along a molecule's dissociation coordinate, considering that dissociation can occur on a

time scale of hundreds to thousands of femtoseconds. This has already been utilized for a number of dissociation processes [34-37], and the general scheme is shown in Figure 1.8.

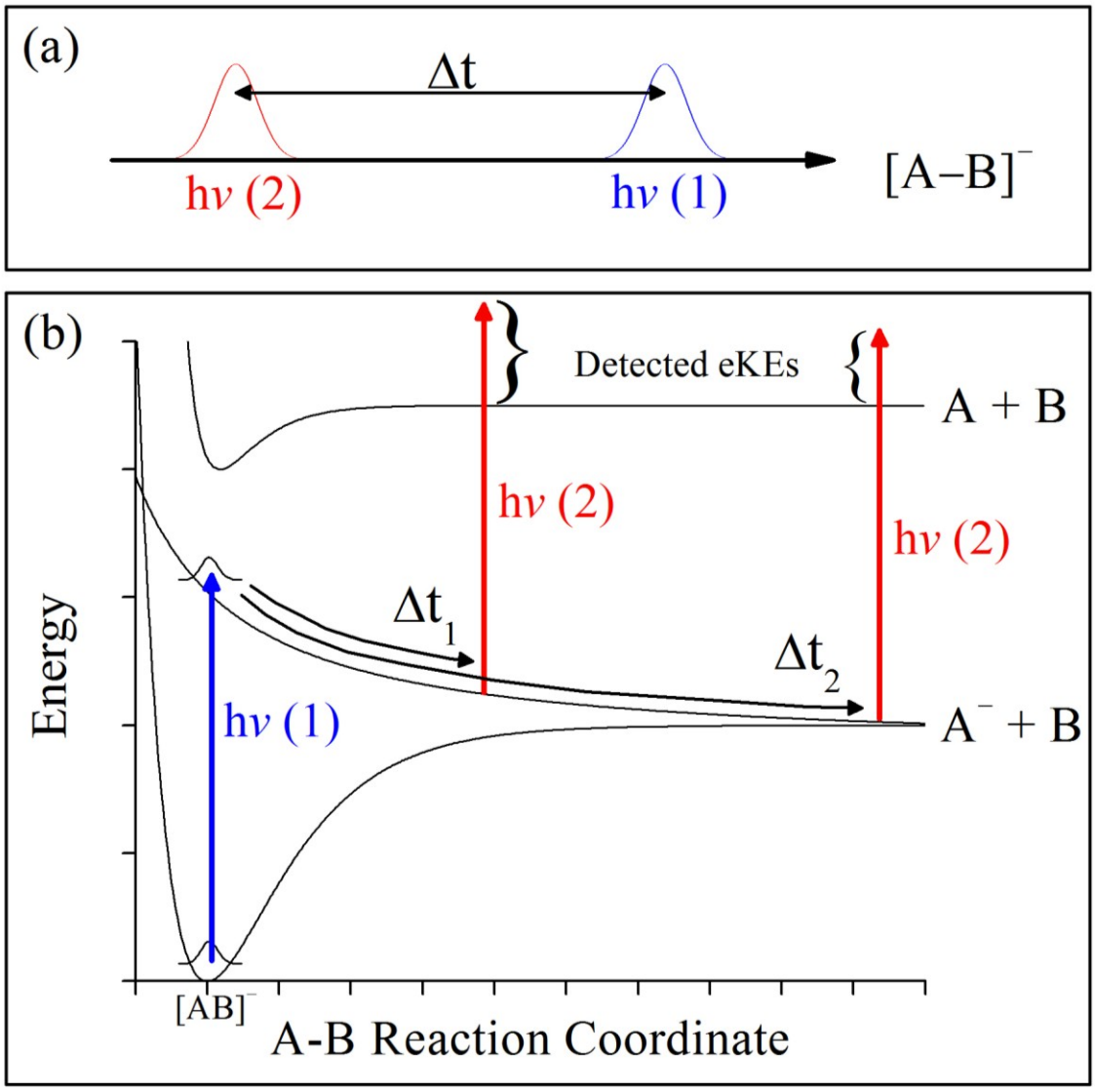

Figure 1.8: (a) General timing scheme for a time-resolved pump-probe experiment. Diatomic anion AB is first excited by the pump laser pulse [hν(1)] and then probed at a certain time delay by the probe laser pulse [hν(2)]. (b) Scheme for a pump-probe experiment for the dissociation of molecular anion AB. $[AB]^-$ is excited by the pump pulse to a dissociative curve where the wavepacket evolves along the AB reaction coordinate and the probe pulse detects the wavepacket at a specific time, Δt_1 or Δt_2. If the wavepacket is allowed to evolve long enough the fragment (A^-) will be detected by the probe pulse.

The general configuration is two laser pulses separated by some temporal delay specified by the user, popularly referred to as a pump-probe process. One pulse (pump) initiates dissociation and the second pulse, trailing the first by a known time delay, probes the wavepacket at that specified delay. Repetition over a series of time delays allows us to follow the dissociation process in real time.

For a typical anion dissociation pump-probe experiment, a nonstationary wavepacket is prepared on a dissociative curve associated with the reaction coordinate. This wavepacket evolves along this dissociation curve until the probe pulse detaches the electron at a timed delay. An example of this type of experiment will be shown in Chapter 4.

Chapter 2

Experimental Methods

The following chapter will contain the general information needed to generate, mass select, and probe anions for photoelectron spectroscopy. A general schematic of the instrumentation used in our experiments can be found in Figure 2.1. The three main areas of focus are anion production, mass selection, and probe/detection of photoelectrons. The regions of the source chamber and detection region are differentially pumped, the former held at 10^{-6}-10^{-5} Torr and the latter at 10^{-8}-10^{-9} Torr. Anions are produced via pulsed supersonic expansion with a carrier gas, coupled with a pulsed arc discharge source [Fig 2.1(1)], which will be explained in more detail in Section 2.1. They are then extracted by a repeller plate [Fig 2.1(2)] into the time-of-flight (TOF) region where the dense packet of anions are accelerated and separated by mass before reaching the detection region. In the detection region we cross the selected mass with a pulsed laser beam to detach photoelectrons which are detected in a velocity-map imaging arrangement [1,38]. Here a general overview of the instrumentation and techniques are presented. Specific details will be provided in later chapters.

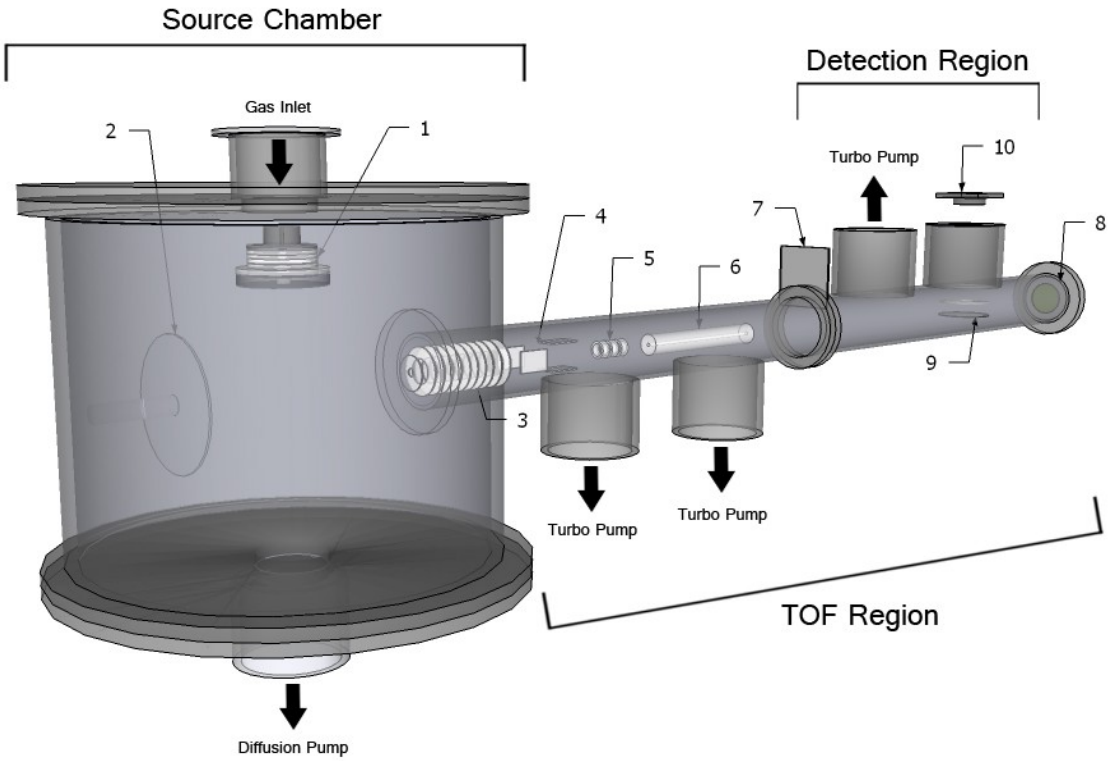

Figure 2.1: Schematic of the photoelectron imaging spectrophotometer, regions labeled appropriately (see text for specific details). (1) Discharge apparatus (2) Repeller plate (3) Acceleration stack (4) Pair of ion deflectors (5) Three ring electrode Einzel lens (6) Potential switch tube (7) Gate valve (8) Mass MCP detector (9) VMI electrodes (10) Imaging MCP coupled to phosphor screen with CCD camera.

2.1 Anion Generation: Metals into the Gas Phase

The heart of negative ion photoelectron spectroscopy lies in the ability to selectively produce anions for probing. Since the common factor between all the experiments listed in this dissertation is binding a copper atom to one or more different atoms, we will focus on this specific issue. An ideal source of anions for our experiments would produce the anions in their ground state to reduce the amount of excited vibrational levels. The method that we employ involves a pulsed supersonic expansion source [40] coupled with

a pulsed discharge source [Fig 2.1(1)], incorporating elements from Osborn et. al. [39] and Ganteför [41,42].

A selected gas is introduced into the source chamber through a pulsed nozzle (General valve Series 9, Parker-Hanifin, 0.76 mm diameter), where the supersonic expansion occurs from high pressure gas entering the source chamber of low pressure (10^{-6}-10^{-5} Torr). The discharge source is composed of a metal wire (cathode) and a stainless steel sewing needle (anode/ground), with the tips separated by ~1 mm. These are held between two insulating plates (Teflon) as shown in Figure 2.2(a,b). A pulsed negative DC high voltage power supply is connected to the cathode through a 7kΩ resistor and its timing is synchronized with the gas pulse. Dielectric breakdown occurs, effectively generating ions from the gas, bombarded by the rapid flow of electrons, and stripping metal atoms from the cathode. This plasma contains metal and gaseous ions, which are allowed to interact with one another in a short cooling tube. Anions are then extracted into the TOF region by a negatively pulsed repelling plate [Fig 2.1(2)].

Production of copper containing anions was achieved by use of a copper wire (0.6mm diameter) cathode. For all experiments medical grade (99.0% purity) oxygen gas was pulsed into the discharge source at backing pressures ranging from 50-80 psi. Specific details for individual anion formation are presented in each subsequent chapter.

2.2 Mass Selection

The packet of anions contains a wide variety of species, and Time-of-Flight Mass Spectrometry (TOF-MS) is employed to separate the individual masses. Once the packet of anions is repelled into the TOF tube they are immediately accelerated by a potential

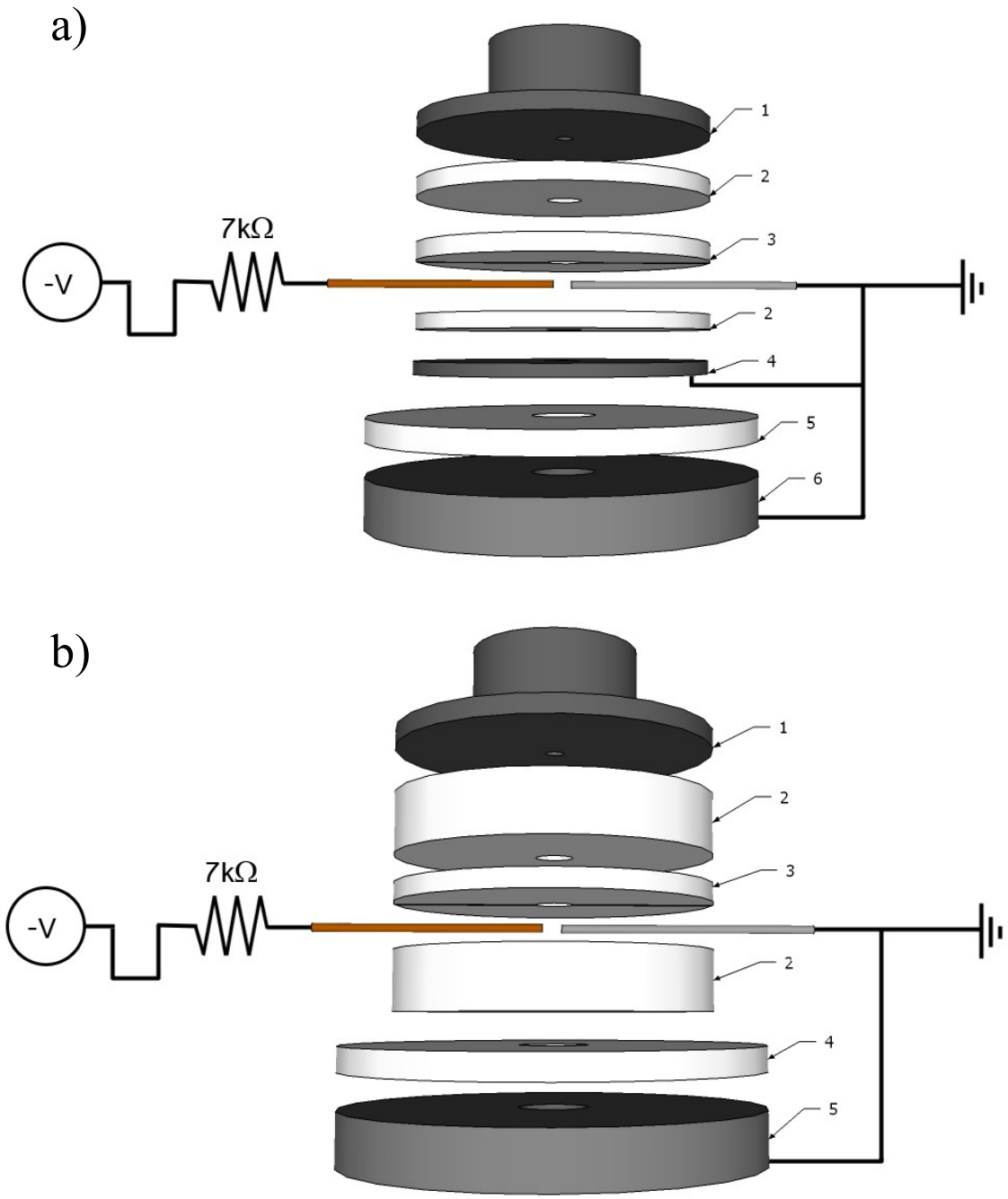

Figure 2.2: Model representations of both discharge setups, **a)** early discharge apparatus (1) pulse nozzle (2) 2 mm thickness Teflon plate (3) 2 mm thickness Teflon plate with slit for electrodes (4) 2 mm thickness stainless steel plate (5) 2 mm thickness, 3 mm diameter hole Teflon plate (6) 5 mm thickness, 3 mm diameter hole stainless steel plate **b)** modified discharge apparatus (1) pulse nozzle (2) 6 mm thickness Teflon plate (3) 2 mm thickness Teflon plate with slit for electrodes (4) 2 mm thickness, 3 mm diameter hole Teflon plate (5) 5 mm thickness, 3 mm diameter hole stainless steel plate. The negative pulsed voltage travels through a 7 kΩ resistor and to the cathode (copper needle) where discharge occurs to the anode (stainless steel needle) held at ground. Needle separation is 1 mm.

gradient (1975 V), using a series of 10 stainless steel plates [Fig 2.1(3)] resistively coupled to ground. After acceleration, the ions pass through two pairs of deflectors [Fig 2.1(4)], an Einzel Lens [Fig 2.1(5)], and a potential switch [44] [Fig 2.1(6)]. An adjustable potential is applied to both deflectors and the central Einzel Lens electrode in order to guide and focus the ion beam into the detection region. The potential switch enables us to re-reference a part of our ion beam to ground without perturbing the path or the kinetic energies of the ions inside the switch at the time of potential step. All other ions not re-referenced will be deflected out of the beam path. At the end of the TOF tube, the ion beam strikes a micro channel plate (MCP) [Fig 2.1(8)] and the mass spectrum is obtained on an oscilloscope. An example mass spectrum is provided in Figure 2.3.

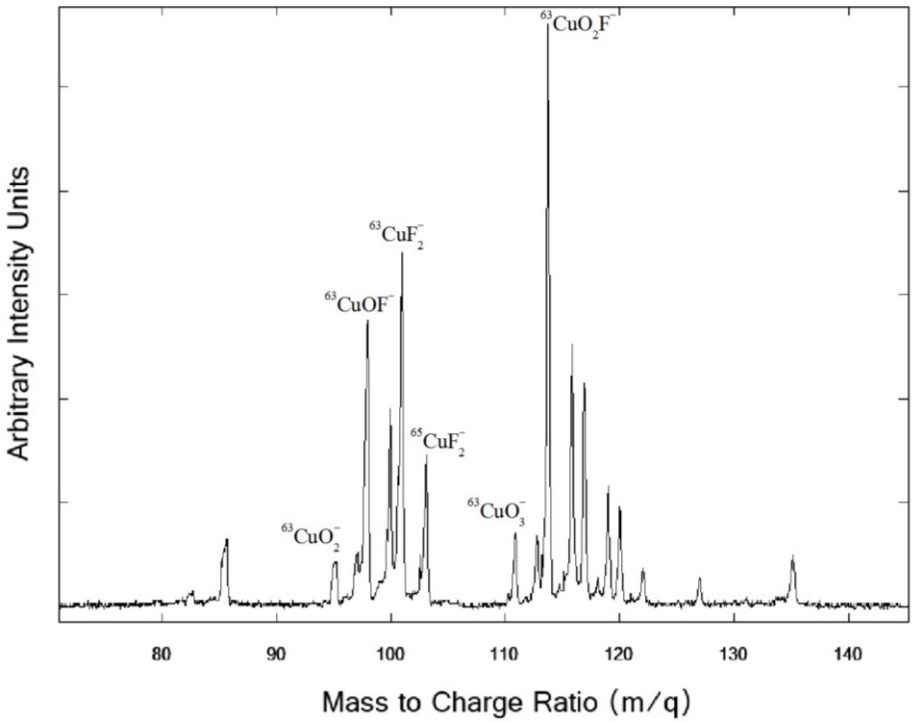

Figure 2.3: Example of a mass spectrum taken from our TOF instrument using copper wire as the cathode and oxygen as the carrier gas. The spectrum contains a variety of copper based anions containing both stable isotopes of copper (^{63}Cu & ^{65}Cu, respective natural abundance 0.69:0.31 ratio), some of which are labeled above their respective peaks. Calibration of mass spectra can be accomplished with two predetermined masses.

Strictly speaking, TOF separates ions by their mass-to-charge ratio (m/q). Since our source generates a packet of singly charged anions (q = −1), it is common to refer to the peaks in the mass spectrum by their respective mass, as q is constant between all ions. The potential energy (PE) of an individual particle can be expressed by the following equation:

$$PE = qV \tag{2.1}$$

where q is the charge of the particle and V is the voltage of the electric field. When the ion is accelerated in the electric field the potential energy is converted to kinetic energy:

$$qV = PE = KE = \frac{1}{2}mv^2 \tag{2.2}$$

where KE is the kinetic energy, m is the mass of the ion, and v is the velocity. Since all ions have the same KE, different masses will have different velocities, and upon entering the field free region of the TOF tube their respective velocities will remain constant. Velocity can be expressed as units of distance (x) over time (t) and Equation 2.2 can be rearranged to give the time of the particle as a function of its mass-to-charge ratio for a TOF tube of length x:

$$t = \frac{x}{\sqrt{2V}} \times \sqrt{\frac{m}{q}} \tag{2.3}$$

As an example, our instrument utilized a two meter long flight tube that can sufficiently separate out anions of single charge to within Δm/m values of 0.39% resolution. Two copper anion isotopes are generated in our instrument, $^{63}Cu^-$ and $^{65}Cu^-$, and when accelerated with a 1975 V electric field yield a flight time of 25.714 μs and 26.119 μs respectively (Δt = 400 ns). Typical FWHM for mass peaks are 100 ns, which provide sufficient temporal separation for a 5-8 ns laser pulse. This laser pulse is

synchronized with the selected mass by monitoring the laser pulse on the same oscilloscope as the mass spectrum.

2.3 Detection of Photoelectrons

As mentioned in Chapter 1, if the incoming polarized laser pulse has a sufficient amount of energy to detach an electron, then a photoelectron will be emitted at a certain angle and velocity with respect to the polarization of the laser beam. Detection of the angular distribution of our photoelectrons (PAD) could be accomplished by having a spherical detector that could detect each individual photoelectron's angle and velocity, but this would be rather impractical and expensive. Chandler and Houston invented a method for detection of photofragments in the photodissociation dynamics of methyl iodide in 1987 [43]. It enabled the user to detect a two-dimensional (2D) image of fragments guided by a repeller plate towards a pair of grounded grids and MCP detector, effectively projecting the three-dimensional distribution of fragments into the 2D field for image analysis. In 1997, Eppink and Parker expanded upon this design by taking out the grids and adding a third electrode [1,38] officially giving rise to velocity-map imaging (VMI).

Our VMI setup is very similar to that of Eppink and Parker and consists of three electrodes [Fig 2.1(9)], Repeller (R), Extractor (E), and Ground (G). This is combined with a chevron type 40 mm diameter MCP position sensitive detector (Photonis USA, Inc., APD 3040 FM, 10 μm diameter pores) coupled to a P20 phosphor screen and CCD camera array (Imperx, Inc., IPX- VGA120-L, 640×480 pixels). A schematic for the VMI

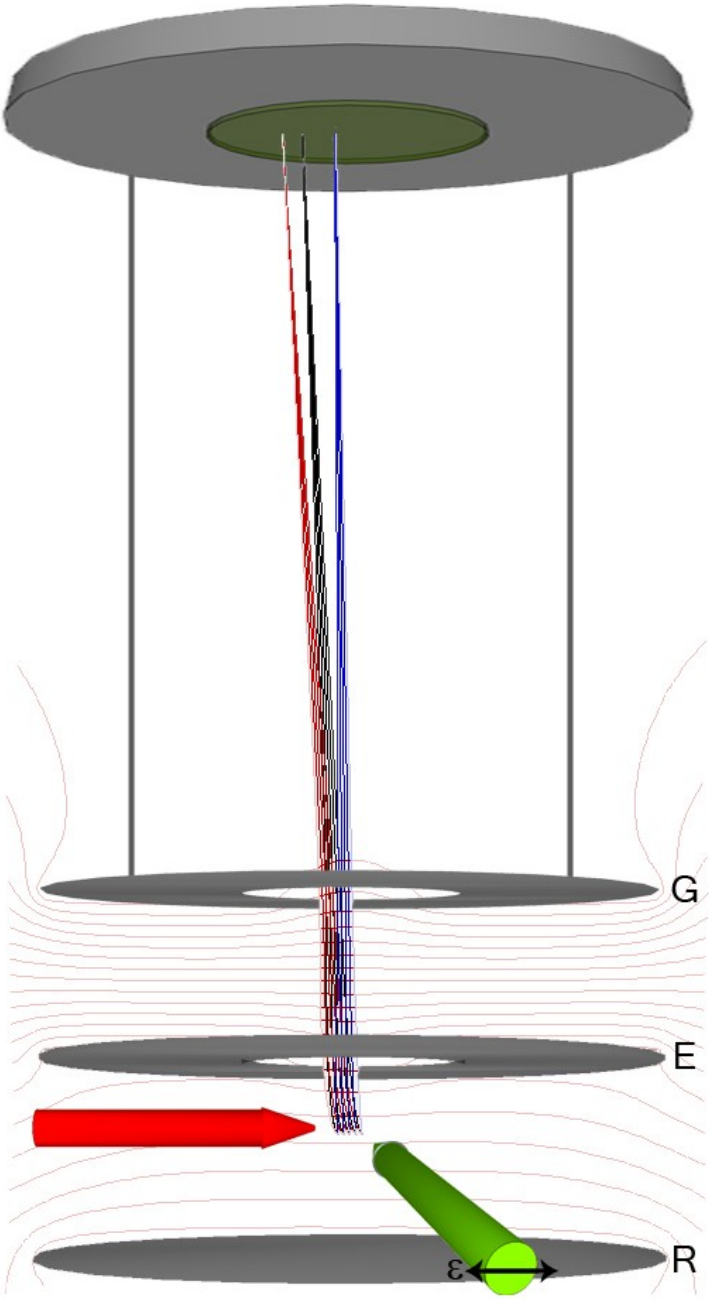

Figure 2.4: Velocity Map Imaging representation with three electrodes, Repeller (R, −1000 V), Extractor (E, −700 V), Ground (G, 0 V), and detector MCP (top). Thin red lines represent the electric field lines present while device is active. The anions path and laser beam are represented by the large red and green arrows respectively. ε is the laser polarization in the laboratory frame z-axis. Ejected electron flights are represented by the vertical red (eKE = 2 eV), black (eKE = 1 eV), and blue (eKE = 0.5 eV) lines. The simulation displays the electrons at different velocities (red, black, blue) ejected along the lab frame z-axis at different positions (5 mm spread, 1 mm separation). Higher velocity electrons hit at a larger radius on the detector MCP. Simulation performed with SIMION [46].

arrangement can be seen in Figure 2.4. When the electrodes have no voltage applied, the ions pass between the R and E electrodes, and prior to detection a negative voltage is applied to both lower electrodes and the top electrode is held at ground, generating an electric field [Figure 2.4 (thin red lines)] that focuses detached electrons with the same velocity vector to the same position on the detector. A typical voltage ratio for E:R is 0.70. The flight paths for three different eKE values are presented in Figure 2.4, where electrons with higher eKE values are focused at a larger radial distance from the center of the detector.

The MCP multiplies the electron impacts by orders of magnitude to allow detection using the phosphor screen and CCD camera. This process is repeated hundreds to thousands of times at a camera operation speed of 10-50 fps. Electron impacts recorded on the detector are summed in a frame by frame manner using a PC. For nanosecond laser detachment, one final image would be the subtraction of two separately summed images to eliminate the background noise. Typical collection times for each image are 10 seconds of the laser on ion signal (ion + background) and 10 seconds off ion signal (background) for 10 minutes. It is common for data sets to consist anywhere from 2-25 of these final images depending on variables such as laser power, ion cross-section, ion signal strength, signal-to-noise ratio, etc. For a femtosecond pump-probe experiment, each final image consists of electrons solely produced by the sequential action of both pump and probe beams. This is accumulated through a four image (A to D) collection scheme. Image A is recorded with both pump and probe beams propagating through the detection region. Images B and C have only the probe or pump beam respectively present. D represents a pure background, recorded when neither laser propagates through

the detection region. The result image is obtained by subtraction, A – B – C + D. Typical data collection time for either scheme is 10 min for one image and several images are collected and summed for each wavelength and time delay to produce the final image.

2.4 Laser Systems

2.4.1 Nanosecond System

Most of the experiments reported here were performed with a Spectra-Physics Sirah Pulsed Dye Laser (Cobra-Stretch LG-24), which is pumped with a Spectra-Physics Quanta-Ray INDI Pulsed Nd:YAG (neodymium-doped yttrium aluminum garnet; $Nd:Y_3Al_5O_{12}$) laser. The Q-switched YAG laser emits horizontally polarized 1064 nm light (450 mJ, 10 Hz) as the first harmonic, and can be frequency doubled or tripled to produce 532 nm light (200 mJ, 10 Hz) or 355 nm light (100 mJ, 10 Hz) respectively. It is the latter two harmonics that are used to pump the Sirah Dye Laser to produce a wide variety of fundamental wavelengths from 370-780 nm, which can also be frequency doubled with a β-barium borate (BBO) crystal, achieving wavelengths from 250-380 nm. Typical temporal widths of the pulses are 5-8 nanoseconds.

2.4.2 Femtosecond System

The real time reaction dynamics of chemical systems usually occur on short time scales, where monitoring a system with the temporal width of a nanosecond laser pulse can sometimes produce the image of a two photon process [Section 1.4]. This can be problematic for monitoring the reaction initiated by the first photon, as the time scale is

unknown between the second probe photon in the nanosecond laser pulse. Instead we can employ femtosecond (10^{-15} s) laser technology that can produce pulses around 120 fs, which work within the timescale of molecular vibrations and dissociations. This enables the user to monitor these reactions with two temporally short pulses of light separated by a known time delay.

Our femtosecond laser system is built upon multiple laser systems for production and combination of seed pulses and amplification pulses. A Spectra-Physics Tsunami Mode-locked Ti:sapphire Laser is optically pumped by a Spectra-Physics Millenia Pro-5sJ Diode-Pumped, CW Visible Laser System. The second harmonic output from the Millenia (4.90-5.00 W, 532 nm) pumps the Ti:sapphire rod in the resonator cavity of the Tsunami. Output powers and wavelength bandwidths from the Tsunami are monitored with a Spectra-Physics power meter (Model 407A) and Ocean-Optics SpectraSuite Spectrophotometer respectively, and tuned accordingly using a prism dispersion control, slit wavelength selector, and both high reflectors that compose the resonator cavity. The Tsunami can be tuned within the wavelength range 705-865 nm, however peak power is obtained at 800 nm, providing a bandwidth of about 12-14 nm centered at this wavelength. The laser cavity is actively mode-locked by a Spectra-Physics Lok-to-Clock Model 3955 Module, which effectively modulates the radiation in the resonator cavity at a rate that matches the round-trip time of light in the cavity [45]. Pulses released from the cavity are then sent to our Spectra-Physics Spitfire Pro HP (Ti:Sapphire Regenerative Amplifer System) for amplification.

The Spitfire employs the chirped pulse amplification method in order to amplify low energy Ti:sapphire laser pulses provided from the Tsunami. The three stage procedure

for amplification is as follows: stretching, amplification, and compression. Stretching is accomplished with a diffraction grating that separates, or stretches, the low power short pulse into its respective redder and bluer shifted beam components. A Spectra-Physics Empower (Intracavity-Doubled, Diode-Pumped Nd:YLF [neodymium-doped yttrium lithium fluoride; $Nd:LiYF_4$]) Laser System provides the power for amplification of input seed pulses, and typical power amplifications are on the order of 10^6, for example an input seed pulse of a few nanojoules can be amplified to a millijoule. The final compression stage acts the same as a reversed stretcher, effectively compressing the pulse to yield an output of 2.1-2.4 W for a center wavelength of 800 nm. Time syncing for all Spitfire and Tsunami components is accomplished with a Spectra-Physics Timing Delay Generator (TDG). The output pulse width is monitored and fine tuned with the aid of a Newport PulseScout Autocorrlator.

Chapter 3

CuO^-: Relative Branching Ratios and Higher Anionic Excited States

3.1 Introduction

The unusual characteristics of transition metal oxides, which range from magnetic to insulating properties, have made them an attractive target for study [47-54]. Specifically, numerous experimental and theoretical works have been done on copper oxides [55-58] with considerable attention directed at the diatomic species CuO [31,59-62,74]. Early emission spectroscopy work on the neutral species characterized low lying excited electronic states of CuO including vibrational and rotational analysis [63,64].

The first negative ion photoelectron spectroscopy study on CuO^- was performed by Polak et. al. [60], where they characterized the first two electronic states of the neutral, $X^2\Pi$ and $Y^2\Sigma^+$, and assigned the ground anion electronic state as $X^1\Sigma^+$. For the remainder of this chapter we will adopt their terminology for these electronic states. The ground state of the neutral $X^2\Pi$ was observed to have a small spin-orbit splitting (34.6 meV), $^2\Pi_{3/2}$ and $^2\Pi_{1/2}$ [see Section 1.3.1]. In this chapter, the threshold behavior of the vibrational levels associated with these states will be explored.

In order to understand bonding in the anion, Polak et. al. [60] concluded, based on a prior analysis of the neutral [65], that the anion can be described by a simple molecular orbital model. An energy diagram corresponding to this interpretation of the anion is provided in Figure 3.1(a), showing only the valence orbital levels. Since the ground state of the neutral can be described by the ionic configuration $Cu^{+}O^{-}$, with the electron hole located on the copper atom, the anion can similarly be described with addition of an extra electron. The first few valence configurations of the anion, along with their term symbols, are shown in Equation 3.1:

$$\begin{aligned} {}^{1}\Sigma^{+} &: 3d\sigma^{2}\,3d\pi^{4}\,3d\delta^{4}\,2p\sigma^{2}\,2p\pi^{4}\,4s\sigma^{0} \\ {}^{1,3}\Pi &: 3d\sigma^{2}\,3d\pi^{4}\,3d\delta^{4}\,2p\sigma^{2}\,2p\pi^{3}\,4s\sigma^{1} \end{aligned} \tag{3.1}$$

$^{1}\Sigma^{+}$ is the lowest energetic electronic state, in which the extra electron is mainly located in the oxygen 2pσ orbital, although there is partial sharing with the copper 4s orbital. The singlet and triplet Π states represent excited states of the anion and are described as having the electron largely based in the copper 4s orbital. These configurations were later verified with theoretical work by Xian et. al. [61].

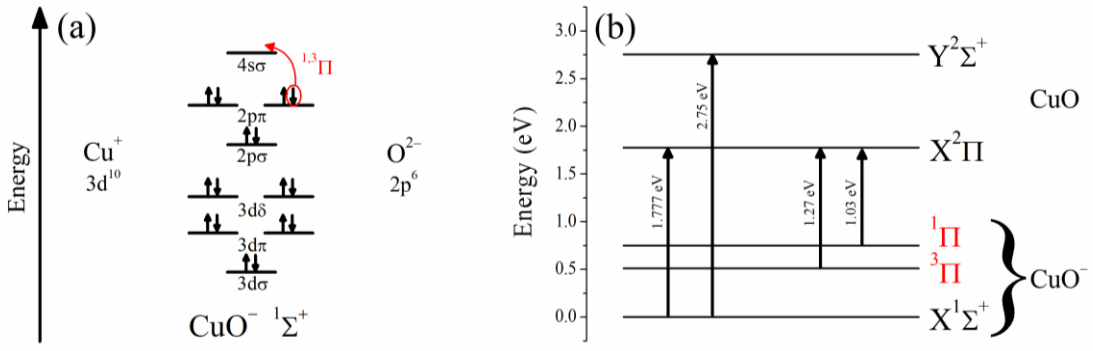

Figure 3.1: a) Orbital energy level diagram for the ground anion state ($^{1}\Sigma^{+}$) showing the filled valence electrons. Promotion of an electron from the oxygen 2pπ orbital to the copper 4sσ orbital (red) generates new electronic states, $^{1,3}\Pi$. **b)** Quantitative energy level diagram for the first few anion electronic states and the first two neutral electronic states. Energy gaps are labeled with vertical arrows, representing the eBE for those particular transitions.

Another photoelectron study based on a variety of copper oxides was performed by Wu et. al. [49], where they studied the detachment of CuO^- at various wavelengths. Their photoelectron spectra showed the presence of transitions originating in an excited state of the anion, which were not seen in the previous photoelectron study [60]. In addition, they observed a second anion excited state transition when a fragment CuO^- was probed in a two photon process from the dissociation of CuO_3^-. They attributed both to originate from excited $^3\Pi$ spin-orbit states of the anion, although these were later reassigned in a later theoretical study [61] to the $^{1,3}\Pi$ states [Eq. 3.1]. An energy level diagram of CuO and CuO^- electronic states are shown in Figure 3.1(b). The nature of these CuO^- excited states from our experimental work will be explored in detail in the results and discussion.

3.2 Experimental

Photoelectron images were collected from wavelengths 310-710 nm (4.00-1.75 eV), with the exception of the range 380-430 nm which could not be achieved due to dye laser grating limits. CuO^- molecular anions were generated by flowing 50 psi of O_2 gas (99.0% purity) through a pulsed nozzle (10 Hz repetition rate) into the discharge apparatus [Section 2.1]. During operation the ion source chamber was maintained at pressures between 6×10^{-6}-8×10^{-6} Torr. The $^{63}Cu^{16}O$ isotopic mass peak was selected for study due to its highest yield in the mass spectrum.

The momentum space distribution of photoelectrons is reconstructed from the collected image using the BASEX program of Dribinski et. al. [3] allowing extraction of the photoelectron spectrum and corresponding angular distributions.

3.3 Results and Analysis

3.3.1 Branching Ratios of Higher Vibrational Levels at the $^2\Pi$ Threshold

Displayed in Figure 3.2(a) is a 370 nm (hν = 3.351 eV) photoelectron image (left half) and its corresponding transformed image (right half) recorded on our instrument.

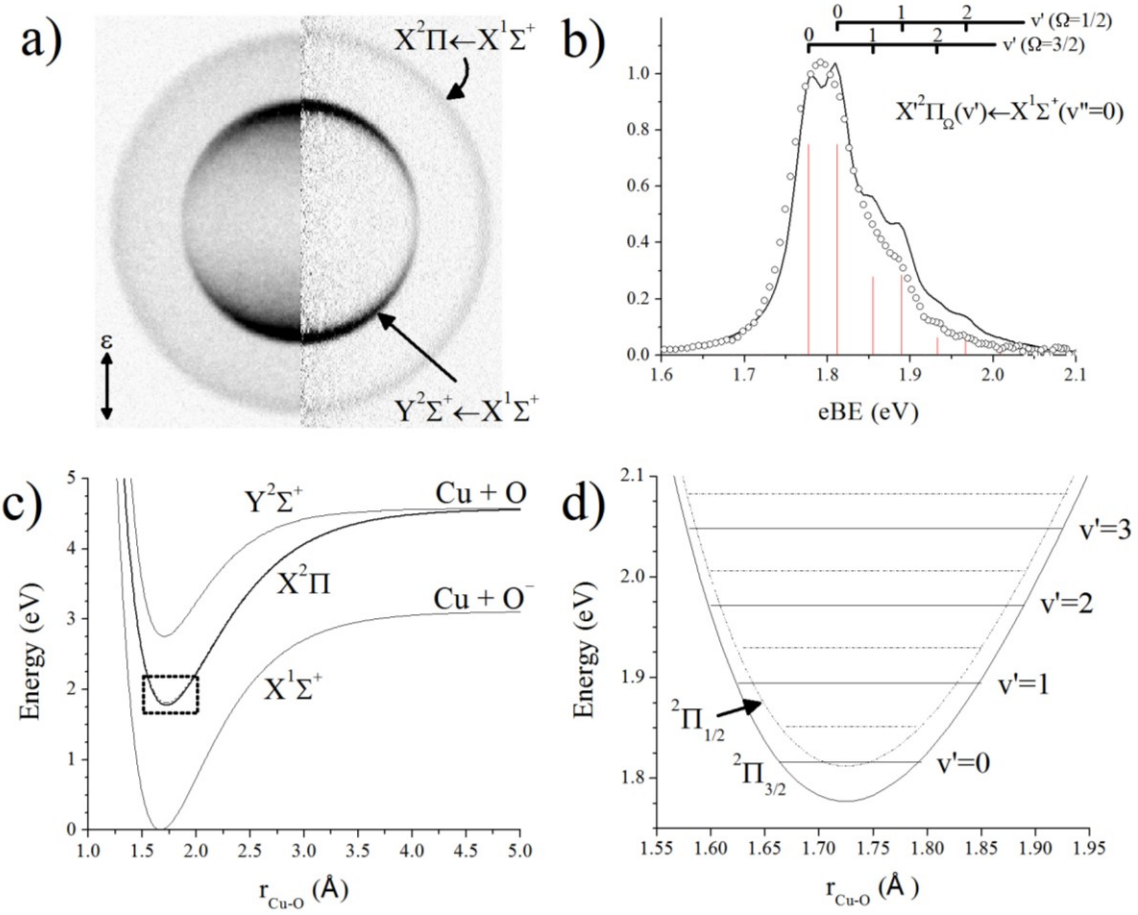

Figure 3.2: a) CuO^- photoelectron image (left half) and reconstructed image (right half) at 370 nm. **b)** Photoelectron energy spectrum at 560 nm (open circles) showing the unresolved vibrational structure along with a Franck-Condon analysis stick spectrum (red) and convoluted spectrum (solid black line). **c)** Morse potentials for the ground state anion and the first two neutral electronic states. **d)** Zoomed in version of the dotted box in *c*, shows the $^2\Pi$ is actually split into two spin orbit states, $^2\Pi_{3/2}$ (solid line) and $^2\Pi_{1/2}$ (dotted line), by 34.6 meV. The first four vibrational levels for the $^2\Pi_{3/2}$ state are displayed; the first four $^2\Pi_{1/2}$ vibrational level labels were omitted for clarity.

It shows that two electronic states of neutral CuO are accessible within the energy range available in the experiment. These are the $X^2\Pi \leftarrow X^1\Sigma^+$ and $Y^2\Sigma^+ \leftarrow X^1\Sigma^+$ transitions. Reducing the photon energy to 560 nm ($h\nu$ = 2.214 eV) yields slightly better resolution for the $X^2\Pi$ state from which a Franck-Condon (FC) analysis [Section 1.3.3] could be performed [Figure 3.2(b)]. The FC factors were convoluted with a 50 meV FWHM Lorentzian function to account for instrumental broadening. The program PESCAL [66] was used for the FC analysis with the Morse potential parameters from Ref[60,67]. The Morse potential curves for neutral/anion electronic states are plotted in Figure 3.2(c), and they represent the ground state of the anion ($X^1\Sigma^+$), the ground state of the neutral ($X^2\Pi$), and the first excited state of the neutral ($Y^1\Sigma^+$), with the $X^2\Pi$ state degeneracy lifted by a spin-orbit splitting [Figure 3.2(d)]. The two spin-orbit states, $^2\Pi_{3/2}$ and $^2\Pi_{1/2}$, are separated by 34.6 meV with the former being lower in energy. The first four vibrational levels for both spin-orbit states are also shown in Figure 3.2(d) and will be central to the later discussion.

A 2D contour plot was constructed from photoelectron spectra recorded in the wavelength range 560-695 nm in 5 nm increments [Figure 3.3]. These photon energies span the energy range of Figure 3.2(d). A horizontal slice through the contour plot would represent the photoelectron spectrum at a specific photon energy, and three such photoelectron spectra are displayed in Figure 3.3(a-c). A vertical slice through the plot indicates a specific vibrational channel's binding energy [Figure 3.3 (gray lines)], so any change in the photoelectron spectral intensities along the vertical slices correlates with a change in the intensity of the specified vibrational channel relative to the $0\leftarrow0$ transition as a function of the photon energy. All photoelectron spectra were scaled relative to the

$^2\Pi_{3/2}$ (v′=0) ← $^1\Sigma^+$ (v″=0) transition at an electron binding energy (eBE) of 1.78 eV, which we will refer to as the 0←0 transition. With this knowledge, it becomes clear in the contour plot that a noticeable change in intensity occurs for individual higher vibrational channels relative to the 0←0 transition at the photon energies displayed in Figure 3.3(a-c).

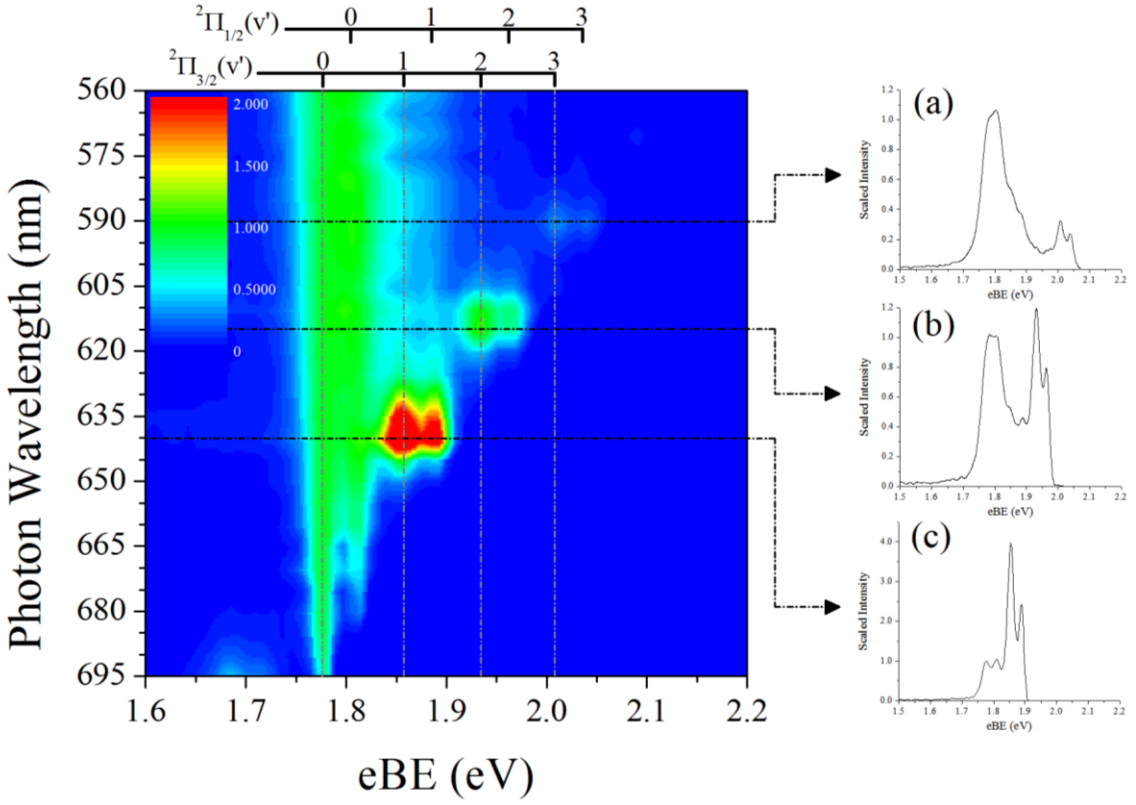

Figure 3.3: 2D contour plot of photon energy vs. electron binding energy from the ranges of 560-695 nm. Each horizontal dot-dash slice (black) through the plot represents one photoelectron energy spectrum **a)** 590 nm **b)** 615 nm **c)** 640 nm. Each vertical dot-dash slice (gray) represents a vibrational state binding energy for the $^2\Pi_{3/2}$ state. Labels for $^2\Pi_{1/2}$ vibrational states were omitted for clarity.

Traversing the plot vertically (increasing photon energy), the $^2\Pi_{3/2}$ v′=1-3 channel openings can be observed. The sharp initial increase in intensity for each individual vibrational channel is followed by a decrease in intensity, falling to approximately the FC expectation at higher photon energies. The same effect is observed in the $^2\Pi_{1/2}$ v′=1-3

channels as well, although the vertical lines were omitted for clarity. An interesting observation is the $^2\Pi_{3/2}$ and $^2\Pi_{1/2}$ v′=1-3 channels appear to simultaneously rise and fall in intensity at the same photon energy; however, we note this may be due to instrumental broadening, which prohibits complete resolution of the spin orbit splitting (34.6 meV).

The area under the curve for each vibrational channel was monitored from wavelengths 580-658 nm. This was achieved by fitting Lorentzian line shapes to both $^2\Pi_\Omega(v')$ ($\Omega= \frac{3}{2}, \frac{1}{2}$) states from v′=0-3 and taking the areas under the Lorentzians. Due to the instrumental resolution, we summed the areas of both Lorentzians for $^2\Pi_\Omega(v')$ ($\Omega= \frac{3}{2}, \frac{1}{2}$) states, and labeled them together as v′←0. The v′=1-3 areas are plotted relative to the 0←0 channel areas. The results are represented in Figure 3.4, which is a more quantitative way of looking at the same effect as Figure 3.3. Plotting the ratios [Figure 3.4] against photon energy allows us to identify associations between vibrational level energies [Figure 3.4, (vertical lines)] and the maxima observed in Figure 3.3.

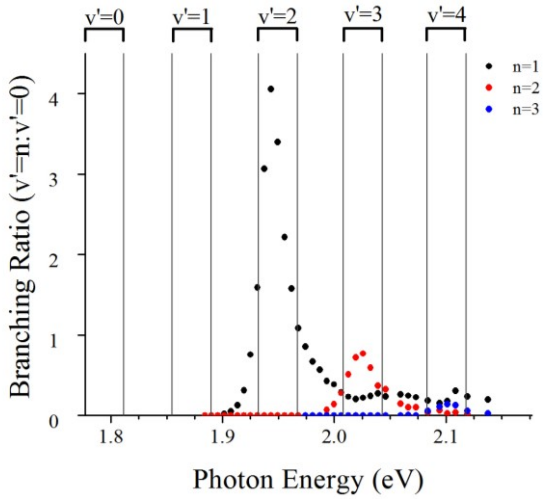

Figure 3.4: Branching ratios for v'=1-3 relative to the v'=0 channel vs. eKE of the v'=0 channel. The solid vertical lines represent the threshold energy for vibrational channels of the $^2\Pi_{3/2}$ electronic state and the vertical lines represent the threshold energy for vibrational channels of the $^2\Pi_{1/2}$ electronic state. Corresponding vibrational quantum numbers labeled at the top of their respective channel.

3.3.2 PADs for the $X^2\Pi \leftarrow X^1\Sigma^+$ and $Y^2\Sigma^+ \leftarrow X^1\Sigma^+$ transitions

Figure 3.5 shows the PADs for the two transitions observed in Figure 3.2(a). The anisotropy parameters (β) for the $X^2\Pi \leftarrow X^1\Sigma^+$ transition (filled circles) were determined by using the energy range of the FHWM associated with the unresolved $^2\Pi$ spin orbit transitions for each photon energy. We report β = +0.25 at a photon energy of hν = 3.49 eV, which is comparable to Ref[60]'s β = +0.35 at a similar photon energy. The PAD for this transition initially shows a negative trend similar to detachment from a π-like orbital, reaching a minimum (β = ~0.5) and rising to an isotropic/slightly positive value. However, near the channel opening for the $Y^2\Sigma^+ \leftarrow X^1\Sigma^+$ transition ($eKE_{X\leftarrow X}$ = 0.97 eV) the PAD deviates back to isotropic before trending to higher β values at high eKE. Theoretical electronic state configuration calculations indicate that the detachment from the 2pπ orbital [Figure 3.1] is the dominant factor for this transition with a slight contribution from detachment from the 2pσ orbital [61].

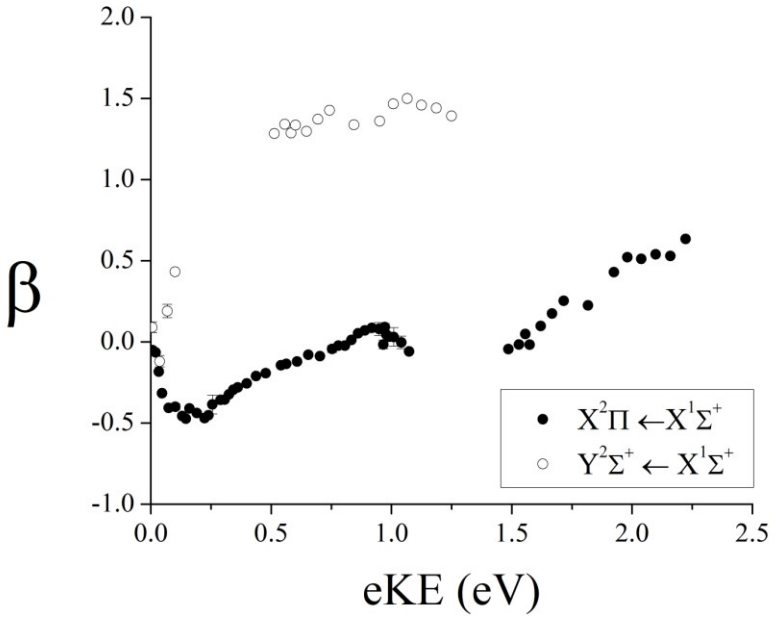

Figure 3.5: PADs for the $X^2\Pi \leftarrow X^1\Sigma^+$ transition (filled circles) and the $Y^2\Sigma^+ \leftarrow X^1\Sigma^+$ transition (open circles). Anisotropy values are monitored as a function of each transition's respective eKE.

The PAD for the $Y^2\Sigma^+ \leftarrow X^1\Sigma^+$ transition (open circles) shows strong positive character leveling off at higher eKE values at $\beta = +1.5$. Our results are again comparable to Ref[60] at a similar photon energy. The positive nature of this PAD suggests detachment from a σ-like orbital, also backed by the same theoretical study, showing that the $Y^2\Sigma^+$ state electronic configuration is mainly composed of a hole in the 2pσ orbital, with small contribution from a 3dσ hole [61], from where the electron was detached.

3.3.3 Photoelectron Spectra for Higher Lying Anionic Electronic States

As the photon energy is decreased near and below the threshold of the 0←0 transition (eBE = 1.78 eV), other transitions become more obvious in the photoelectron spectrum. Figure 3.6 displays two photoelectron spectra of CuO^- (690 nm, 710 nm) with their corresponding photoelectron images above them.

In the 690 nm image ($h\nu$ = 1.80 eV), just above the 0←0 energy threshold, three different transitions ending in the neutral $^2\Pi$ state are apparent. The feature labeled 0←0 is the previously discussed $^2\Pi_{3/2}(v'=0) \leftarrow {}^1\Sigma^+(v''=0)$ transition, while the feature labeled 0←1 corresponds to the $^2\Pi_\Omega$ ($\Omega = \frac{3}{2}, \frac{1}{2}$) $(v'=0) \leftarrow {}^1\Sigma^+(v''=1)$ transitions, $\Omega = \frac{3}{2}$ having the lower binding energy. Transitions with $v''>0$ are commonly referred to as a hot bands, the parent anion occupying a vibrational level other than the ground state. Changes in the source conditions (particularly temperature) alter the intensities of these transitions relative to the 0←0 transition intensity [49,60]. The assignment of the third feature at an eBE = 1.27 eV is the subject of some debate. Originally observed by Wu et. al. [49], this transition was assigned to originate in the $^3\Pi_2$ excited anion state and terminate in the $^2\Pi$ neutral ground state. A subsequent theoretical study [61] suggested reassignment of the

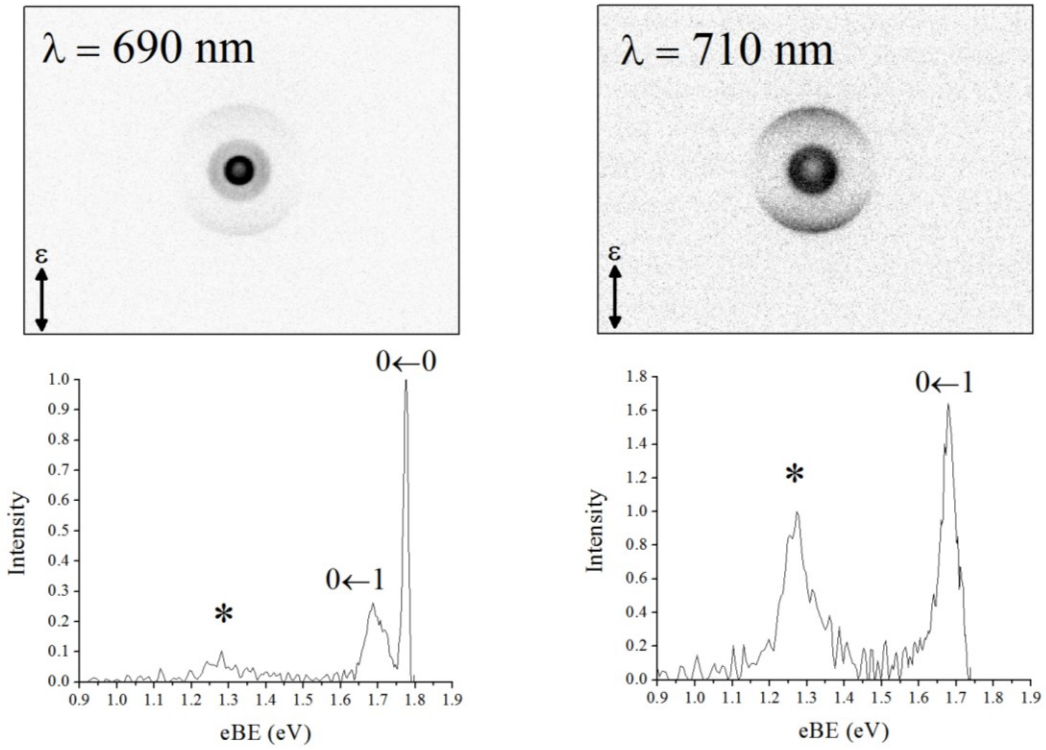

Figure 3.6: CuO^- photoelectron images (top) with their corresponding energy (eBE) spectra (bottom) for detachment at 690 nm (hν = 1.797 eV, left) and 710 nm (hν = 1.746 eV, right). Near the threshold for the $^2\Pi_{3/2}(v'=0) \leftarrow {}^1\Sigma^+(v'=0)$ transition (0←0), more transitions become observable such as hot bands (0←1) and the feature at an eBE = ~1.27 eV. Dropping to lower photon energy with 710 nm, the 0←1 is at its energetic threshold and the 1.27 eV feature becomes more apparent.

transition to span all the spin-orbit components of the $^3\Pi$ state based on the calculated small spin-orbit splitting between the $^3\Pi_2$ and $^3\Pi_0$ states (35.7 meV).

Upon reduction of the photon energy to 710 nm (hν = 1.75 eV), the 0←0 transition is no longer observable as there is insufficient photon energy, but the 0←1 transition remains accessible, albeit very near its own energy threshold. The 1.27 eV transition is clearer compared to the 690 nm image, the result of dynamic range effects, and has a FWHM = ~90 meV at an eKE = 0.48 eV, suggesting that the transition width is not solely due to instrumental broadening [ΔE(FWHM)/E(eKE) = ~10%]. The anisotropy

parameter was measured to be $\beta = +1.6$ at eKE = 0.48 eV, where the positive character of this PAD indicates preferentially parallel detachment relative to the laser polarization.

3.4 Discussion

The results presented thus far can be divided into three topics: (1) Analysis of the PADs for the two electronic transitions $X^2\Pi \leftarrow X^1\Sigma^+$ and $Y^2\Sigma^+ \leftarrow X^1\Sigma^+$. (2) Non-Wigner threshold behavior for vibrational channel cross sections, as it has been shown that individual vibrational channels see enhancement in their cross sections. (3) The nature of the higher excited states of the anion, previously reported in Ref[49], the assignment of which has been the subject of debate. Discussion will assess the nature of the non-Wigner behavior with the aid of *ab initio* calculations, and also explore the characterization of this excited anion state with aid from previously reported data and theoretical work.

3.4.1 Parent Orbitals Reflected in Transition PADs

The two PADs shown in Figure 3.5 represent detachment from the same anion electronic state ($X^1\Sigma^+$) but from different parent orbitals. Note, the PAD for $X^2\Pi \leftarrow X^1\Sigma^+$ [Figure 3.5 (filled circles)] should not be strongly affected by the coalescence of the two spin-orbit transitions as they are both detached from the same parent orbital. Even though β is eKE dependent, the difference in eKE between the two states (0.035 eV) is small and both spin-orbit state PADs should be roughly the same.

For the transition to $X^2\Pi$ the detached electron originates in the O2pπ orbital, and the transition to $Y^2\Sigma^+$ represents detachment from O2pσ orbital. Even though both

transitions originate in an O2p orbital, the differences in the PADs reflect the difference in symmetry between the two parent orbitals (π & σ). The PAD for detachment from the 2pπ orbital is at low eKE (<0.93 eV) reminiscent of the Cooper-Zare equation [5].

3.4.2 Relative Changes in Vibrational FC Factors Linked to Dipole Bound States

The FC analysis in Figure 3.2(b) provides a reasonable description of the observed relative intensities between vibrational channels. Aside from Wigner effects near threshold [Section 1.3.4], the relative intensities between vibrational channels should not change with photon energy, as the FC factors are independent of photon energy; hence, they can serve as a reference to observe deviations in experimental data. Previously reported by our laboratory, deviations in spin-orbit channel branching ratios for I^- clusters have proven to be a useful tool for monitoring dipole bound state (DBS) resonances [73]. The relative FC factors associated with vibrational transitions can likewise serve in a similar way to monitor electronic resonance scattering effects.

The area ratios for the vibrational channels $v' = 1$-3 are plotted as a function of their respective channel's eKE in Figure 3.7 (black circles). The shape of the profiles bear a resemblance to Fano profiles associated with resonance phenomena [68]. A Fano line shape, convoluted with the appropriate Lorentzian response function, was fit to each data set and lifetimes for the resonances were extracted [Figure 3.7, (red line)]. The respective lifetimes for each vibrational channel $v' = 1$-3 are 50.6, 38.3, and 40.4 fs. While these resonance lifetimes may appear short at first glance, they are comparable to the timescale for nuclear vibration, in which one period for the CuO stretching mode takes 52.1 fs. Such a delay in electronic detachment is characteristic of accessing

resonances caused by DBSs. The permanent electric dipole moment of neutral CuO has been experimentally reported to be 4.57±0.03 D [74], which is well above the dipole moment value to support a DBS capable of causing such resonances. Using a combination of *ab initio* calculations along with our experimental results, we intend to explore the nature of this possible dipole bound resonance.

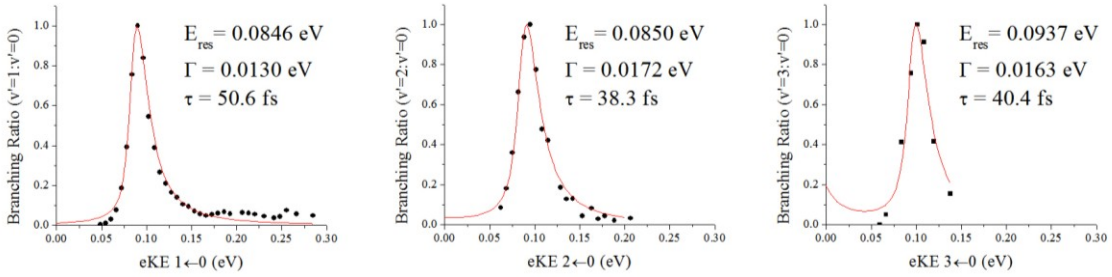

Figure 3.7: Relative branching ratios for the v'←0 (v' = 1-3) vibrational channels (black circles) with a Fano line shape fit convoluted with the appropriate Lorentzian response function (red line) for each data set. Extraction of the resonance energy (E_{res}), FWHM (Γ), and lifetime (τ) is achieved through the fitting.

3.4.2.1 Computational Analysis

Ab initio calculations were performed for CuO^- and the corresponding $^2\Pi$ neutral species using Gaussian 03 software [76] in order to confirm the existence of a DBS. The $^2\Pi$ DBS calculation was performed with the initial guess method employed by Ref[69], which recognizes the DBS as a neutral molecule with a loosely bound electron (lbe). The neutral molecule is first optimized with diffuse orbitals, and the extra electron is placed into a diffuse stable virtual orbital (e.g. LUMO+1, LUMO+2, etc.) which serves as the initial guess for optimization of the DBS. The calculated orbital is displayed in Figure 3.8 using MOLEKEL [70]. The choice of basis sets for the DBS were chosen according to Ref[71]. Aug-cc-pVDZ was used for both copper and oxygen atoms [72], with extra 3s3p2d diffuse functions added onto the copper atom due to its presence at the positive

charge end of the dipole moment. The exponents for the 3s3p functions were the same, starting from 5.383275E-03 and decreasing by a ratio of 2.87 [71]. This ratio was also used for the d functions starting from an exponent value of 2.296516E-02.

Since the dipole bound orbital is diffuse and lies well outside the neutral framework, a dipole bound $[CuO]^-$ ion should have a similar geometry to neutral CuO. The lbe imparts minimal distortion to the neutral geometry. The neutral species is optimized via the Hartree-Fock method with the basis set above to identify suitable virtual orbitals to accommodate the excess electron. For CuO, the beta extra electron was placed in the LUMO+1 and an MP2 single point energy calculation was performed to incorporate perturbation effects from the neutral species other electrons. The MP2 result indicates that the DBS electron binding energy (eBE) is 34.4 meV below the neutral $^2\Pi$ state at the neutral equilibrium geometry.

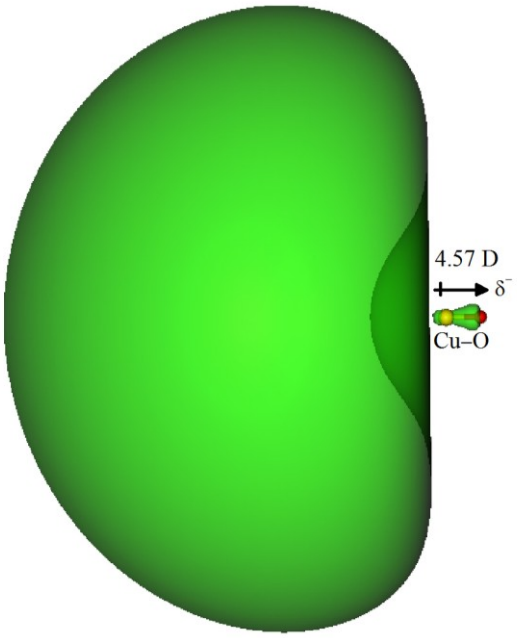

Figure 3.8: Side view of a calculated DBS orbital (green) corresponding to the dipole bound electron in the LUMO+1 of the neutral CuO species. Copper atom in yellow and the oxygen atom in red. The dipole moment of the neutral species is 4.57 Debye (D), with the negative charge density (δ^-) located on the oxygen atom.

The relative rise and fall in each vibrational channel cross section for $^2\Pi_\Omega(\Omega = \frac{3}{2}, \frac{1}{2})$ v′=1-3 [Figure 3.3] can now be interpreted with the support of this *ab initio* work. The dipole moment of CuO has been experimentally reported to have a value of 4.57 D [74] with the positive end located on the copper atom [Figure 3.8]. Through the orbital analysis presented here, this DBS is suggested to be a large s-type orbital and reside on the copper side of the molecule. The weak, diffuse state, corresponding to electron capture into the DBS, energetically resides just below its associated neutral electronic state (34.4 meV below the $^2\Pi_{3/2}$ state). This also implies that there will be a DBS vibrational level associated with each vibrational level for both the $^2\Pi_{3/2}$ and $^2\Pi_{1/2}$ spin-orbit states. Upon observation of Figure 3.1(d), it can be envisaged that this would be a congested region of vibronic states. With this information, we return to Figures 3.3, 3.4, & 3.7 for further discussion on the effects of DBSs on this energy region.

Increasing the photon energy past the $^2\Pi_{3/2}$(v′=1) threshold, the v′=1 channels opens. The DBS associated with the v′=2 channel will also be accessible about 30 meV below the v′=2 threshold. This is precisely where the relative intensity of the v′=1 channels begin to rise, reaching a maximum at about 40 meV higher in energy before tailing off to their relative FC factor intensities. As the v′=1 channel intensities fall, a similar effect is seen in the relative v′=2 channel intensities, and likewise the relative v′=3 intensities. Each time the DBS linked to the next highest vibrational level becomes accessible just below the v′+1 threshold.

Note, one reason we do not observe a rise and fall in the cross section for the 0←0 transition in Figure 3.3 is that we have arbitrarily scaled all spectra to this transition; hence, the effects of the v′=1 and v′=0 DBSs are not seen in Figure 3.3. The relative

maximum intensities of the vibrational levels can be explained by the respective FC factors for the transitions to each vibrational level. The transition strengths to higher vibrational levels in both CuO $^2\Pi$ spin-orbit states [seen in Figure 3.2(b)] have steadily decreasing FC factors. Thus, the absorption cross section to DBSs associated with these levels becomes less intense; therefore, you would expect the effect to be less intense for higher values of v′, which is exactly what is observed. Lastly, the extracted resonance energies of the DBSs [Figure 3.7, E_{res}], from our experimental data, lie slightly above their respective vibrational levels, suggesting we are detecting an averaging effect of the two spin-orbit states. As previously stated, the DBS should energetically lie below the respective neutral level; however, the spin-orbit splitting (34.6 meV) is not capable of being fully resolved by our instrument, making true detection of E_{res} difficult.

3.4.3 Interpretation of Spectral Assignments for Anionic Excited States

As mentioned previously, the feature reported by Wu et. al. [49] at a binding energy of 1.27 eV was originally assigned to the transition $^2\Pi_\Omega$ ($\Omega = \frac{3}{2}, \frac{1}{2}$)$\leftarrow{}^3\Pi_2$. In addition to this feature, a different CuO^- detachment band (eBE = 1.03 eV) was also observed by Wu et. al. [49] when CuO^- is produced by CuO_3^- dissociation. This feature was assigned as originating from a higher spin-orbit state corresponding to the transition $^2\Pi_\Omega$ ($\Omega = \frac{3}{2}, \frac{1}{2}$) $\leftarrow$ $^3\Pi_0$. The reasoning for these assignments was justified based on the energy splitting (~0.24 eV) and its correlation with the spin-orbit splitting of the ^2D_J ($J = \frac{5}{2}, \frac{3}{2}$) state in atomic Cu (0.25 eV). A theoretical study [61] employed DFT to study the anion excited states and claimed that the energy gap would be too large for the original

assignment. The calculated spin-orbit splitting ($^3\Pi_2$–$^3\Pi_1$–$^3\Pi_0$) was 17.85 meV. Therefore, the conclusion was the feature observed at an eBE = 1.03 eV must be detachment from the anion's $^1\Pi$ state. The absence of the transition originating in the $^1\Pi$ state from our data, as well as Wu et. al.'s single photon data, suggests that the formation of this excited anion state is the result of the photodissociation fragment of CuO^- from CuO_3^- rather than direct detachment in either ion source.

Returning to our 710 nm image in Figure 3.6, the width of the 1.27 eV transition could be interpreted as many transitions occurring within a small energy range. Figure 3.9 displays possible transitions from the anion $^3\Pi$ state to the neutral $^2\Pi$ state, using the theoretically calculated spin-orbit splitting value from Ref[61] (17.85 meV). Ω = 0, 1, 2 for the $^3\Pi$ state and $\Omega = \frac{3}{2}, \frac{1}{2}$ for the $^2\Pi$ state, making a total of six transitions to the neutral possible. Also shown in Figure 3.9 is a simulated spectrum using FC factors based on the available experimental data and theoretical parameters available for this transition. The agreement is good, consistent with an interpretation invoking a small spin-orbit splitting.

The previously mentioned angular distribution of β(0.48 eV) = +1.6, indicates parallel detachment with the laser polarization. This positive nature can be qualitatively explained by the s & p model described in Ref[75]. The model uses the elements from the point group of the molecule and considers electronic detachment in the molecular frame, which requires the direct product of the final state (ψ_f, composed of the free electron and neutral state wavefunctions), molecular frame dipole operator (μ_{MF}), and initial state (ψ_i) irreducible representations to be invariant under the symmetry operators of the molecule's point group:

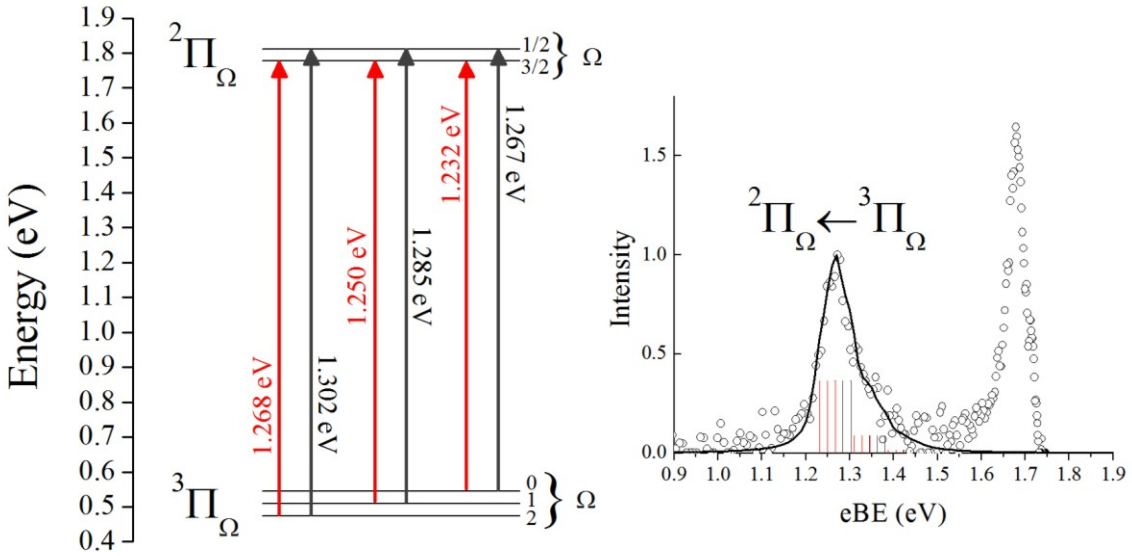

Figure 3.9: Energy level diagram (left) with vertical arrows representing the six possible electronic detachment energies for the $^2\Pi_\Omega \leftarrow {}^3\Pi_\Omega$ transition. The energy scale is relative to the anion ground state ($^1\Sigma^+$, not shown). (right) CuO^- photoelectron energy spectrum at 710 nm (open circles) with a Franck-Condon analysis stick spectrum (red & gray) and convoluted spectrum (black solid line).

$$\Gamma(\psi_f) \otimes \Gamma(\mu_{MF}) \otimes \Gamma(\psi_i) \supseteq \Gamma_{TotSym} \tag{3.2}$$

where Γ indicates the irreducible representation and Γ_{TotSym} is the totally symmetric irreducible representation. The allowed symmetries of the free electron wave are then extracted from ψ_f and expanded on a single-center atomic orbital basis, and an approximation is applied assuming electron $\ell \leq 1$ waves are the main contributing terms in the PAD at low eKEs. These molecular frame s and p-waves are then interpreted in the laboratory frame axis, defined by the laser polarization (ε). For the CuO^- $^2\Pi \leftarrow {}^3\Pi$ transition ($C_{\infty v}$ point group), both initial and final states are of Π symmetry and the totally symmetric irreducible representation is Σ^+ symmetry. The dipole operator in the molecular frame (μ_{MF}) translates as Σ^+ in the z orientation and Π in the x and y orientation. If the laboratory frame z-axis is equivalent to the molecular frame z-axis, the

allowed free electron symmetries are s and p_z waves, both corresponding to parallel detachment along the laser polarization axis (i.e. – positive β values). For a laboratory frame z-axis oriented along the molecular frame x or y axis, the allowed free electron symmetries are p_x and p_y waves, both again corresponding to parallel detachment along the laser polarization axis. Assuming a random orientation of molecules prior to detachment, one would expect the laboratory frame PAD to contain strong positive character, which is exactly what is observed at an eKE = 0.48 eV (β = +1.6).

By combining our experimental observations with theoretical work and a qualitative explanation of the anisotropy with the s and p model, it becomes reasonable to claim that this broad feature is entirely due to detachment from the excited anion $^3\Pi$ state.

3.5 Summary

Photoelectron imaging studies on the CuO anion near the threshold region associated with the neutral CuO $^2\Pi$ state has provided valuable information in regards to DBS vibrational channels. CuO neutral's high dipole moment (4.57 D) was found to support vibrational levels associated with a temporary DBS, which lies energetically just below the neutral $^2\Pi$ state and all associated vibrational levels. Excitation to a DBS vibrational level (v′) resulted in enhancement of the $^2\Pi$ state v′−1 channel cross section, and lifetimes for the DBS v′ = 2-4 levels were measured to be 50.6, 38.3, and 40.4 fs respectively. These low energy electrons are temporarily captured by the neutral's dipole moment and undergo approximately one CuO vibrational period before ejection. While this is true for DBS v′ ≥ 1 levels, the DBS v′ = 0 level, lying energetically below the neutral, should be stable with respect to electron loss, as there is not enough energy input

for detachment. This experimental evidence for temporary and stable DBSs, with respect to electron loss, has proven to be an effective method for controlling electron-neutral interactions and dipole bound anion formation.

The observation of a CuO^- detachment feature at an eBE = 1.27 eV was assigned to represent detachment from the $^3\Pi$ excited anion state to the $^2\Pi$ neutral ground state. With the aid of previous theoretical work [61], a simulation of the energy spectrum proved to be a good fit to the experimental work. This evidence for stable excited anion species provides more incentive for theoretical groups to search and develop working models for other metal oxide excited anion states. As we shall see in the next chapter about the copper dioxide anion (CuO_2^-), electrons detached from excited anion states may be more common than previously thought.

Chapter 4

CuO_2^-: A Dissociation Study using Frequency and Time-Resolved Methods

4.1 Introduction

Reactivity of copper atoms with oxygen has been the subject of extensive research based on their availability and for their emerging properties which range from corrosion to catalytic oxidation for oxygen transport in biocomplexes [77]. In particular, cuprates are popular anions among the field of superconductivity in the search for the existence of high (room) temperature superconductors. Previous research has shown the importance of having layers of CuO_2 contained in the lattice of superconductors and their quantity dependence for raising the molecule's critical temperature [78-81].

Early experimental work on CuO_2 using matrix infrared absorptions revealed various geometries of the species [82-84], in which assignments for the linear isomer were refined by a later study [56]. The linear isomer was first observed and assigned in photoelectron spectroscopy from a study performed by Wu et. al. [85]. This initiated a series of theoretical work [57,86,87,89] in attempt to establish the energetically ground state geometry of the triatomic species, in which the bent (CuOO) and linear (OCuO)

isomers are the two competing geometries. A detailed theoretical work using density functional theory (DFT) on the linear isomer was done by Deng et.al. [88], which relates closely to our experimental results as well as Wu et. al. Therefore, we adopt their electronic state assignments for the anion and neutral species, in which we use our own labeling scheme within the energy diagram provided in Figure 4.1. Referral to Figure 4.1 will emerge later in the discussion.

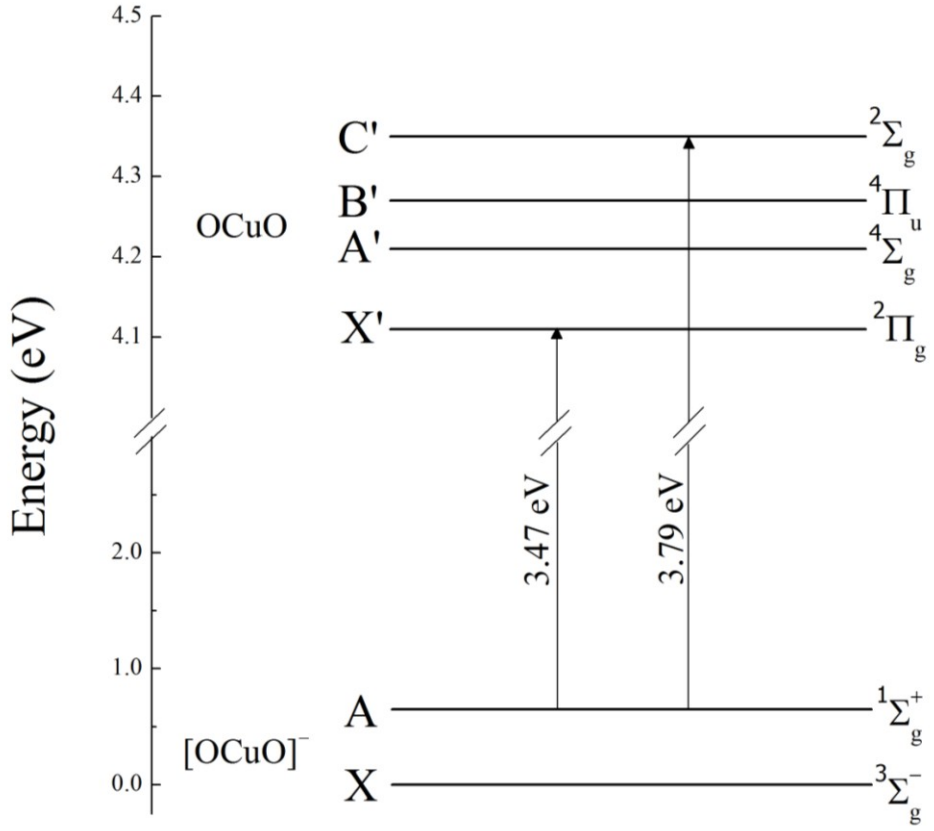

Figure 4.1: Energy diagram of electronic states for the anion and neutral CuO_2 species. The state energies were calculated using a combination of experimentally observed transitions [85] and term symbols assigned according to a theoretical study [88]. The new labeling scheme (X, A, etc.) is shown to the left of the electronic state.

Wu et. al. [85] obtained a series of photoelectron spectra of CuO_2^- at three higher ordered harmonics (532 nm, 355 nm, 266 nm), and observed the bent isomer at lower

photon energies as well as the linear isomer at higher photon energies. Along with this observation, at the two lower energy harmonics, a Cu^- fragment signal appears from the CuO_2^- species dissociating by absorption of an initial photon and detection of its anion fragment by a second trailing photon within the same laser pulse. This dissociation process was assigned to the bent isomer due to its weakly-bonded nature. Despite the evidence for the existence of this bent isomer in their negative ion photoelectron study, our source conditions only generate the linear isomer anion; however, we still observe the Cu^- fragment signal in our spectrum. The nature of this dissociation is observed in more detail throughout the rest of this chapter, where we employ the combination of nanosecond laser spectroscopy and time-resolved photoelectron spectroscopy (TRPES) [Section 1.4] for probing the reaction.

4.2 Experimental

Photoelectron images for nanosecond data were collected at a series of photon wavelengths from 305–765 nm. CuO_2^- molecular anions were generated by flowing 50-70 psi of O_2 gas (99.0% purity) through a pulsed nozzle (10 Hz repetition rate) into the discharge apparatus [Section 2.1]. During operation the ion source chamber was maintained at a pressure between 6×10^{-6}-1×10^{-5} Torr. The ^{63}Cu and ^{16}O isotopic peaks were selected for analysis due to highest yield in the mass spectrum.

For pump-probe time domain experiments [Section 1.4], 80 psi of O_2 gas (99.0% purity) is flowed through a pulsed nozzle (50 Hz repetition rate) into the discharge apparatus, maintaining source chamber pressures between $1\text{-}2\times10^{-5}$ Torr. A regeneratively amplified Ti:Sapphire laser system (Spectra Physics, Tsunami and Spitfire

Pro) produces 2 mJ, 120 fs pulses at 800 nm. The output is divided using a 50% beam splitter into two beams (pump & probe). The pump is frequency doubled using a Beta Barium Borate (BBO) crystal producing 150 μJ per pulse at 400 nm output. The probe travels down a motorized translation stage, providing an optical delay between the pump and probe pulses. The two beam paths are recombined prior to entering the detection region and synchronized with the arrival time of the CuO_2^-. Both beams are gently focused prior to the to the detection region by a lens (focal length 1 m), with estimated beam diameters of 3 mm (800 nm) and 6 mm (400nm) at the point of interaction.

All collected images are reconstructed using the BASEX program of Dribinski et. al. [3] allowing extraction of the photoelectron spectrum.

4.3 Results

4.3.1 Higher Photon Energy Spectra

A selection of electron binding energy (eBE) domain spectra are shown in Figure 4.2, scaled relative to the highest intensity peak in the individual spectrum. Figure 4.2(a) displays the 305 nm ($h\nu$ = 4.07 eV) CuO_2^- photoelectron spectrum. The observed transitions are consistent with those previously reported to be due to detachment from a linear CuO_2^- isomer. The states associated with these transitions have been assigned according to previous experimental and theoretical work [49,85,88] although our notation is different [see Figure 4.1], reflecting the parent anion and daughter neutral states. The neutral states will be further labeled with a single dash for distinction from the anion. The ground state of linear CuO_2^- has been determined to be a triplet, $X(^3\Sigma_g^-)$. states. According to calculations [88], the spectral feature we observe at eBE = 3.47 eV

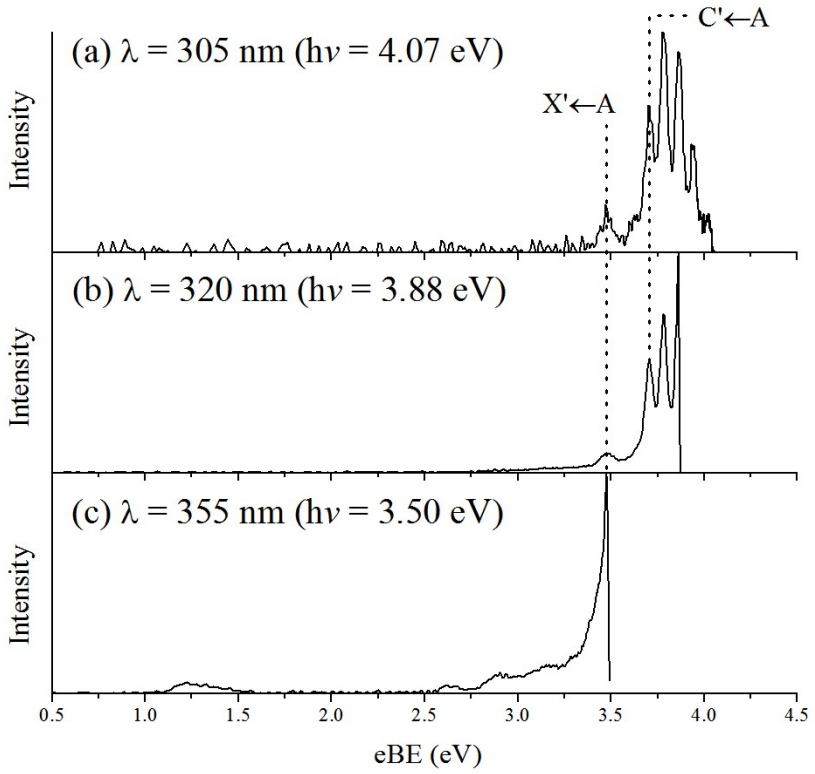

Figure 4.2: Detachment from CuO_2^- at three different photon wavelengths. At high photon energies [(a) and (b)] transitions X' ← A and C' ← A are observed, but as the photon energy is lowered near the X' ← A threshold (c), new lower binding energy features emerge.

corresponds to detachment from the first excited state of the linear CuO_2^- anion to the ground state of the neutral; $X'(^2\Pi_g) \leftarrow A(^1\Sigma_g^+)$. The series of closely spaced transitions starting at 3.79 eV also originate in the $A(^1\Sigma_g^+)$ state of CuO_2^- but end in the neutral C' state which is designated the term symbol $^2\Sigma_g$. The structure within this band is predominantly due to vibrational excitation of the neutral molecule and the average peak to peak separation is 630 cm^{-1}, also consistent with previous calculation [88]. For completeness we note that transitions from the $X(^3\Sigma_g^-)$ anion state have been observed previously [85], but these are found at higher photon energies than employed in our experiments.

At 320 nm [Figure 4.2(b), hν = 3.88 eV] the spectrum is rather similar to that at 305 nm, the absence of the higher eBE features merely reflecting the reduction in photon energy. However, it is noticeable in Figure 4.2(c) that as the photon energy is reduced, lower eBE features become apparent in the spectrum below the X' ← A transition threshold.

4.3.2 Cu^- Fragment and Low eKE Features: Detection with Nanosecond Pulses

The origin of three of these lower eBE features seen in Figure 4.2(c) can be ascribed to detachment from atomic Cu^- anions. This is clearly seen in Figure 4.3(a) where the photoelectron spectrum recorded for a free Cu^- anion at 355 nm (red line) is overlaid on that of the 355 nm molecular anion (shaded in grey). The three peaks in the Cu^- spectrum, correspond to detachment via the first three electronic states of the Cu atom, $^2S_{1/2}$, $^2D_{5/2}$, $^2D_{3/2}$. Figure 4.3 also shows that although the atomic transitions seen in the CuO_2^- experiment might seem rather broad for atomic detachment (particularly the $^2S_{1/2}$ feature), the width of the transition is largely due to instrument broadening, a facet of the momentum space imaging technique in which the eKE resolution decreases as the speed of the electrons increase. The origin of the Cu^- ions which produce this contribution is a photoinduced fragmentation process. Leading photons from the ns laser pulse excite the molecular anion to some dissociative state and trailing photons within the same laser pulse detach electrons from the Cu^- product [Section 1.4].

This phenomenon has been reported previously for CuO_2^- [85], although as discussed later, we suggest a different origin for the fragmentation process. The different photon power dependence of the Cu^- component of the spectrum is demonstrated in Figure

4.3(b), where the 3.0 - 3.5 eV region is scaled to the height of the Cu($^2S_{1/2}$) peak. The intensity of the X'($^2\Pi_g$) ← A($^1\Sigma_g^+$) feature (eBE = 3.47 eV) increases relative to the Cu($^2S_{1/2}$) peak as the pulse energy decreases, and a similar trend is seen across the whole of the 3.0 - 3.5 eV region.

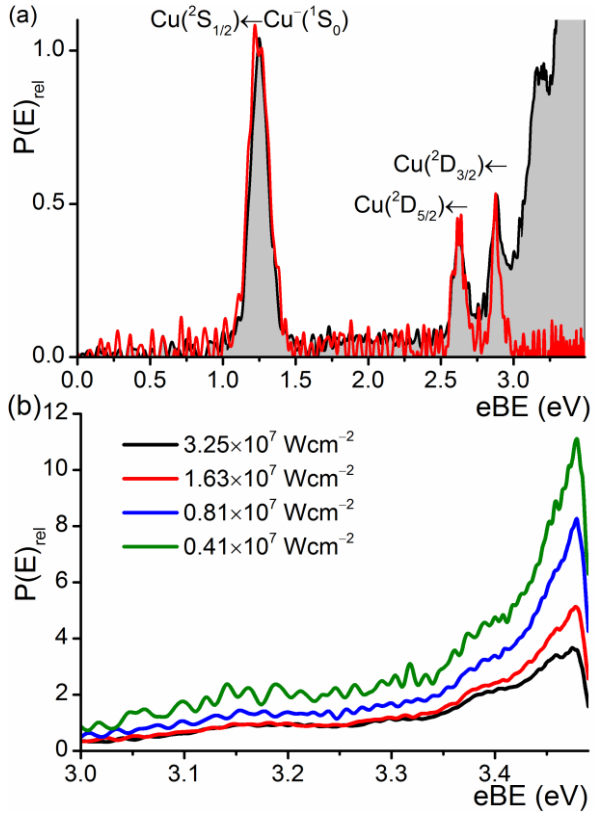

Figure 4.3: (a) 355 nm energy spectrum (filled gray) overlapped with Cu^- energy spectrum (red line), showing good agreement with lower binding energy features. (b) Laser power density dependence of the higher binding energy features scaled relative to the Cu^-($^2S_{1/2}$) peak (not shown). Shows linear dependence of features as power density is varied.

In Figure 4.4 we show spectra recorded below the direct detachment threshold of CuO_2^-. Care must be taken in reading these spectra. Figure 4.4(a-c) images were acquired using 4-6 mJ laser pulses while (d) used estimated 15-20 mJ pulses due to a suspected weak cross section. The spectra of Figure 4.4 are scaled relative to the height of the most intense transition and so the behavior of the cross section for Cu^- production

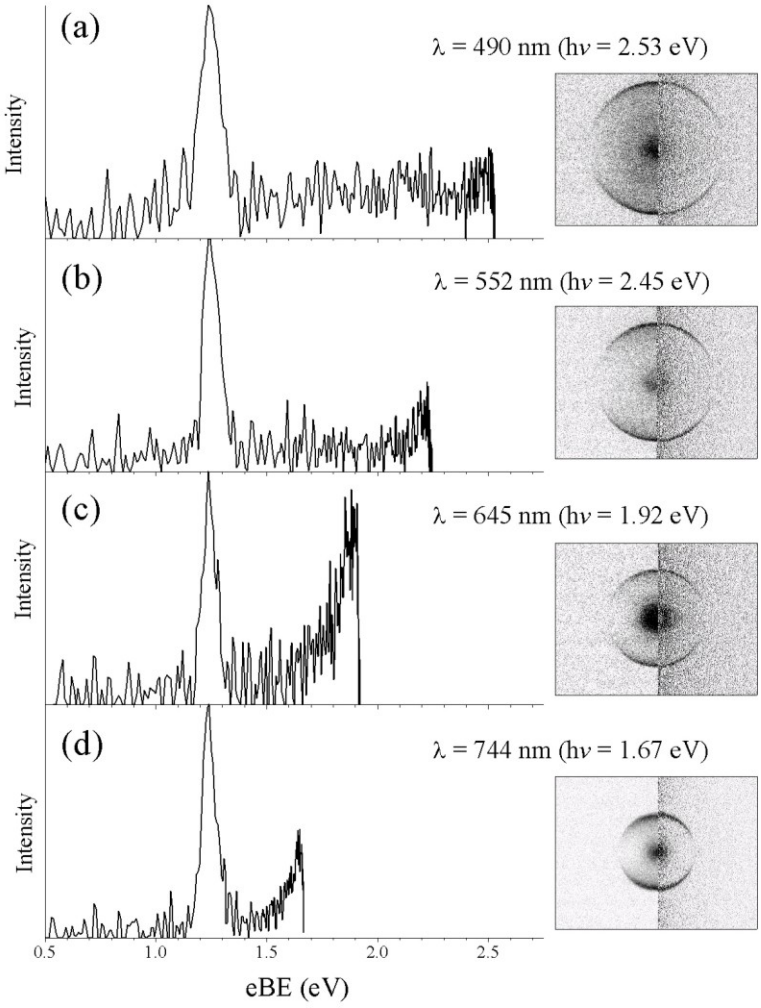

Figure 4.4: Four images (vertical laser polarization) taken below the X' ← A detachment threshold (eBE = 3.47 eV). Cu^- fragments are detected (eBE feature at 1.24 eV) along with a central feature at all wavelengths shown. Left half of image is the raw image, right half is the reconstructed image.

cannot be directly extracted. Nevertheless, there are important related facets of these spectra. The Cu^- fragment is produced over a large range of detachment energies. In fact, we have observed Cu^- fragments at photon energies as high as 3.65 eV and as low as 1.62 eV, the lower limit representing the limit of our dye laser range. There is evidence for photoelectrons produced with apparent binding energies between 1.5 and 3.0 eV which are not readily apparent in the 320 and 305 nm spectra. All images taken below

threshold show a peak in the spectrum at low eKE (eBE close to the photon energy), some more apparent than others. This behavior is perhaps clearer to see in the images shown to the right of the corresponding spectra. These provide a quick visual demonstration of the variation of the ratio between the low eKE feature and the Cu^- fragmentation as the excitation wavelength is changed. Rather harder to make out in the images is the fact that there is also an appreciable tail leading toward the central feature to higher eKE (lower eBE). The origin of these photoelectrons will be discussed later.

4.3.3 Detection of Cu^- Fragment using Femtosecond Time-Resolved Photoelectron Spectroscopy (TRPES)

It is clear that an appreciable amount of Cu^- is produced on a timescale equivalent to the width of the ns laser pulse (5-8 ns). In order to gauge the timescale for Cu^- production a femtosecond (pulse width 120 fs) pump-probe TRPES imaging study was performed using a 400 nm excitation (pump) pulse and an optically delayed 800 nm probe pulse. Four images are accumulated, (A) both pump + probe laser, (B) probe only, (C) pump only, and (D) background only.

In these experiments the probe laser (B) produces no discernible photoelectron signal unless preceded by the pump laser. Representative (A) and (C) images are shown in Figure 4.5 at a pump-probe delay of 260 ps. The pump laser (400 nm) produces the isotropic feature in the center of the images, but only when the pump precedes the probe do we see the outer feature (A). A combination of A – B – C + D (also shown in Figure 4.5) removes any signature of single photon detachment.

The central feature seen in images (A) and (C) is clearly the result of a single photon detachment process. This is fortuitous as it gives a means to assess the change in the Cu^-

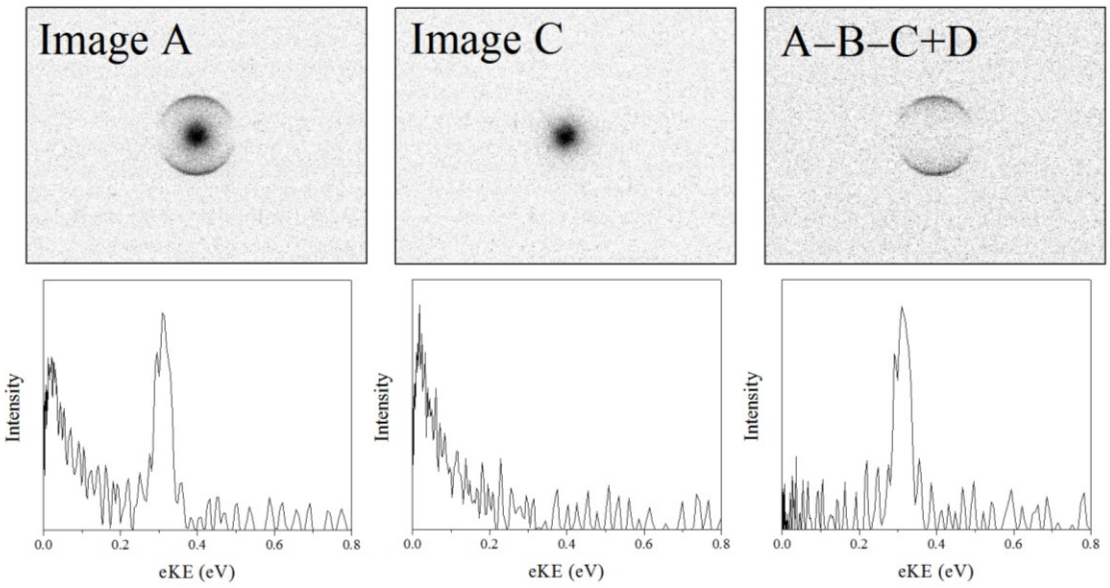

Figure 4.5: Images accumulated during a TRPES experiment with a 260 ps time delay between the pump and probe pulses (both vertical polarization). Image A: both pump and probe. Image B: probe only (800 nm). Image C: pump only (400 nm). Image D: background. The combination A – B – C + D yields the final two photon signal. Images B and D were omitted due to containing only background noise. Corresponding eKE spectra located below the respective image.

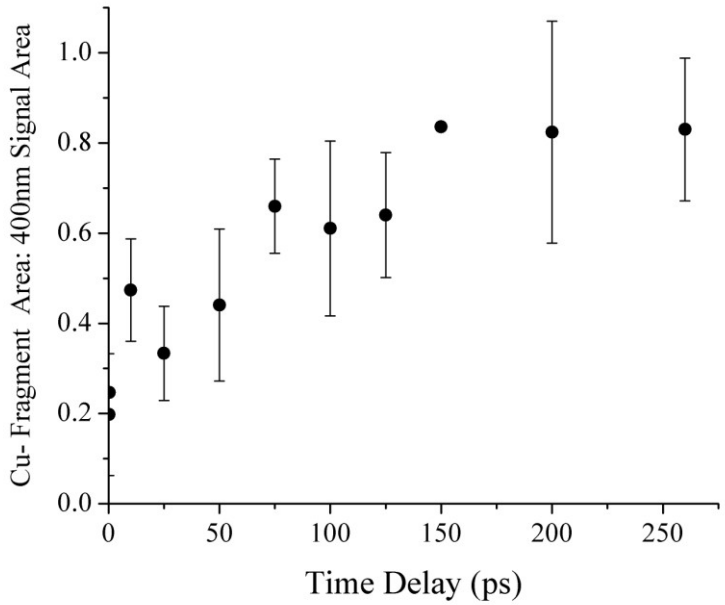

Figure 4.6: The integrated area of the Cu ($^2S_{1/2}$) peak (A−B−C+D) and the integrated area of the 400 nm signal (Image C) ratios as a function of time delay between the pump and probe laser pulses.

photoelectron yield as a function of time, effectively providing a reference signal. The integrated area under the Cu ($^2S_{1/2}$) peak in the spectrum, extracted from image (A), is divided by the integrated area under the higher eBE peak in the same spectrum. The variation in this ratio as a function of delay time is plotted in Figure 4.6 and, although the error bars are rather large, shows a steady increase in the relative photoelectron yield (i.e. Cu^- yield) as a function of pump-probe time delay. Perhaps most striking is the long timescale during which the Cu^- signal continues to rise, seeming to level off at around 150 ps, suggesting a long lifetime for the photoexcited state produced as the precursor to dissociation, particularly in comparison to a typical vibrational period.

4.4 Discussion

4.4.1 Spectral Assignments for detachment from linear CuO_2^-

A previously reported approximation to visualize bonding in linear OCuO was to assume charge transfer between the oxygen and copper to be O^- Cu^{2+} O^- [83,85]. This approach takes into account a 13 electron system and ignores the contribution of transition metal d-orbitals, but was believed to be a good qualitative estimation to explain specific transitions reported by Wu et. al. [85]. They explained using molecular orbital theory that the ground states for CuO_2 and CuO_2^- were respectively $^2\Sigma_g$ and $^1\Sigma_g^+$. Theoretical work challenged this approximation with the aid of LSDA and GGA calculations on orbital populations [88]. They found that the d-orbitals have significant contribution to bonding in the valence orbitals and the 13 electron system would be a poor approximation. Also of interest, this orbital analysis predicts the electronic configuration for the anion to be:

[core]$(5\sigma_g^+)^2(4\sigma_u^+)^2(6\sigma_g^+)^2(1\pi_g)^4(1\delta_g)^4(5\sigma_u^+)^2(3\pi_u)^4(7\sigma_g^+)^2(2\pi_g)^2$ forming two electronic states, $^3\Sigma_g^-$ and $^1\Sigma_g^+$, the triplet being lower in energy [Figure 4.1]. While populated anionic excited states are rare, they have been experimentally observed [89] and theoretically proven to exist [90]; therefore, it is reasonable to assume that a transition can originate in an excited anion electronic state, in which we confidently assign the first two energetically observable transitions, X' ← A and C' ← A [see Figure 4.1].

4.4.2 Fragmentation of CuO_2^-

As previously mentioned, Wu et. al. [85] also observed the Cu^- fragments in their energy spectra at the same photon energies. Also observed in their energy spectra is a feature at significantly lower binding energies than the linear isomer, and based on previous spectroscopic studies [83,95,96] they assigned this vibrational band at an eBE = 1.50 eV (absent in our spectra) to be detachment from a bent isomer ($CuOO^-$), where an O_2 molecule is bound to the Cu atom by one O atom forming a bent structure (C_s symmetry). This assignment is in good agreement with theoretical studies [89]. Based on a prior dissociation study of $OCuO^+$, where they found the major dissociation product to be CuO^+ [97], they assigned the Cu^- fragment signal to dissociation of this bent $CuOO^-$ isomer, due to the absence of CuO^- or O^- fragments in their spectra. Energetically, this is a reasonable assumption; however, our energy spectra see no trace of this bent isomer signal at a binding energy of 1.50 eV, yet we still observe the Cu^- fragments at the same wavelengths. The absence of the bent isomer could easily be attributed to different methods for anion formation. We employ the discharge method [Section 2.1] while Wu et. al. employ laser ablation of a Cu target, and while both

methods work in generating Cu based molecular anions, it is important to point out that anion formation is highly dependent on source conditions. While we cannot comment on the dissociation process of the bent isomer in their spectra, we can use the absence of the bent isomer in our spectra to our advantage; hence, we conclude that the source of the Cu^- fragment in our spectra must be due to dissociation of the linear [$OCuO^-$] anion via one photon process.

The possible dissociation processes for yielding Cu^- product from a signal photon absorption in the linear isomer are shown in Equation 4.1:

$$\begin{aligned} [OCuO^-] + h\nu &\longrightarrow O + Cu^- + O && \text{(I)} \\ &\longrightarrow [CuO]^- + O \longrightarrow Cu^- + O + O && \text{(II)} \\ &\longrightarrow [OCuO^-]^* \longrightarrow Cu^- + O_2 && \text{(III)} \end{aligned} \qquad (4.1)$$

Channel (I) represents the simultaneous dissociation of both Cu−O bonds, presumably from a strong excitation of the symmetric stretching mode, and upon dissociation of the two bonds, the extra electron would reside on the Cu atom. Channel (II) represents the sequential dissociation of both O atoms from the Cu, first producing an intermediate state of excited CuO^- and O after the first Cu−O bond dissociation, and then breaking the second Cu−O bond leading to the final product Cu^-. Channel (III) represents the formation of a bent isomer from the initial excitation of the linear isomer, it is presumed that this bent isomer is formed along a dissociative curve, ultimately leading to the products $Cu^- + O_2$. An energy diagram including the asymptotic limits for the three possible dissociation channels are compared with the molecular anion and neutral (bent & linear) energy levels in Figure 4.7:

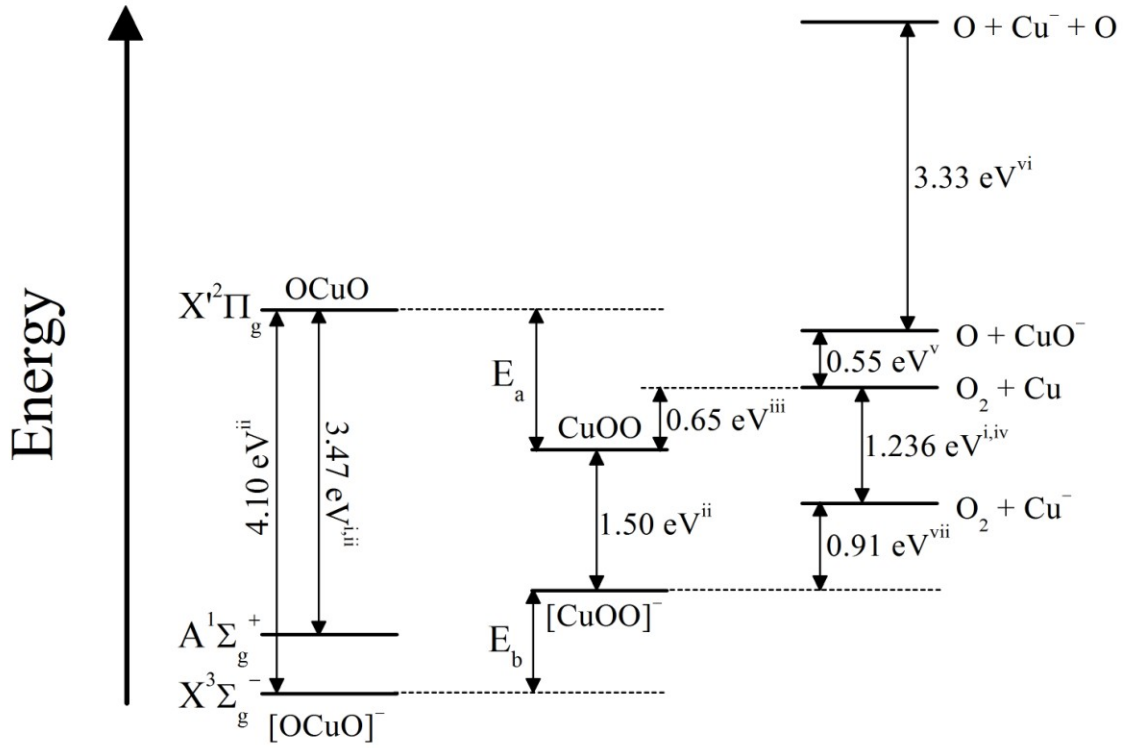

Figure 4.7: Energy diagram of the linear isomer (left), bent isomer (middle), and dissociation channel (right) energy levels. Energy gaps labeled from experimental values: (i) This work (ii) Ref[85] (iii) Ref[90,91] (iv) Ref[92] (v) $D_e(O_2) - D_e(CuO) - EA(CuO)$ (vi) $EA(CuO) + D_e(CuO) - EA(Cu)$ (vii) $EA(CuOO) + D_e(CuOO) - EA(Cu)$. E_a and E_b represent experimentally unknown energy values.

The known experimental values of EA(Cu) [92], D_e(O2) [93], EA/D_e(CuO) [60], and EA/D_e(CuOO) [85,90,91] were used to create the energy diagram, with energy gaps labeled where appropriate. The relative energies of the anion and neutral states have been well characterized by photoelectron spectroscopy [49,85]. The dissociation energy (D_e) of the neutral bent isomer (CuOO) has been previously measured, however, the uncertainty is quite large (0.65±0.22 eV). Using this value, we obtain an estimate for the lower lying anion fragmentation channel, $[CuOO]^-$ (0.91±0.22 eV). No experimental data exists energetically relating the linear-to-bent-neutral [Figure 4.7 (E_a)] or the linear-

to-bent-anion [Figure 4.7 (E_b)], although multiple theoretical studies suggest the linear anion isomer is the more stable species [89,94]; hence, E([CuOO]$^-$) > E([OCuO]$^-$). Aside from this general consensus, it should be noted that the reported calculations are highly sensitive to the methods and basis sets used [56,57,88,89,94,96,98-101]. Two DFT studies have directly compared the anion and neutral isomers [89,94]. They reported values of E_a = 0.52 eV (DFT-GGA, ignoring spin polarization) [89] or 0.36 eV (DFT-GGS, including spin polarization) [94], and E_b = 1.10 (DFT-GGA) or 1.92 eV (DFT-GGS). These calculated values are not consistent with the photodetachment results, as it can be shown from Figure 4.7 that E_a and E_b are constrained to E_a+E_b = 2.60 eV; however, inclusion of spin polarization brings the calculations to within 0.32 eV of achieving energy balance. With this added knowledge and aid from Figure 4.7, let us reexamine the dissociation processes in Equation 4.1.

From an energetic standpoint, the method of Channel (I) dissociation seems unlikely. Assuming the initial process starts in the linear $A^1\Sigma_g^+$ state, the energy input in the form of a photon would simply not be feasible to reach such a high dissociation energy (~6 eV from the higher lying [CuOO]$^-$ state). While the Channel (II) intermediate state lies significantly lower in energy than Channel (I) dissociation (3.33 eV), it would still require a similarly large energy input to dissociate the [CuO]$^-$ species with a single photon. This leaves Channel (III) as the most energetically reasonable dissociation process, as the product state lies E_b+0.28 eV above the [OCuO]$^-$ $A^1\Sigma_g^+$ state. Our experimentally observed Cu^- fragments from nanosecond experiments, in which the Cu^- has been observed at photon energies as low as 1.62 eV, now have implications for possible values of E_b. Assuming production of the linear anion in the $A^1\Sigma_g^+$ state, the

energetic upper limit for E_b is 1.34±0.26 eV, accounting for 0.04 eV uncertainty for the dissociation energy for the linear anion to $O_2 + Cu^-$ product. This upper limit is in agreement with the DFT-GGA prediction but significantly less than the more sophisticated DFT-GGS prediction. Additionally, this sets the lower limit for E_a = 1.26±0.28 eV, which is vastly different than any predicted values to date, the majority of which are < 0.6 eV [56,89,94,96,98-101]. This seems to suggest that additional theoretical work is required to make any accurate comments about energy gaps between isomers of CuO_2, but combination of our experimental evidence with current theory does give a slightly quantitative edge on the fragmentation process.

Furthermore, the Channel (III) fragmentation to $O_2(^3\Sigma_g^-) + Cu^-(^1S_0)$ corresponds to a state with a total spin quantum number of 1 (S = 1). This would suggest the transition $O_2+Cu^- \leftarrow A^1\Sigma_g^+ [OCuO]^-$ (S = 0) is radiatively forbidden (i.e. $\Delta S \neq 0$); however, the long timescale (~150 ps) for production of the Cu^- fragment signal in the time-resolved experiments [Figure 4.6] suggests a substantial barrier to dissociation and the strong possibility of interstate coupling subsequent to initial excitation.

4.4.2.1 Central eKE Feature

Broad, low kinetic energy features are observed in the 355 nm spectra [Figures 4.2 & 4.3] as well as the lower photon energies [Figure 4.4]. They appear as intense photoelectron signals near the center of the images that tail off at higher eKE, with higher photon energy spectra containing relatively longer electron tails (i.e. higher eKE electrons). We note that Wu et. al. [85] also observed a similar photoelectron

background in their 355 nm spectrum, which underlies the non-linear peaks, and also in their 532 nm spectrum, showing an electron tail leading towards higher eKE.

In this work, we observe this unstructured photoelectron signal near low eKEs at wavelengths between 355-765 nm (hν = 3.49-1.62 eV). While there are neutral isomers of $[CuO_2]^-$ that have lower detachment energies than the linear anion, we rule them out as a source for the signals based on their lack of generation through our source conditions. In the eBE domain spectra [Figure 4.4], the photoelectron signal always seems to extend to energies close to the photoelectrons produced from the Cu^- fragments.

The production of such photoelectrons is clearly not from a direct single photon detachment process. We note two possible processes for production of this feature:

$$\begin{aligned} &OCuO^- \xrightarrow{h\nu_1} [OCuO^-]^* \xrightarrow{h\nu_2} OCuO + e^- \qquad \text{(IV)} \\ &OCuO^- \xrightarrow{h\nu} [OCuO^-]^* \longrightarrow OCuO + e^- \qquad \text{(V)} \end{aligned} \tag{4.2}$$

Process (IV) is a two photon process, which could feasibly occur as the excited anion $[OCuO^-]^*$ traverses the dissociation coordinate. In the asymptotic limit, this process is the origin of the Cu^- fragment signals observed in the nanosecond spectra. Although the excitation energy is different in the femtosecond time-resolved experiments, we report the only two photon signal observed at various time delays is from Cu^- fragments. Process (V) represents an autodetachment process in which the excited anion state $[OCuO^-]^*$ relaxes to a lower lying neutral state via electron loss. In order for the autodetachment process to be possible, there must be a neutral state that lies energetically below the photoexcited anion.

From a speculative standpoint, Process (IV) is illustrated in Figure 4.8 for the nanosecond and femtosecond kinetic energy spectra. For both cases, the initial photon

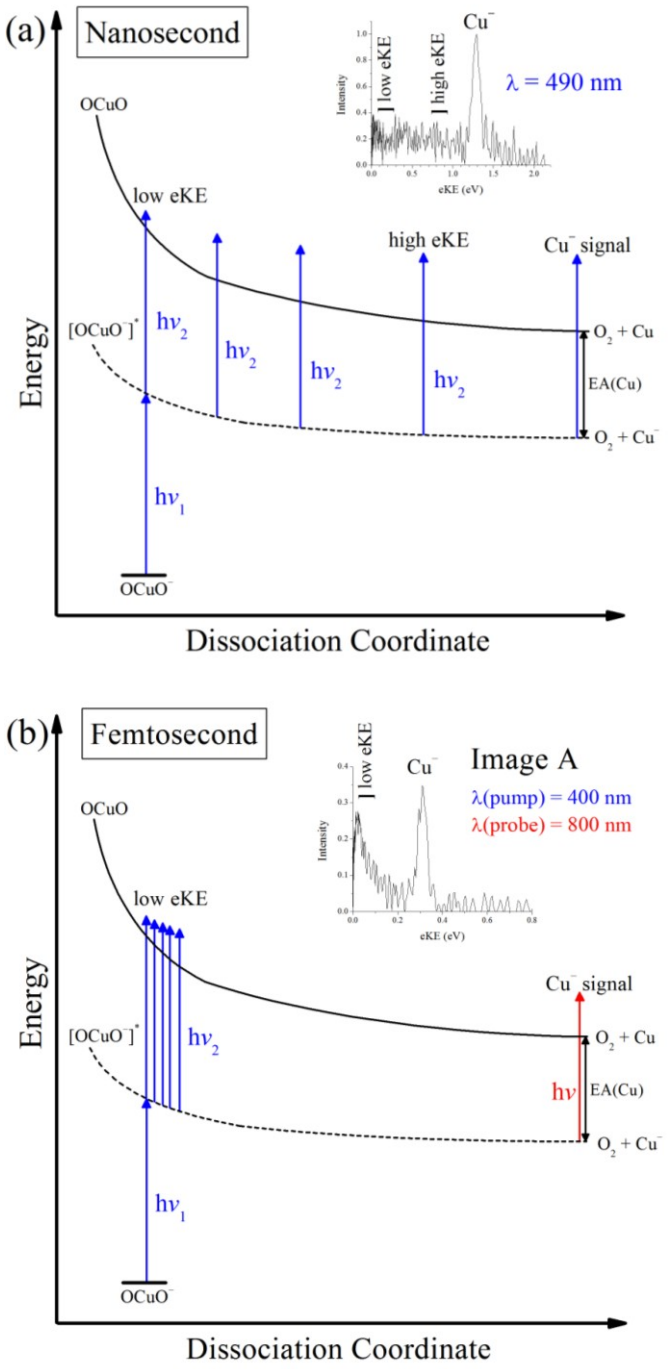

Figure 4.8: One-dimensional (1D) energy schemes for the dissociation process associated with the excited anion $[OCuO^-]^*$. (a) Nanosecond (ns) time domain for a 490 nm ns pulse. The pulse width allows the system to sample the whole dissociation coordinate with secondary photons ($h\nu_2$), within the same pulse, detaching electrons at various points along the curve, accounting for low, high, and Cu^- signals in the energy domain spectrum. (b) Femtosecond (fs) time domain for a pump-probe experiment. The pulse width is much shorter (~120 fs) allowing a smaller range on the dissociation coordinate to be sampled, accounting for a shorter electron tail in the energy domain spectrum.

($h\nu_1$) excites the linear anion to an excited dissociative state $[OCuO^-]^*$ (dashed line) below the neutral state (upper black line). Within the same pulse a second photon ($h\nu_2$) excites $[OCuO^-]^*$ to a neutral state, whereupon the electron is ejected with some kinetic energy.

The amount of kinetic energy is dependent on the temporal width of the pulse and the time delay between $h\nu_1$ and $h\nu_2$ (loosely related to position on the dissociative curve). For a nanosecond pulse, the temporal width is long enough for secondary photons to sample the entire dissociative coordinate, producing low eKE signal at short time delays and high eKE signal at longer time delays. The asymptotical limit (i.e. completed dissociation) produces the Cu^- detachment feature. For a femtosecond pulse (~120 fs), the secondary photons can sample only a small section of the excited dissociative curve; hence, producing an eKE signature without a long photoelectron tail [Figure 4.5 (Image C)]. The probe pulse then detaches the Cu^- fragment at a certain temporal delay. As the time delay (Δt) between the pump and probe pulses increases, the probe pulse is allowed to sample different points along the dissociation coordinate, eventually probing the dissociation channel at the asymptotic limit ($\Delta t = \infty$) where the energy gap between the neutral and anion curves converge to the EA of Cu (1.236 eV).

It is important to point out this 1D pictorial representation of dissociation may be overly simplistic. Our femtosecond data [Figure 4.6] indicates that the asymptotic limit for production of Cu^- fragments occurs on a long timescale (~150 ps), suggestive of an energetic barrier to dissociation, which is not indicated in Figure 4.8. Despite this unknown variable we are still able to make useful determinations.

The electron tail is only observed at eKEs no greater than the Cu^- fragment signal. This indicates the curvature associated with the excited anion state $[OCuO^-]^*$ along the dissociation coordinate is less steep than the neutral curve associated with this coordinate, with the closest energetic gap being the asymptotic limit. This suggests the highest eKE the energy spectra can achieve is the eKE associated with the Cu^- fragment signal, which is exactly what is observed in our spectra.

While Process (IV) seems to be the more likely source of this central eKE feature, we cannot completely rule out Process (V). The unknown energy of this dissociative curve creates large uncertainty in the energies associated with any lower lying neutral states for which the autodetachment process could occur. To the best of the author's knowledge, no theoretical work has suggested any neutral CuO_2 structures to energetically lie far below the bent isomer (CuOO), making this the most likely candidate for the final state of the autodetachment process. Using the estimated value of E_b [Section 4.4.2], the energy gap between the linear anion A state and neutral bent ground state ranges from 1.95-2.47 eV. We report excitation energies as low as 1.62 eV that still produce this central eKE feature, suggesting Process (V) does not occur for lower photon energies; however, at higher photon energies it becomes unclear if autodetachment plays a role in generation of the central feature, especially since the complete mechanism for dissociation is largely uncertain. Although we are not able to say with certainty, based on our observations and speculation, the two photon process [Process (IV)] seems most likely to be the mechanism responsible for the central eKE feature.

4.5 Summary

The dissociation of the linear $OCuO^-$ isomer has been studied using both nanosecond and femtosecond laser systems, displaying the useful capabilities of both detection methods. The experiments presented in this chapter have also shown how to use source conditions for selectively isolating isomers and utilizing this to our advantage.

Monitoring the central eKE feature and Cu^- fragment signal via nanosecond pulse width timescales acquired an energy range for both features and identified the linear anion as the only isomer produced within our source conditions. Using femtosecond TRPES, identification of the time frame for complete dissociation of the linear anion into Cu^- was extracted (~150 ps). Starting from the linear anion, the only energetically reasonable one photon dissociation process ends in the $O_2 + Cu^-$ exit channel [Eq. 4.1, (III)]. The relatively long timescale to production of Cu^- in the time resolved experiment [Figure 4.6] suggests an energetic barrier to dissociation. A central eKE feature also coincides with the production of Cu^- upon dissociation; however, its origin has some uncertainty. Based on all acquired energy spectra and speculation [Figure 4.8], the two photon process [Eq. 4.2, (IV)] for production of this feature seems to be the most logical conclusion, although we still note autodetachment [Eq. 4.2, (V)] is still a possible cause for the feature at relatively higher photon energies.

The conclusions made here hopefully drive more interest for theoretical groups to study CuO_2^- in more detail. Specifically, the energy gap between the anionic linear and bent isomer [Figure 4.7, E_b] has a large experimental uncertainty, yet scarcely agrees with current theoretical methods [89,94]. Even more so, the process for dissociation is

suggested to have an energetic barrier. Plotting accurate potential surfaces can provide more insight on the dissociative mechanism.

Chapter 5

CuF^-: An Introduction to Copper Fluoride Anions

5.1 Introduction

Throughout the previous chapters, we have explored the electron scattering dynamics for small copper oxide anions. We now turn our attention to studying the effects accompanied by alterations in the anion composition, specifically the ligand atoms bound to the transition metal atom (Cu). For the remaining two chapters, the electron scattering effects for copper fluoride anions will be explored through the use of a tunable laser source, similar to the previously discussed work on CuO^- in Chapter 3.

Substitution of the O atom in CuO^- with an F atom, or any halogen, may not appear significant at first glance, but has profound differences when discussing electronic detachment from parent molecular orbitals. The molecular anion valence configurations differ in regards to one being closed shelled (CuO^-) and the other open shelled (CuF^-), and as we will see in future sections, the extra unpaired electron in the HOMO for CuF^- is largely based on the Cu atom, providing us with the ability to study the effects of detachment from molecular orbitals with large transition metal character.

To date, information on anionic and neutral CuF remains scarce. To the best of the author's knowledge, no studies on the CuF anion have been previously reported, and this chapter aims to provide not only details for copper fluoride anion generation, but also an examination of the detachment dynamics to the lowest energy neutral state. In regards to the neutral species, early microwave spectroscopic work has been previously reported [102,103], but the limits of the methods employed prevented full characterization of higher excited states of the neutral. A later gas phase chemiluminescence examination of Cu + F_2 reactions observed CuF fluorescence, allowing characterization of certain triplet excited states that strongly coupled with the singlet states through spin-orbit interaction [115]. Photoelectron spectroscopy provides the ability to characterize these triplet states with minimal selection rules, and it is our intent to view these spin-orbit states with this alternate method.

5.2 Experimental

CuF^- molecular anions were generated by flowing 50 psi of O_2 gas (99.0% purity) through a pulsed nozzle (10 Hz repetition rate) into the discharge apparatus [Section 2.1], in which the Teflon plates provided the source of fluorine in the generated plasma. A significant amount of F^- (identified by TOF-MS and an eBE = 3.40 eV) was produced and observed using this method, allowing calibration of our assignments in the mass spectrum. During operation the ion source chamber was maintained at a pressure between 6×10^{-6}-8×10^{-6} Torr. The ^{63}Cu and ^{19}F isotopic mass peaks were selectively excited due to their higher natural abundance in the mass spectrum (i.e. 82 amu CuF^-).

Photoelectron images for CuF^- were collected between photon wavelengths 305-770 nm (4.065-1.610 eV), with the exception of the range 380-430 nm. The momentum space distribution of photoelectrons was reconstructed from each collected image using the BASEX program of Dribinski et. al. [3], allowing extraction of the photoelectron spectrum and corresponding angular distributions.

5.3 Results and Analysis

5.3.1 CuF^- $X'^1\Sigma^+ \leftarrow X^2\Sigma^+$: Divergent PAD behavior for individual vibrational channels and relative vibrational cross-sectional enhancement

Figure 5.1(a,b) displays the 740 nm ($h\nu$ = 1.675 eV) photoelectron/reconstructed image with its associated energy domain spectrum, which features the vibrational band associated with transitions to vibrational levels of the neutral ground state of CuF ($X'^1\Sigma^+$). Lower binding energy peaks correspond to transitions from the anion ground vibrational level ($v''=0$) to lower vibrational levels (v') of the neutral, labeled in Figure 5.1 as $v' \leftarrow 0$. Lorentzian line shapes were fit to the spectra to determine vibronic transition energies. Extracted eBEs for each vibrational level were used to calculate the vibrational frequency, the results listed in Table 5.1. Images for analysis were selected close to the threshold energy where instrumental broadening is minimized. The adiabatic electron affinity (AEA) for the $X'^1\Sigma^+ \leftarrow X^2\Sigma^+$ transition is 1.271 eV with a vibrational frequency for the neutral of 630 cm^{-1}, comparable to Ref[102,103].

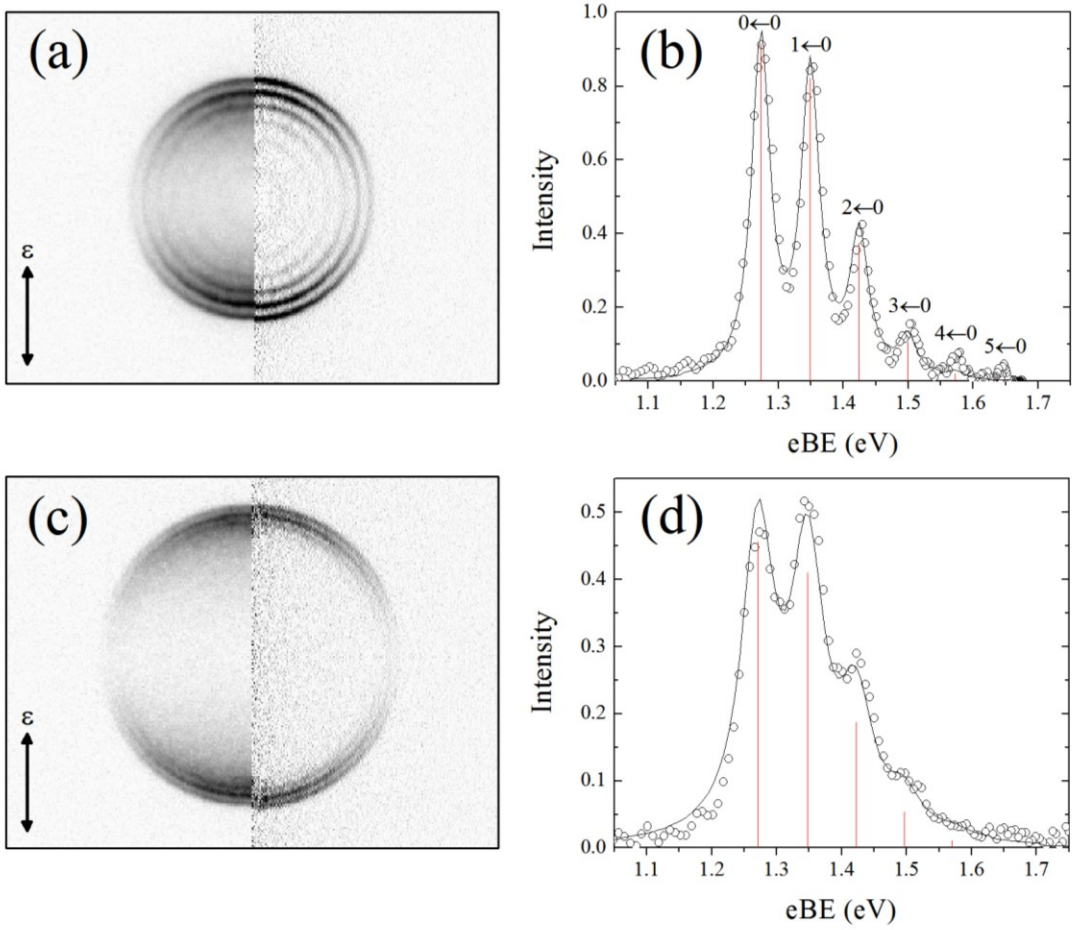

Figure 5.1: (a) Photoelectron image of CuF^- (left half) and reconstructed image (right half) taken at 740 nm ($h\nu$ = 1.675 eV). (b) Corresponding energy domain spectrum (open circles) with a FC analysis (red lines) with a 40 meV FWHM convolution (black line) added to simulate instrumental broadening. (c) CuF^- at 605 nm ($h\nu$ = 2.05 eV). (d) 605 nm energy spectrum with a FC analysis and convolution using the extracted 740 nm FC factors.

TABLE 5.1: $CuF \leftarrow CuF^-$ Experimental Data

Transition	$v' \leftarrow v''=0$	eBE (error)
$X'\,^1\Sigma^+(v') \leftarrow X^2\Sigma^+(v'')$	$v'=0$ (eV)	1.271 (0.002)
	$v'=1$ (eV)	1.350 (0.002)
	$v'=2$ (eV)	1.427 (0.004)
	$v'=3$ (eV)	1.501 (0.009)
	$v'=4$ (eV)	1.57 (0.01)
	r_e'' (Å)	1.83 (0.01)
	ν (cm^{-1})	630 (30)

A Franck-Condon (FC) analysis was performed with PESCAL [66] on the vibrational band [Figure 5.1 (red lines)] using Morse parameters, and convoluted with a Lorentzian function with a FWHM of 40 meV to simulate instrumental broadening [Figure 5.1 (solid black line)]. The Morse parameters used in the FC analysis for neutral CuF were obtained from Ref[102,103] (consistent with our measurements), and the anion bond length was optimized using PESCAL to fit to the 740 nm experimental data (r_e'' = 1.83±0.01 Å). A higher photon energy image (605 nm) and its energy domain spectrum with a FC analysis is shown in Figure 5.1(c,d). A simulation was performed using the FC factors (FCFs) [Section 1.3.3] extracted from the 740 nm analysis, but convoluted with a broader (FWHM = 70 meV) Lorentzian to account for additional instrumental broadening. The simulation gives a good fit, suggesting the FCFs extracted from the 740 nm spectrum represent a reliable control to indicate cases of non-FC behavior.

5.3.1.1 Photoelectron Angular Distributions (PADs) for Specific Vibrational Transitions

The anisotropy parameter (β) values for the energy range across the FWHM of selected $v'\leftarrow0$ (v' = 0-4) transitions were extracted by fitting with the equation: $I(\theta)=(\sigma/4\pi)[1+\beta P_2(\cos\theta)]$, [Section 1.2.1]. The PADs for each transition were monitored between photon wavelengths 770-605 nm ($h\nu$ = 1.61-2.05 eV), the lowest photon energy being the limit of our dye laser grating and the higher being limited by the inability to resolve vibrational channels at higher eKE. The results are displayed in Figure 5.2 as β (black circles) plotted against photon energy, where each β value represents the PAD at a specific photon energy. The error bars represent the standard deviation of β values acquired from multiple images taken at each photon energy.

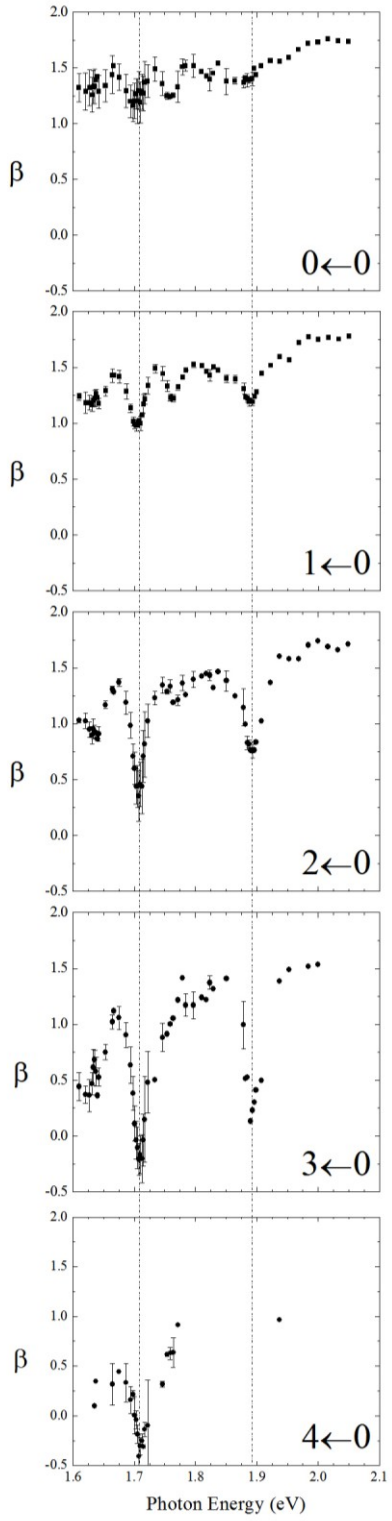

Figure 5.2: PADs as a function of photon energy for vibrational channels v'←0 (v' = 0-4), error bars shown in black. Vertical dotted lines indicate two strong anisotropy deviations for all channels at hν = 1.705 & 1.89 eV.

The 605 nm image [Figure 5.1(c)] discussed earlier is represented by the right most (highest photon energy) data point for most of the vibrational PADs in Figure 5.2 (except for the 4←0 transition), and it is clear from this image that β for all vibronic transitions is positive at this photon energy. There appears to be a general decrease in β towards lower photon energy for each vibronic transition; however, characterization of this trend is difficult as there are several large fluctuations within this energy range. It is particularly clear that for all the vibronic transitions, β sharply drops at photon energies near 1.71 eV and 1.89 eV. These sharp β deviations become more apparent for higher v′ transitions and occur for each vibronic transition at essentially the same photon energy. Figure 5.3

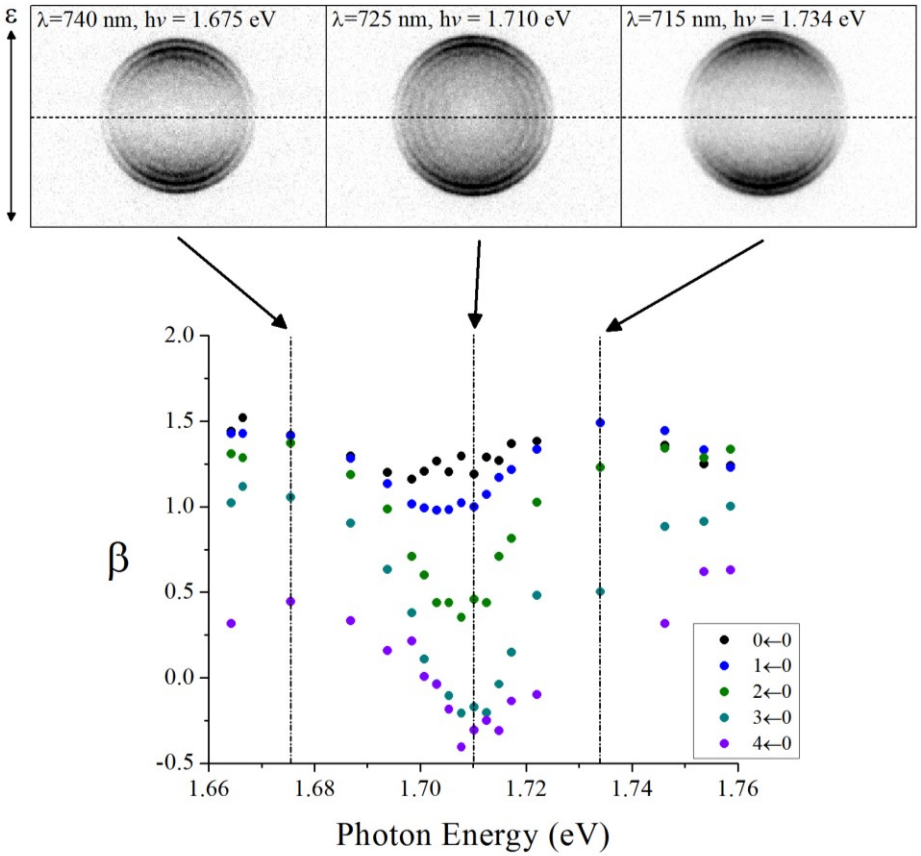

Figure 5.3: Three photoelectron images (top) that scan through the lower energy anisotropy deviation (plot below). A horizontal slice through the images (horizontal dashed line) shows more intensity in the 725 nm image, indicating a deviation towards more isotropic β values for all vibrational channels at the same photon energy.

focuses on the small energy range from 1.66-1.76 eV (the lower energy deviation). Above the plot are three selected photoelectron images (740, 725, 715 nm) at photon energies that traverse this region. The intensity distributions of the inner rings in the 725 nm image become significantly more isotropic relative to the 740 or 715 nm images. This can be observed by following the horizontal intensities across the center of these images (noted by the horizontal dotted line in Figure 5.3) and noticing the 725 nm image possesses the most intensity.

5.3.1.2 Non-adiabatic Effects in the Integrated Cross-Sections

Traversing the photon energy range in Figure 5.2, the relative vibrational channel intensities undergo significant fluctuations. The 740 nm FCFs can be used as a reference to monitor these changes. Figure 5.4 displays the intensity deviations from simulated spectra, using the 740 nm FCFs, for each channel ($v' = 1\text{-}5 \leftarrow v'' = 0$) relative to the 0←0 channel intensity. For each photon energy, a simulation was performed similar to the 605 nm spectrum [Figure 5.1(d)]. The change in resolution with eKE is approximated in the following manner. An average peak width (ΔeKE) is determined by fitting Lorentzian functions to each peak in the spectrum. The overall instrument response function is then taken as a Lorentzian with width ΔeKE. The simulations are compared with the experimental energy spectra by scaling of the 0←0 transition intensities to unity, and noting the intensity difference in subsequent peak heights between the experimental and simulated data. A positive deviation indicates the experimental transition has greater intensity than the simulated FC profile transition.

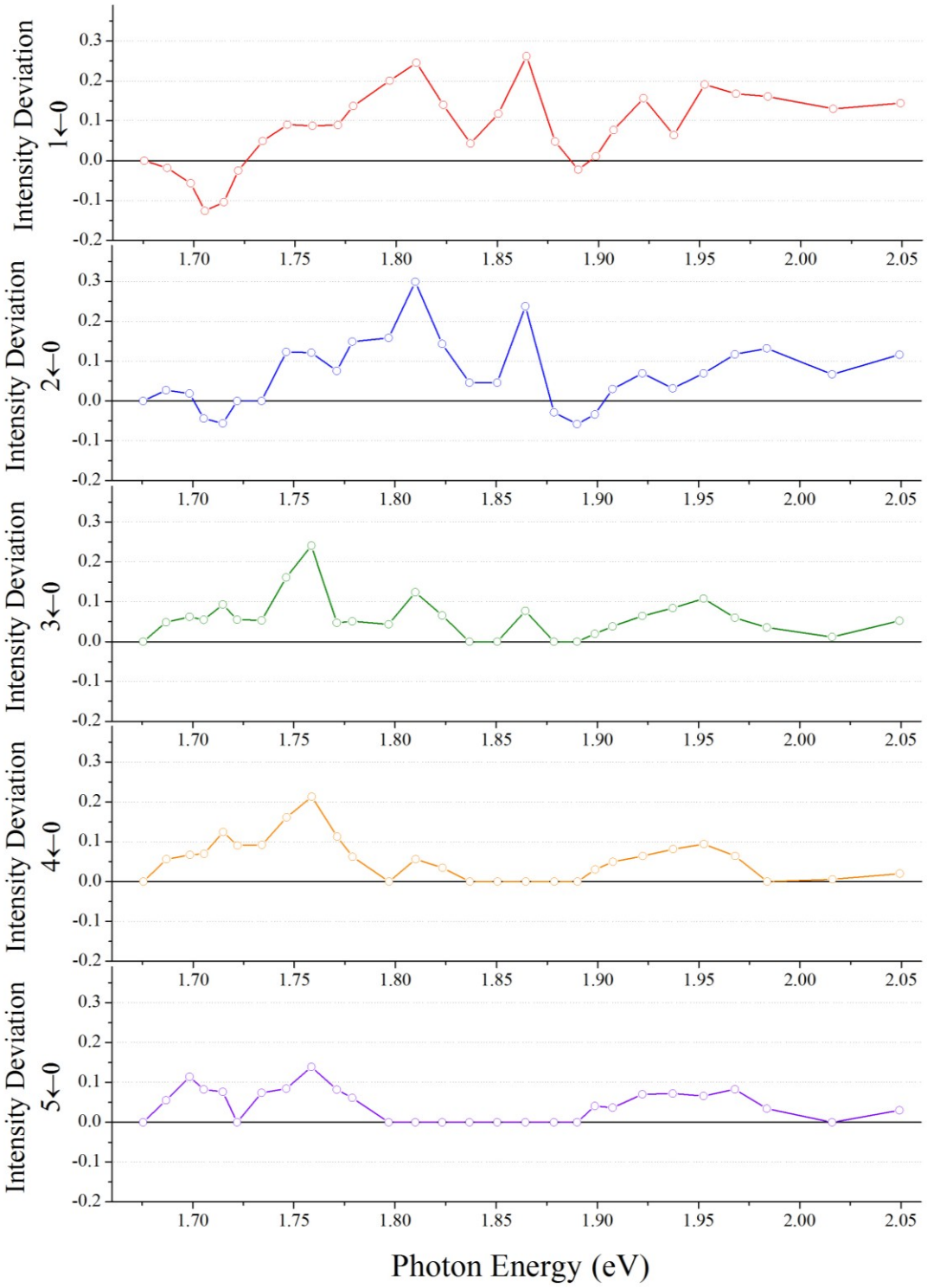

Figure 5.4: Intensity deviations for vibrational channels v'←0 (v' = 1-5) as a function of photon energy. Deviations are relative to the 740 nm FCFs; therefore, zero marks no change from the 740 nm energy spectrum.

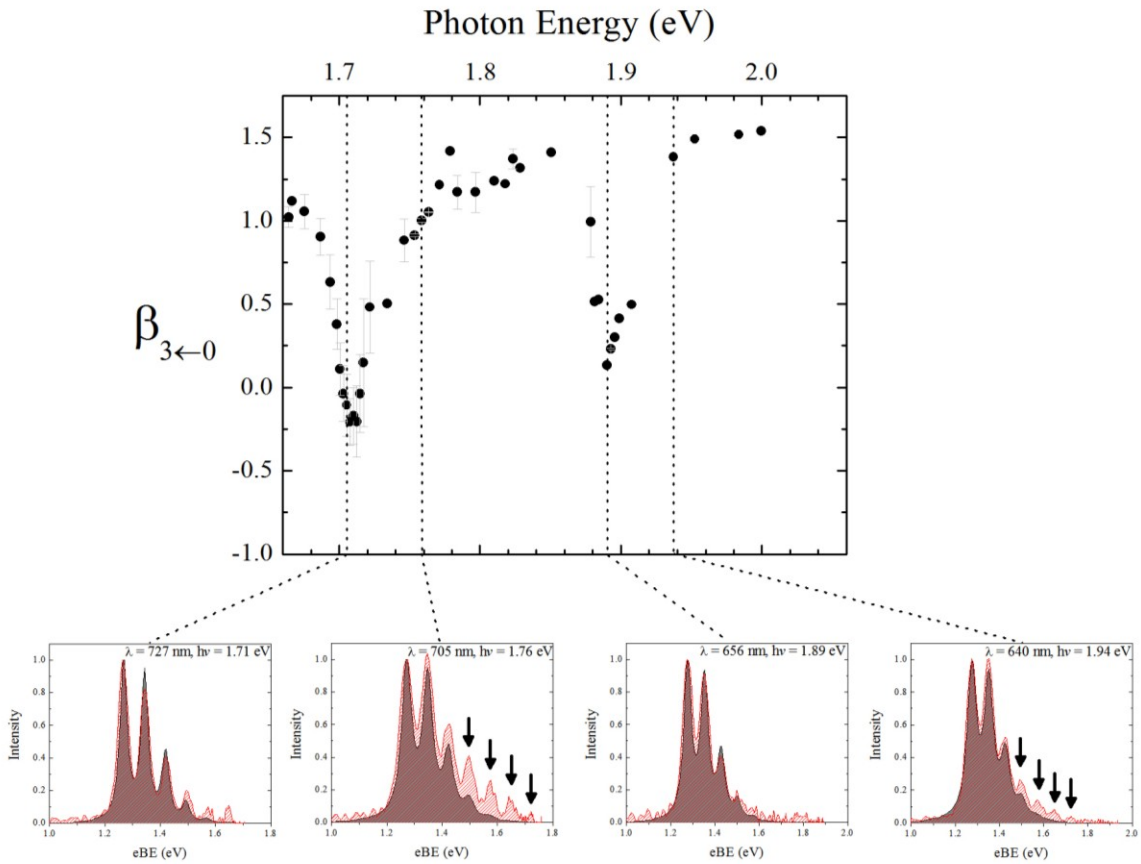

Figure 5.5: PAD for the 3←0 vibrational channel (top). Vertical lines indicate spectra at specific photon energies (bottom) showing the experimental spectra (red) overlaid with the simulated energy spectra using the 740 nm FC factors (filled gray). The two left most spectra show the same trend as the two right most spectra, both seeing a relative increase in the v'←0 (v' = 3-6) channel intensities (black arrows) just past the respective β deviations.

Figure 5.5 displays four of the simulated spectra (filled gray) overlaid with experimental spectra (red). Comparison with the 3←0 transition PAD (black circles) is shown above, with vertical dashed lines representing the energy spectrum at that specific photon energy. The spectra can be split into two pairs, the two on the left-hand side (727 & 705 nm) showing the bottom of the lower energy β deviation and slightly higher photon energy, and the two on the right-hand side (656 & 640 nm) showing the higher energy β deviation and slightly higher photon energy. It appears that the maxima in the overall cross-section deviations for channels v' = 3-6 (black arrows) occur at slightly

higher photon energies than the minima in both β deviations. Discussion of the $X'^1\Sigma^+ \leftarrow X^2\Sigma^+$ transition will be centered on the relationship between these two types of deviations.

5.3.2 CuF Excited Electronic States

Earlier work performed using microwave spectroscopy on neutral CuF reported three excited neutral electronic states ($A'^1\Sigma^+$,$B'^1\Pi$, & $C'^1\Delta$) [102,103]; however, the spin selection rule for electric dipole absorption transitions, $\Delta S = 0$, limits transitions from the ground state of CuF ($X^1\Sigma^+$) to only singlet excited states. Although some triplet states ($a'^3\Sigma^+$,$b'^3\Pi_\Omega$, & $c'^3\Delta_\Omega$) have been characterized through absorption and emission spectroscopy due to strong state mixing [106], certain triplet spin-orbit states remain to be observed. Negative ion photoelectron spectroscopy can overcome this limitation and we use this technique to probe excited states that were otherwise inaccessible in previous results.

Three photoelectron images (360, 350, & 313 nm) with their corresponding energy spectra below them are shown in Figure 5.6 (a-c). The $X'^1\Sigma^+ \leftarrow X^2\Sigma^+$ transition of the previous section [Section 5.3.1] is the outermost ring in all of the images, where the individual vibronic transitions are unresolved due to instrumental broadening (not shown in energy spectra). The higher eBE features >3 eV show prominent vibrational structure and can be distinguished into two different vibronic bands and a series of unresolved transitions. The experimental parameters for the apparent vibronic bands were extracted and summarized in Table 5.2.

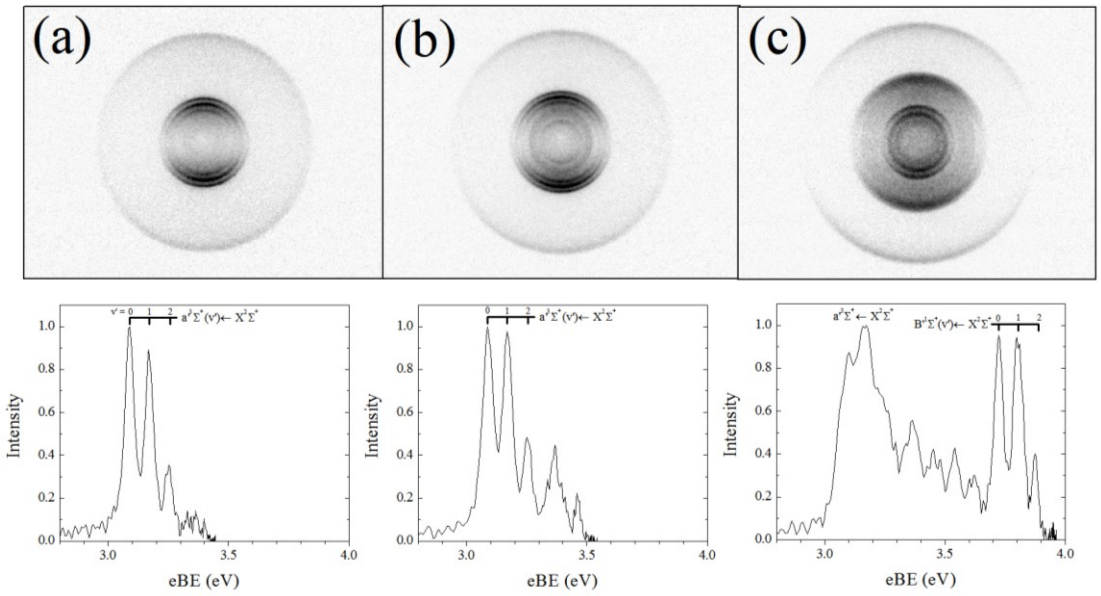

Figure 5.6: CuF^- at a) 360 nm b) 350 nm c) 313 nm (vertical laser polarization). Energy domain spectra located below respective wavelength images. The outer ring in all images is the $X'^1\Sigma^+ \leftarrow X^2\Sigma^+$ transition (not shown in energy spectra). All spectra show the transition to the first excited state $a'^3\Sigma^+ \leftarrow X^2\Sigma^+$, but it is not until higher photon energy (c) the $B'^1\Sigma^+ \leftarrow X^2\Sigma^+$ transition is observed.

TABLE 5.2: CuF Excited State Experimental Data

Transition ($CuF^* + e^- \leftarrow CuF^-$)		Value (error)
$a'^3\Sigma^+(v') \leftarrow X^2\Sigma^+(v''=0)$	$v'=0$	3.09 eV
	r_e	1.75 (0.01) Å
	ν	690 (20) cm^{-1}
$A'^1\Sigma^+(v') \leftarrow X^2\Sigma^+(v''=0)$	$v'=0$	3.72 eV
	r_e	1.74 (0.01) Å
	ν	640 (40) cm^{-1}

The lower energy band, labeled $a'^3\Sigma^+(v' = 0\text{-}2) \leftarrow X^2\Sigma^+(v''=0)$ (3.09-3.25 eV), is resolved in both the 360 and 350 nm images [Figure 5.6 (a,b)], with a measured a' state equilibrium bond length of 1.75±0.01 Å and vibrational frequency of 690 cm^{-1}. The higher energy band, labeled $A'^1\Sigma^+(v' = 0\text{-}2) \leftarrow X^2\Sigma^+(v''=0)$ (3.72-3.88 eV), only seen in the

313 nm image, has a measured A' state equilibrium bond length of 1.74±0.01 Å and vibrational frequency of 640 cm^{-1}. Both the a′ and A′ bands show remarkably similar FC profiles indicating similar equilibrium bond lengths for the different neutral states, given that the vibrational frequencies are comparable. Their positive β(eKE) values [a′(v′=0) β(0.36 eV)=+1.7; B′(v′=0) β(0.24 eV)=+1.5)] suggest large contribution from photoelectron p-waves, indicative of a strong s component to the orbital. The a' and A' bands are assigned the term symbols $^3\Sigma^+$ and $^1\Sigma^+$ respectively, based on previous neutral analyses in Ref[102,103,106]. The overlapping series of transitions beginning at an eBE = 3.37 eV cannot be assigned due to instrumental broadening; however, we suggest the presence of multiple spin-orbit states based on the reported electronic state $^3\Pi$ (ν = 649 cm^{-1}) [105-107], corresponding to an eBE = 3.45 eV in our energy spectra.

5.4 Discussion

5.4.1 CuF $X'^1\Sigma^+ \leftarrow X^2\Sigma^+$ PAD and Vibrational Channel Intensity Fluctuations

Deviations in cluster anion PADs have been previously reported by our laboratory [73,110,111]. Specifically, monitoring the neutral ground state PAD for I^- clusters shows a spike in β near the energetic threshold of the higher neutral spin-orbit state, deviating from the Cooper-Zare equation. It was shown that these β deviations were caused by electronic photoexcitation into a resonant dipole bound state (DBS), temporarily capturing the electron prior to detachment. The deviation in β arises from interference of two pathways, (1) direct detachment and (2) excitation to the DBS followed by autodetachment into the continuum, also known as a Feshbach resonance, with both

pathways ejecting the electron with the same eKE. The PADs shown in Figure 5.2 display similar behavior at multiple photon energies, however, the possibility of accessing a DBS can be ruled out. For neutrals possessing a dipole moment >2 D, such as CuF (μ = 5.26 D) [112], a DBS is predicted to lie energetically below the ground state neutral and this DBS will also have associated vibrational levels just below the neutral vibrational levels, as seen in Chapter 3 for CuO. The photon energy range in this region could energetically access the DBS levels below the $X'^1\Sigma^+(v'>5)$ levels, but would have extremely unfavorable FC overlap ($\approx$ 0) with the ground vibrational level of the anion ground state, prohibiting excitation to these DBSs. Nevertheless, the deviations in the vibrational channel PADs [Figure 5.2] are narrow, and sharp changes in the differential cross sections for photodetachment are generally indicative of the existence of temporary excited states. To evaluate this assertion we perform density functional theory (DFT) and time-dependent density functional theory (TDDFT) calculations to optimize the anion/neutral ground states and obtain excitation energies of the lowest lying excited anion electronic states. Specific computational details can be found in a later section [Section 5.4.1.1]. The results are listed in Table 5.3:

TABLE 5.3: DFT/TDDFT Computational Data

Electronic State	r_e (Å)	ν (cm^{-1})	Energy (eV)[c]
$CuF^- X^2\Sigma^+$	1.88	439	0
$CuF\ X'^1\Sigma^+$	1.78	584	1.32
$[CuF^-]^* A^2\Sigma^+$	–	–	1.64
$[CuF^-]^* B^2\Pi$	–	–	1.805
Experimental $X^2\Sigma^+$	1.83(0.01) [a]	–	0
Experimental $X'^1\Sigma^+$	1.745 [b]	623[b]	1.271(0.002) [a]

[a]This work (based on 740 nm spectrum)
[b]Ref[102,103]
[c]Referenced to anion ground state ($X^2\Sigma^+$)

An orbital energy diagram for CuF^- is also provided in Figure 5.7 for visualization of the anion ground state electronic configuration ($X^2\Sigma^+$). The ordering of the molecular orbitals (MOs) was based on a Mulliken population analysis performed with the same method and basis sets as the optimizations.

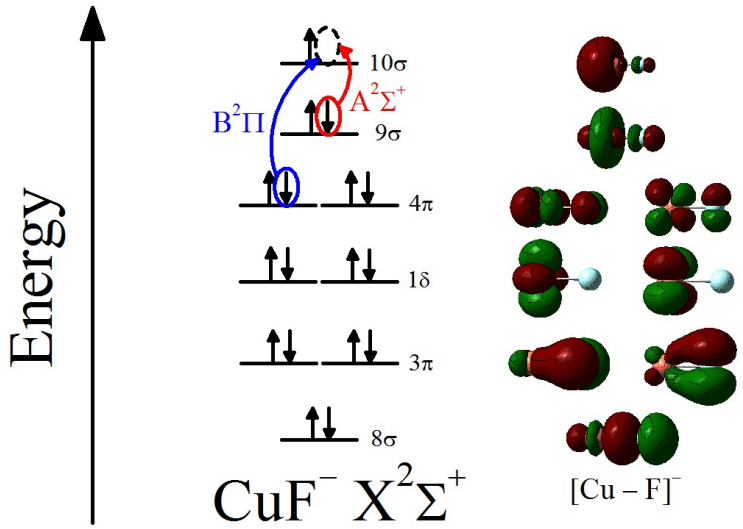

Figure 5.7: Molecular orbital (MO) diagram for CuF^- ground state anion ($X^2\Sigma^+$). Excitation of an electron from the 9σ (red) or 4π (blue) orbital leads to the excited state configurations $A^2\Sigma^+$ or $B^2\Pi$, respectively. Visual MOs provided to the right of diagram.

Also shown in the diagram are the anion excited state configurations upon promotion of an electron from 9σ→10σ, state $A^2\Sigma^+$ (red), and 4π→10σ, state $B^2\Pi$ (blue). The TDDFT calculation suggests these two states are located 1.64 eV and 1.805 eV above the ground state anion, respectively. Given the error in TDDFT calculations is typically on the order of ±0.1-0.3 eV [109], transitions to both of these excited states lie well within the energetic range of the two largest β deviations (1.705 eV and 1.89 eV), suggesting the deviations are caused by an electronic Feshbach resonance at the vertical excitation of these excited anion states. To schematically demonstrate such resonances, the possible excitation pathways via one photon absorption are expressed in Equation 5.1:

$$
\begin{aligned}
CuF^-(X^2\Sigma^+) &\xrightarrow{h\nu} CuF(X'^1\Sigma^+) + e^- && \text{(I)} \\
&\xrightarrow{h\nu} [CuF^-]^*(A^2\Sigma^+) \longrightarrow CuF(X'^1\Sigma^+) + e^- && \text{(II)} \\
&\xrightarrow{h\nu} [CuF^-]^*(B^2\Pi) \longrightarrow CuF(X'^1\Sigma^+) + e^- && \text{(III)}
\end{aligned} \qquad (5.1)
$$

Pathway (I) represents direct detachment from the ground state of the neutral ($X'^1\Sigma^+$), while pathways (II) and (III) represent excitation of two Feshbach resonances. A temporary anion state (respectively $A^2\Sigma^+$ and $B^2\Pi$) is initially excited and then relaxes to the neutral ground state (via electron loss and electronic rearrangement). With sufficient photon energy, all three pathways would eject the extra electron at the same eKE for each vibrational channel, meaning the pathways are indistinguishable with respect to detection of eKEs. Instead, there are two indicators one can use to distinguish pathways (II) and (III) from (I), changes in the PADs and/or changes in the integral cross sections; however, changes in the PAD are more sensitive for detection of such resonances. The PADs for all vibrational channels associated with detachment from $X'^1\Sigma^+$ [Figure 5.2] show strong deviations at 1.705 and 1.89 eV. Let us entertain the idea that these deviations can be attributed to resonances with an excited anion state [pathways (II) and (III)], prior to electron detachment. To gain more insight on accessing these excited anion states, we turn to energy calculations along the reaction coordinate (Cu−F internuclear separation).

Potential energy curves were generated, shown in Figure 5.8, for the ground state anion (black) and neutral (gray) species, and the first two anion excited states (red, blue) at MP2 level of theory. Multiple single point energy calculations were performed at different points along the internuclear coordinate. A Morse potential curve was fit to this data, from which the equilibrium bond length, vibrational frequency, anharmonic constant, and dissociation energy were extracted for each state. From these parameters

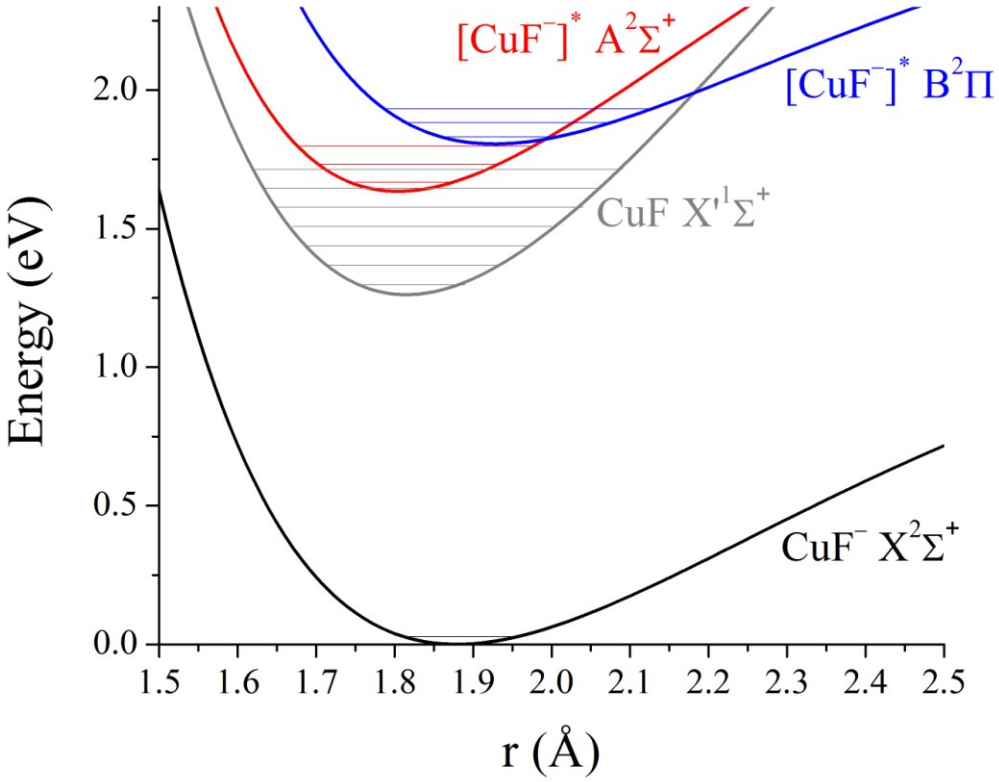

Figure 5.8: Calculated potential energy curves, using MP2 level of theory, for the ground state anion (black), ground state neutral (gray), first excited anion state (red), and second excited anion state (blue). v" = 0 vibrational level indicated by black horizontal line for the anion ground state.

vibrational levels for each state were estimated using the Morse approximation, and the low vibrational levels are shown for each curve in Figure 5.8. One immediately notices both excited anion states are energetically stable with respect to dissociation, but lie higher in energy than the neutral ground state, indicating these states are unstable with respect to electron loss. Absorption to these states could potentially support an excited anion configuration for relatively long lifetimes (τ) compared to direct detachment ($\tau_{(II)}$, $\tau_{(III)} > \tau_{(I)}$). Relaxation to the neutral ground state (via loss of the excess electron) can only be achieved from the photoexcited anion states [pathways (I) & (II)] if a rearrangement of the neutral electron configuration accompanies electron loss.

The anisotropy deviations and variations in the vibrational channel intensities might be explained by indirect detachment via these temporary excited anion state resonances. Absorption and detachment FCFs can be extracted for each excited state and neutral ground state from the Morse potentials in Figure 5.8. The results are summarized in Table 5.4:

TABLE 5.4: Calculated FCFs from MP2 Computational Data

v'	$A^2\Sigma^+ \leftarrow X^2\Sigma^+$ ($9\sigma \rightarrow 10\sigma$)	$B^2\Pi \leftarrow X^2\Sigma^+$ ($4\pi \rightarrow 10\sigma$)	$X'^1\Sigma^+ \leftarrow X^2\Sigma^+$	$X'^1\Sigma^+ \leftarrow X^2\Sigma^+$ Experimental*
0	0.55	0.80	0.61	0.41
1	0.35	0.17	0.29	0.37
2	0.092	0.030	0.081	0.17
3	0.013	0.0056	0.017	0.048
4	9.9×10^{-4}	0.0011	0.0030	0.0090
5	4.1×10^{-5}	2.6×10^{-4}	4.4×10^{-4}	0.0011
6	8.4×10^{-7}	6.2×10^{-5}	5.7×10^{-5}	N/A

*This work, based on extracted 740 nm FCFs

Comparing the calculated and experimental 740 nm neutral ground state ($X'^1\Sigma^+$) FCFs, the calculated values deviate slightly but are still able to provide general trends in the data. The calculated values reproduce the trend in the FCFs for direct detachment to vibrational levels, v'=0 > v'=1 > v'=2, of the X' state. For absorption to the anion A and B states, excitation is mainly to the v' = 0, 1 vibrational levels, suggesting these states are initially prepared upon accessing the resonances.

Excitation to the $A^2\Sigma^+$ or $B^2\Pi$ excited states will manifest in the PAD. A sharp change in the β value occurs because of interference between the competing pathways, (II) or (III) and (I). This is clearly observed at photon energies 1.705 and 1.89 eV [Figure 5.2]. Traversing through the photon energies in Figure 5.2 we see the $A^2\Sigma^+$(v'=0) state becomes energetically accessible at 1.705 eV and the $B^2\Pi$(v'=0) state at 1.89 eV. In

support of this interpretation we note good correlation between calculations of the state energies and anisotropy deviations, bringing validity to these assignments.

In regards to vibrational channel intensities, this detachment scheme becomes more complex. If the initially prepared state has a high probability of sampling the internuclear coordinate at bond lengths comparable to the neutral ground state v' = 3, 4, or 5 turning points, the chance for autodetaching to those levels is enhanced, raising the intensities of those vibrational channels relative to other neutral ground state v' levels. This is particularly noticeable in the 705 and 640 nm spectra [Figure 5.5], which show relative enhancement of the v' = 3-6 intensities just past the two significant β deviations. This probably reflects the importance of the v=1 levels for both excited anion states, which are able to sample a longer section of the reaction coordinate in comparison to the v'=0 level.

As an example, we calculate the FCFs for the overlap between the $B^2\Pi(v=1)$ and $X'^1\Sigma^+(v')$ Morse wavefunctions. The values are listed in Table 5.5:

TABLE 5.5: Calculated FCFs from MP2 Computational Data

v'	$B^2\Pi(v=1) \rightarrow X'^1\Sigma^+(v')$
0	0.316
1	0.051
2	0.046
3	**0.197**
4	**0.208**
5	**0.126**
6	0.055

Comparing to the FCFs calculated for direct detachment in Table 5.4, the v' = 3-5 level values (bold) are greatly enhanced. Near the $B^2\Pi(v=1)$ Feshbach resonance, pathway (III) starts to interfere with direct detachment [pathway (I)], and the FCFs of pathway

(III) start to dominate the FC profile. This causes a deviation in vibrational intensities relative to the direct detachment FC profile. Experimentally, this example transition is most likely to correspond to the 640 nm excitation [Figure 5.5], in which we see a noticeable enhancement of the v' = 3-6 channels.

Although this example works well in describing the $B^2\Pi$ excited state relaxation according to calculations, we note it does not work quite as well for the $A^2\Sigma^+$ excited state. The calculated FCFs for the overlap between the $A^2\Sigma^+(v=1)$ and $X'^1\Sigma^+(v')$ Morse wavefunctions are shown in Table 5.6:

TABLE 5.6: Calculated FCFs from MP2 Computational Data

v'	$A^2\Sigma^+(v=1) \rightarrow X'^1\Sigma^+(v')$
0	0.00894
1	**0.978**
2	0.00770
3	0.00524
4	7.61×10^{-5}
5	1.36×10^{-5}
6	3.52×10^{-8}

According to the calculated curves shown in Figure 5.8, the separation between the $A^2\Sigma^+$ and $X'^1\Sigma^+$ equilibrium bond lengths is only 0.01 Å (for comparision, Δr_e for $B^2\Pi$ and $X'^1\Sigma^+$ states is 0.11 Å), resulting in significant overlap of both A(v=1) and X'(v'=1) vibrational wavefunctions. Hence, the FCF associated with this transition [Table 5.6 (bold)] will be dominant over the other vibrational channels, not allowing the temporary resonance to sample the turning points of the neutral v' = 3-6 levels. Noticing the large enhancement of the v' = 3-6 levels for the 705 nm spectrum [Figure 5.5], the calculated FCFs for pathway (II) could not account for such deviation. It is reasonable to assume

that higher level of theory is required in order to accurately describe these potential energy curves, but there is also the possibility that the curve crossing between the A and B anion excited states [Figure 5.8 (red and blue diabats, r = 2.0 Å)] could account for these enhanced features. The calculated vibrational levels for $A^2\Sigma^+$(v=0-2) show that the curve crossing with $B^2\Pi$ becomes nearly energetically accessible with excitation to the $A^2\Sigma^+$(v=2) level. Depending on slight differences between our calculated curves and other levels of theory, the higher vibrational level enhancements seen in the 705 nm spectrum could be accounted for as observing the effects of accessing the curve crossing between the $A^2\Sigma^+$(v=1) and $B^2\Pi$ states, allowing the $A^2\Sigma^+$(v=1) level to sample the internuclear turning points of the neutral v' = 3-5 levels. This resonance would subsequently undergo autodetachment, raising the intensities of these vibrational channels relative to other neutral ground state v' levels.

Despite these speculations and as a final note, it is important to point out that the general scheme of exciting to a Feshbach resonance followed by relaxation (detachment/electronic rearrangement) to the neutral ground state qualitatively explains the effects observed in the PAD and relative vibrational intensities. From a quantitative standpoint, it has been shown that separations in the equilibrium bond lengths for all electronic states is considerably important for describing the vibrational intensity deviations in the energy spectra near the Feshbach resonances. Higher level of theoretical calculations for generation of more accurate potential energy curves could quantitatively improve this detachment scheme presented in this work.

5.4.1.1 Computational Details

Calculations were performed on both the anion and neutral ground states and the first two excited states of the anion species. The information obtained was previously summarized in Table 3.3. All calculations were carried out with DFT, TDDFT, or MP2 level of theory using Gaussian03 software [76] or Q-CHEM [108]. The basis sets used for all calculations were cc-pTVZ coupled with the CRENBL pseudopotential, obtained from the EMSL basis set exchange [104], for the Cu atom and 6-311+G(d) for the F atom.

Each ground state structure was optimized using the DFT method with the B3LYP functional and frequencies for the stretching mode, bond lengths, and energies were obtained. A full TDDFT calculation was performed on the optimized ground state anion using the Random Phase Approximaton (RPA) feature, with Q-CHEM, to obtain vertical excitation energies for the two lowest anion excited states [Table 3.3, Energy($A^2\Sigma^+$, $B^2\Pi$)].

The potential energy curves for the ground states of the anion/neutral and first/second anion excited states were calculated at the MP2 level of theory. An unrestricted single point energy calculation was performed on the anion ground state at each specified bond length along the potential internuclear coordinate prior to excitation and convergence on the excited state. The excited anion states were calculated by placing the 9σ or 4π beta electron into the empty 10σ orbital [Figure 3.12], and the maximum overlap method (MOM) algorithm was used to slowly converge on the excited state.

5.4.2 CuF Excited State Spectral Assignments

Many of the neutral excited states accessed by the detachment transitions of Figure 5.6 have been previously prepared and theoretically studied [105-107,113-115]. The energetic ordering of the excited states for the neutral are reported as follows: $a'^3\Sigma^+ < b'^3\Pi < A'^1\Sigma^+ < B'^1\Pi < c'^3\Delta < C'^1\Delta$. The highest photon energy employed by our experiments ($h\nu$ = 4.00 eV) can access all but the delta states, corresponding to detachment from a non-bonding delta orbital (1δ) [Figure 5.7]. Starting with the 360 nm image/spectrum [Figure 5.6(a)], the most apparent feature is the vibrational progression for the transition to $a'^3\Sigma^+$ (AEA = 3.08 eV), representing detachment from the 9σ orbital [Figure 5.7]. The angular distributions at this wavelength are shown to be largely parallel to the laser polarization axis (i.e. positive β values) for all vibrational channels v'=0-2. This is expected for detachment from σ-like orbitals as they are known to possess large s orbital character, responsible for the parallel PAD. Increasing the photon energy to 313 nm [Figure 5.6(c)], we see another vibrational progression (AEA = 3.72 eV) with an intensity distribution very similar to the $a'^3\Sigma^+ \leftarrow X^2\Sigma^+$ FC profile. This similarity can be ascribed to detachment from the same parent orbital (9σ), therefore this vibrational progression is assigned as transitions to the $A'^1\Sigma^+$ excited state [102,103]. However, it is worth noting the angular distributions for the vibrational features are somewhat different. For vibrational transitions to $a'^3\Sigma^+(v')$, $\beta_{v'}$(eKE) values follow β_0(0.36 eV)= +1.67, β_1(0.27 eV)= +1.60, and β_2(0.19 eV)= +1.46, but the vibrational transitions to $A'^1\Sigma^+(v')$ are β_0(0.24 eV)= +1.19, β_1(0.16 eV)= +0.39, and β_2(0.09 eV)= −0.05. While the β values are not reported at the same eKE, it is notable that the β_1 and β_2 values are significantly more

isotropic in the $A'^1\Sigma^+$ progression. Strong dissimilarities in β_1 and β_2 may be explained by overlap with transitions to the $^1\Pi$ state [102,103], corresponding to an eBE of 3.78 eV. These transitions represent detachment from the 4π orbital. Detachment from the π-orbitals are expected to show perpendicular PADs (i.e. negative β values) at low eKE values, as demonstrated in the previous chapter on CuO^-. When overlapped with a parallel angular distribution, a more isotropic β value results through averaging over the two transitions.

By process of elimination, the triplet state must represent all unassigned transitions observed between $a'^3\Sigma^+$ and $A'^1\Sigma^+$ (eBE = 3.30 – 3.71 eV). The $b'^3\Pi$ state has been previously reported to lie 2.174 eV above the neutral ground state [112], corresponding to 3.444 eV above the anion ground state; however, we note only this value is reported for the $\Omega = 1$ spin-orbit state. Absorption/fluorescence studies have been able to characterize the $b'^3\Pi_1$ state due to its strong spin-orbit coupling with the $B'^1\Pi$ state, and likewise the $b'^3\Pi_{0+}$ was studied through coupling with the $A'^1\Sigma^+$ state. We note the $b'^3\Pi_2$ spin-orbit state has yet to be reported. This could be due to little to zero spin-orbit mixing, as it would require mixing with the $c'^3\Delta$ state, from which the energy gap would be too large, making spin-orbit coupling unfavorable. Our 350 nm image/spectrum [Figure 5.6(b)] shows two transitions near the center of the image, possessing eBEs at 3.37 and 3.45 eV, the latter being the $b'^3\Pi_1 \leftarrow X^2\Sigma^+$ transition. Due to Hund's rule, the $b'^3\Pi_2$ state must lie lower in energy than $b'^3\Pi_1$ corresponding to a lower eBE; hence, the peak at eBE = 3.37 eV would fit well with the assignment to the $b'^3\Pi_2 \leftarrow X^2\Sigma^+$ transition, as it clearly is not part of the $a'^3\Sigma^+$ vibrational progression. At higher photon energy [Figure 5.6(c)], higher eBE peaks are noticeable at 3.54 and 3.62 eV. Although we cannot say with certainty

because of instrumental broadening, these peaks likely belong to $b'^3\Pi_{0+,\,0-}$ states and/or higher vibrational levels of the $b'^3\Pi_{1,\,2}(v')\leftarrow X^2\Sigma^+(v''=0)$ progression.

5.5 Summary

The first experimental evidence of the CuF anion has been presented in the preceding sections. Excitation from the ground state of the anion at certain photon energies was found to access electronic Feshbach resonances, associated with accessing two anion excited states ($A^2\Sigma^+$ and $B^2\Pi$) lying above the neutral ground state (X'). The effects upon accessing such resonances were observed as fluctuations in vibrational channel PADs and relative vibrational channel intensities from detachment from the neutral ground state. The effects in the PADs were attributed to two competing pathways [Eq. 5.1], direct detachment (I) and autodetachment from temporary excited anion states, (II) and (III). Calculations were performed to generate diabats for anion and neutral states [Figure 5.8], from which FCFs could be extracted to quantitatively demonstrate the relative vibrational intensity enhancements seen in certain energy spectra [Figure 5.5]. Although this approach seems to work well in describing the higher energy resonance ($B^2\Pi$), the other proved to be a poor fit ($A^2\Sigma^+$), indicating either the need for higher level of theory for describing the diabats or that the effects from potential curve crossings are being observed.

In addition to ground state neutral detachment features, a series of higher photon energy photoelectron spectra were reported [Figure 5.6], displaying the first four excited neutral states for CuF ($a'^3\Sigma^+$, $b'^3\Pi$, $A'^1\Sigma^+$, and $B'^1\Pi$) within a small energy range. The $a'^3\Sigma^+$ & $A'^1\Sigma^+$ states and $b'^3\Pi$ & $B'^1\Pi$ states represent detachment from the same parent

orbitals, respectively 9σ and 4π [Figure 5.7]. The previously unreported $b'^3\Pi_2$ spin-orbit state was assigned to the transition at eBE = 3.37 eV based on suspected low spin-orbit mixing with the higher energy $c'^3\Delta$ state, attributing to its absence in past absorption/fluorescence studies.

As previously noted, the copper fluoride molecular anions have not been experimentally studied in the literature. With the dynamics we have already explored with CuF^-, it becomes interesting to study the effects of higher number of ligands surrounding the metal atom. As we will see in the next chapter, addition of one F ligand to CuF^- alters the electron binding properties significantly, opening a new class of molecular anions termed "superhalogens".

Chapter 6

CuF_2^-: A Study of Orbital Arrangements and Superhalogen Properties

6.1 Introduction

The halogens are some of the most electronegative elements in the periodic table, largely attributable to the single electron hole in the valence p-shell. Chlorine possesses the highest recorded atomic electron affinity (EA) at 3.61 eV. Upon attachment of an electron to a neutral halogen atom, we see that the excess electron experiences a high effective nuclear charge (within the Hartree-Fock approximation), binding the electron relatively close to the nucleus. This lowers the total energy of the anion far below the total energy of the corresponding neutral atom.

Early work synthesizing the $XePtF_6$ salt [116] showed that negatively charged metal halides were capable of possessing EAs large enough to ionize Xe. PtF_6^- was predicted to have a minimum EA of 7.37 eV, vastly exceeding the EA of atomic Cl, which eventually lead to classification of such metal-halogen anions as "superhalogens" [117]. The term superhalogen broadly refers to molecules or clusters possessing relatively high EAs, comparable or exceeding atomic Cl. These are thought to follow the formula

$MX_{(n+1)/m}$, where n is the maximal formal valence of metal atom M, and m is the normal valence of ligand X. A number of superhalogens have already been theoretically and experimentally studied [118,122,125,129,140], as has their ability to bond to noble gases and other atoms/molecules [119-121]. Specifically, studies of copper based molecular anions such as CuX_n^- (X = Cl, Br) have been previously reported in the literature [122], where superhalogen properties are not observed until $n \geq 2$. As mentioned in the previous chapter on CuF^-, no experimental work has been previously reported on copper fluoride anions to the best of the author's knowledge. This chapter aims to provide information on CuF_2^-, as well as an analysis of its corresponding neutral electronic states.

An extensive collection of theoretical work has been accumulated for the neutral species [32,123,125,129-132]; however, very few experiments have been conducted [123,133]. Along with the aid of recent theoretical work [32,124,125,129], this chapter will explore the PADs for detachment near threshold, the possibility of emerging superhalogen characteristics upon the addition of one fluorine atom to CuF^-, and present a comparison with other previously reported Cu-halogen molecular anions [122].

6.2 Experimental

CuF_2^- molecular anions were generated by flowing 50 psi of O_2 gas (99.0% purity) through a pulsed nozzle (10 Hz repetition rate) into the discharge apparatus [Section 2.1], in which the Teflon plates provided the source of fluorine in the generated plasma. A significant amount of F^- (identified by TOF-MS and an eBE = 3.40 eV) was produced and observed using this method, allowing calibration of our assignments in the mass spectrum. During operation the ion source chamber was maintained at a pressure

between 6×10^{-6}-8×10^{-6} Torr. The ^{63}Cu and ^{19}F isotopic mass peaks were selectively excited due to their higher natural abundance in the mass spectrum (i.e. 101 amu CuF_2^-).

Photoelectron images were collected between photon wavelengths 280-354 nm (4.428-3.502 eV). The momentum space distribution of photoelectrons was reconstructed from each collected image using the BASEX program of Dribinski et. al. [3], allowing extraction of the photoelectron spectrum and corresponding angular distributions.

6.3 Results and Analysis

6.3.1 High eKE and Near Threshold Spectra

Figure 6.1(a) shows the first photoelectron image of CuF_2^- with its reconstructed image for photon wavelength 310 nm ($h\nu$ = 4.00 eV). A FC analysis [Figure 6.1(b) (red lines)] was performed using Chen's method [128], which is based on the Sharp and Rosenstock formula [126] taking into account treatment of the Duschinsky effect [127].

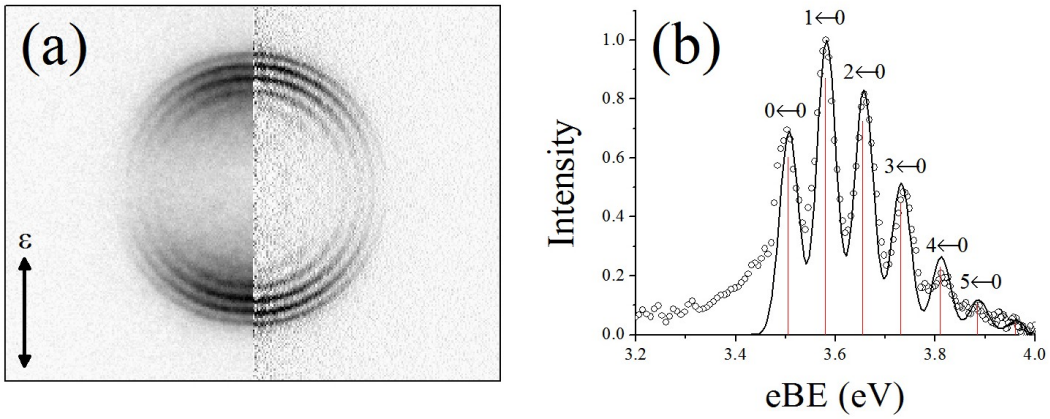

Figure 6.1: (a) Photoelectron image of CuF_2^- (left half) and reconstructed image (right half) taken at 310 nm ($h\nu$ = 4.00 eV). (b) Corresponding energy domain spectrum (open circles) with a FC analysis (red lines) with a 40 meV FWHM convolution (black line) added to simulate instrumental broadening.

Parameters for the calculation were obtained from the output of DFT calculations (B3LYP method/Cu[MDF10 basis set with MDF10 pseudopotential]/F[aug-cc-pVTZ basis set]) performed by the Gaussian03 program [76]. The AEA was taken directly from our experimental data. The energy spectrum shows a vibrational band with an AEA = 3.50 eV with the vibrational transitions labeled above their respective peaks as v′←v″. The vibrational frequency (ν) associated with the harmonic oscillator frequency of this band was measured to be 630±30 cm^{-1}. The calculated FCFs were convoluted with a 45 meV Lorentzian to simulate instrumental broadening and the simulation of the X'(v')←X(v" = 0) band [Figure 6.1(b) (black solid line)] is compared with the experimental spectrum [Figure 6.1(b) (open circles)]. A long tail of electrons is apparent at lower binding energies which may be due to hot bands and/or overlap with other copper molecular anions in the mass spectrum. To examine this region in more detail, the photon energy was reduced to 3.54 eV, shown in Figure 6.2 (black line), where the lower eBE peaks are more resolved. Alterations in the backing pressure at this wavelength shows intensity deviations in the peaks located at eBE = 3.38 & 3.44 eV relative to the 0←0 peak. Through these observations we designate both peaks to be hot bands (HBs). Features at eBE < 3.38 eV resemble those of another anion in the mass spectrum. Two atomic mass units (amu) lighter than $^{63}CuF_2^-$ (mass = 101 amu) lies $F^{63}CuOH^-$ (mass = 99 amu), and its energy domain spectrum is shown in Figure 6.2 (red line) overlaid with the experimental $^{63}CuF_2^-$ spectrum at the same wavelength (350 nm) using the same source conditions. Both spectra show strikingly similar characteristics near lower binding energies. This resemblance is due the isotopic anion $F^{65}CuOH^-$ also appearing in our mass spectrum, isobaric with $^{63}CuF_2^-$ (101 amu). Since the detachment

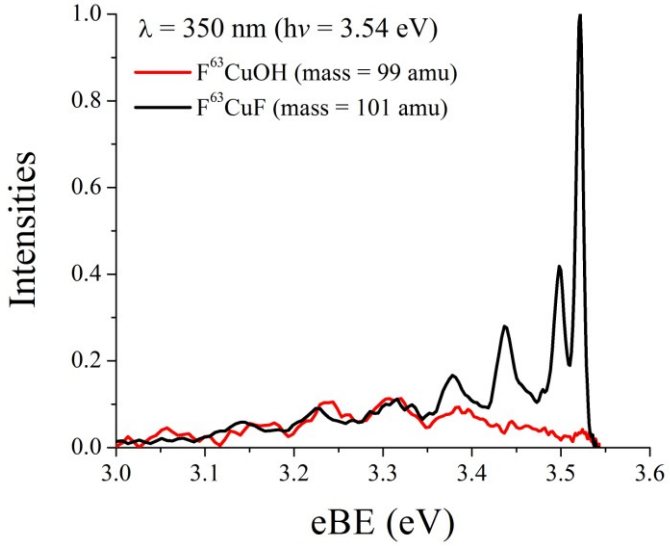

Figure 6.2: Two energy domain spectra at the same photon energy (3.54 eV) showing the photoelectron signal from $F^{63}CuOH$ (red) overlapped with the $^{63}CuF_2$ (black) signal. $F^{63}CuOH$ was used to simulate the $F^{65}CuOH$ energy spectrum because of its equivalent mass with $^{63}CuF_2$. This accounts for extra transition peaks in the $^{63}CuF_2$ spectrum.

from the ^{65}Cu isotope of $F^{65}CuOH^-$ yields almost the same photoelectron spectrum as the ^{63}Cu isotope (using our instrument), the plot demonstrates the broad electronic tail at lower eBE is clearly the result of detachment from the $F^{65}CuOH$ anion species.

A noticeable feature in the 350 nm spectrum [Figure 6.2 (black line)], that has not been addressed, is the high intensity peak located at an eBE = 3.52 eV, which is not evident in our higher photon energy spectra. Figure 6.3 (a-c) displays three energy spectra increasing in photon energy (350, 342, 334 nm), showing that the intensity of this peak (labeled $x_0 \leftarrow 0$) falls significantly, relative to the $0 \leftarrow 0$ peak, until it becomes indiscernible at higher photon energies. Likewise, two additional peaks sharply rise in intensity [Figure 6.3 (b & c), labeled $x_1 \leftarrow 0$ & $x_2 \leftarrow 0$ respectively] before also becoming indiscernible at higher photon energies. It is unclear if these $x_0, x_1, x_2 \leftarrow 0$ features are only accessible during these short energy regions or if they simply have a low absorption cross

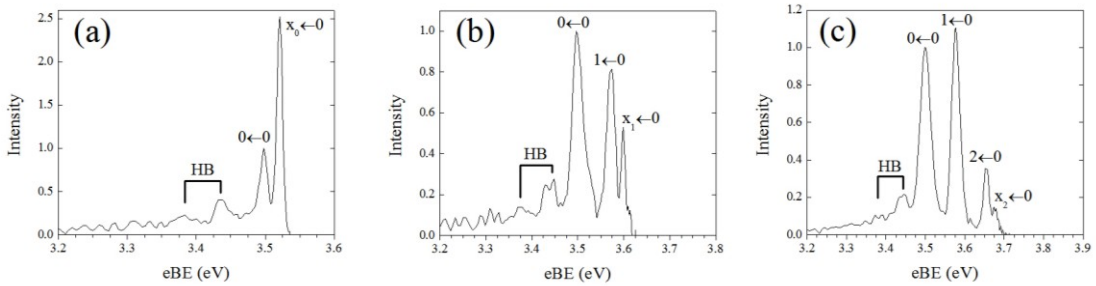

Figure 6.3: CuF_2^- energy domain spectra detached at a) 350 nm b) 342 nm c) 334 nm. The vibrational features labeled v'←0 (v' = 0,1,2) compose the vibrational progression seen in higher photon energy spectra, whereas the features labeled v'←0 (v' = x_0,x_1,x_2) are only observed through enhancement of the cross section near their respective thresholds. Spectra (a,b,c) represent the maxima in intensity deviations for the respective peaks x_0,x_1,x_2←0.

section relative to the eBE = 3.50 eV vibrational band at high eKEs, and therefore become unresolved and unnoticeable from instrumental broadening. The spectra of Figure 6.3 show the maxima for all three transitions x_0,x_1,x_2←0. The relative intensity strengths between these maxima are $x_0 > x_1> x_2$ ←0. Each of these transitions respectively lies ~20 meV higher in binding energy than the assigned vibrational transitions 0,1,2←0 [Figure 6.1(b)/Figure 6.3]. The similarities in the three features x_0,x_1,x_2←0 suggest a vibrational progression, for which a vibrational frequency (using the harmonic oscillator approximation) was measured to be 630±50 cm^{-1}. This is comparable to the previously reported lower energy 0,1,2←0 vibrational progression (630±30 cm^{-1}).

The anisotropy parameter for vibrational transitions with v′=0-2 was monitored as a function of the respective transition's eKE [Figure 6.4(a-c) (black circles)]. All transition PADs approach β=+1.5 at higher eKE values and trend slightly towards lower β values near their energetic thresholds. The PADs for each x_0,x_1,x_2←0 transition are also monitored for the short energy regions they were observable [Figure 6.4(a-c) (red circles)], and are compared with the known vibrational band v′=0,1,2 PADs in three

pairs: (x_0; v′=0), (x_1; v′=1), and (x_2; v′=2). Interestingly, they appear isotropic compared to their v′=0,1,2 counterparts at matching eKEs.

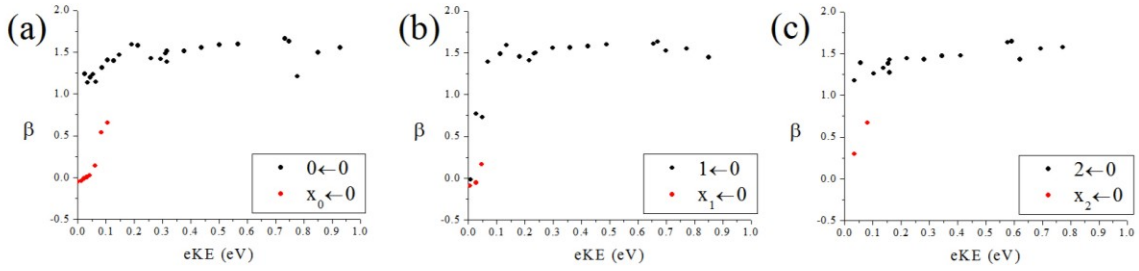

Figure 6.4: (a-c) CuF_2^- PADs for the vibrational channels v'←0 (v' = 0,1,2) (black circles) and the v'←0 (v' = x_0,x_1,x_2) transitions (red circles).

6.4 Discussion

6.4.1 CuF_2 Electronic State Assignments

A number of theoretical studies have been conducted on the neutral linear CuF_2 molecule [32,123,125,129-132]. Some of the earliest studies used self-consistent field methods [123,130] and concluded the ground state of CuF_2 was $^2\Sigma_g^+$ with an energetically close lying $^2\Pi_g$ state; however, inspired by studies that showed $CuCl_2$ has a $^2\Pi_g$ ground state [134,135], groups started to investigate whether more advanced computational techniques were required to accurately simulate the molecular orbital energies. Some groups concluded the $^2\Pi_g$ was the ground state of CuF_2 [131,132], but others remained set on a $^2\Sigma_g^+$ ground state [32,139]. Looking towards experimental data to resolve this conflict, an early high energy photoelectron spectroscopy study was able to develop an orbital energy diagram based upon their data [123], but unfortunately they were not able to resolve the energy spacing between the lowest lying states. Figure 6.5 shows the orbital energy diagram for the linear $^1\Sigma_g^+$ state for CuF_2^- (represented as $F^-Cu^+F^-$) based

on Ref[123] experimental data interpreted by Ref[136], and DFT calculations performed by our group. This assignment for the ground state closed-shell anion is in good agreement with previous theoretical studies [32,123,139]. Detachment from the $7\sigma_g^+$ orbital leaves the neutral in electronic state $^2\Sigma_g^+$, whereas detachment from the $2\pi_g$ orbital leaves it in electronic state $^2\Pi_g$; therefore, the uncertainty in the ordering of the $7\sigma_g^+$ and $2\pi_g$ orbitals is the direct reason for uncertainty in the ground state assignment. In order to assign features in our experimental observations, it becomes important to view the character of the orbitals in more detail.

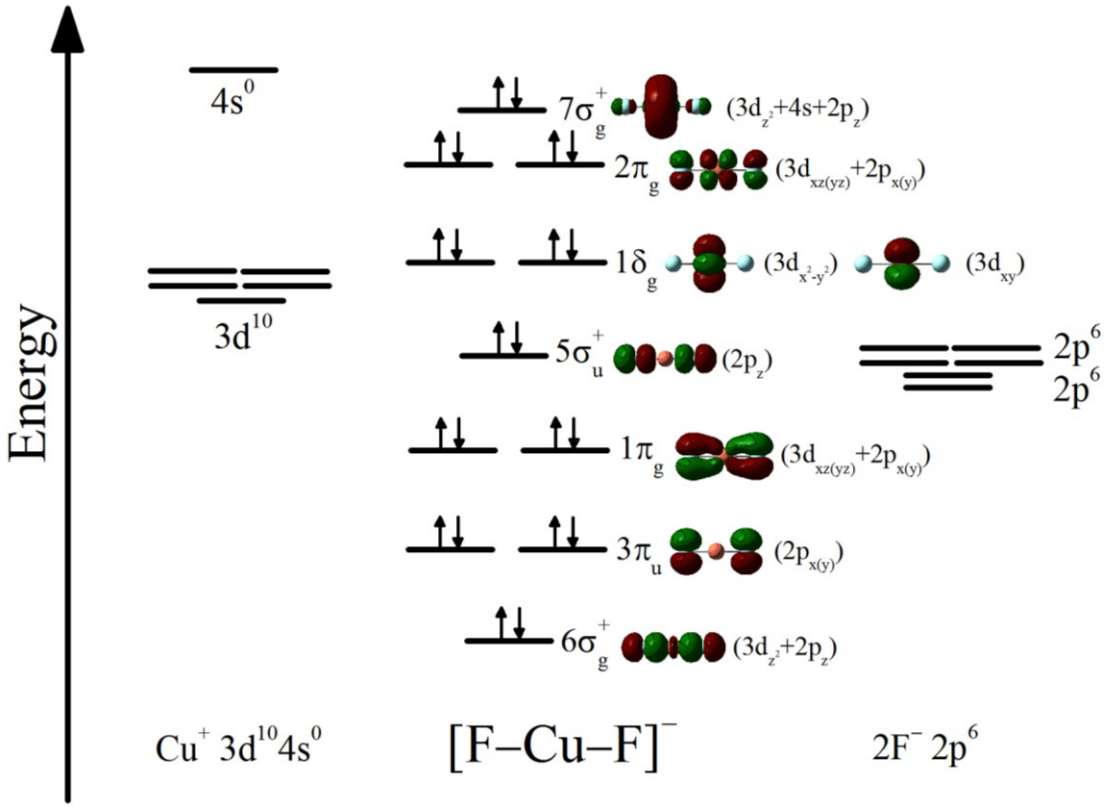

Figure 6.5: Molecular orbital (MO) diagram for CuF_2^- linear ground state anion ($X^1\Sigma^+$). Visual MOs provided to the right of diagram.

The $7\sigma_g^+$, $2\pi_g$, and $1\delta_g$ orbitals possess large 3d character from the Cu atom, while the $5\sigma_u^+$, $3\pi_u$ orbitals possess large 2p character from both F atoms. For specific details on the two highest lying orbitals, we performed a DFT calculation and population analysis of the anion. The $7\sigma_g^+$ is composed of a sizable contribution from the Cu $3d_{z^2}$ atomic orbital, with moderate contributions from Cu 4s, $3d_{x^2-y^2}$ atomic orbitals, and a small contribution from the F $2p_z$ atomic orbitals, while the $2\pi_g$ composition contains relatively equal contributions from both the Cu $3d_{xz(yz)}$ and F $2p_{x(y)}$. Recalling from Section 1.2.1, the PAD is sometimes referred to as the signature of the parent orbital; hence, observing the PAD for specific transitions directly gives information on the orbital from which the electron was detached, in this case either $7\sigma_g^+$ or $2\pi_g$.

There is one dominant vibrational progression in our energy spectra at higher photon energies. Figure 6.1 shows the spectrum at hν = 4.00 eV from which the resolved structure is in good agreement with the FC expectation and can be assigned to the linear CuF_2 symmetric stretching mode (630 cm^{-1}). At lower photon energies, additional transitions become resolved near their respective energetic thresholds [Figure 6.3, (x_0,x_1,x_2←0)], which seem to deviate from Wigner behavior at low eKEs relative to the 0←0 peak intensity. To gain insight on the transitions for this energy region we focus on the PAD. The PADs for all transitions in the main vibrational progression [Figure 6.4, (black circles)] rise immediately to $\beta \approx +1.5$ and remain near this value at high eKEs. The PADs for the other transitions [Figure 6.4, (red circles)] seem to start isotropic (β = 0) and slowly rise towards positive anisotropy values. These different trends in both PADs suggest the electrons are detached from separate orbitals.

Predicting the detachment PADs from the two orbitals, $7\sigma_g^+$ or $2\pi_g$, can be qualitatively accomplished by using the s and p model [75], previously applied in Chapter 3 to explain trends in CuO^- PADs. Figure 6.6 displays an outline of the model for the CuF_2^- transitions, $^2\Sigma_g^+ \leftarrow {}^1\Sigma_g^+$ and $^2\Pi_g \leftarrow {}^1\Sigma_g^+$, representing detachment from the $7\sigma_g^+$ and $2\pi_g$ orbitals respectively. The totally symmetric irreducible representation for the $D_{\infty h}$ point group is Σ_g^+ symmetry and the molecular frame dipole operators for the z and x/y orientations transform as Σ_u^+ and Π_u symmetries respectively. The allowed free electron symmetries correspond to laboratory frame p_z waves in all molecular orientations for detachment from the $7\sigma_g^+$ orbital, correlating to strong parallel detachment along the laser

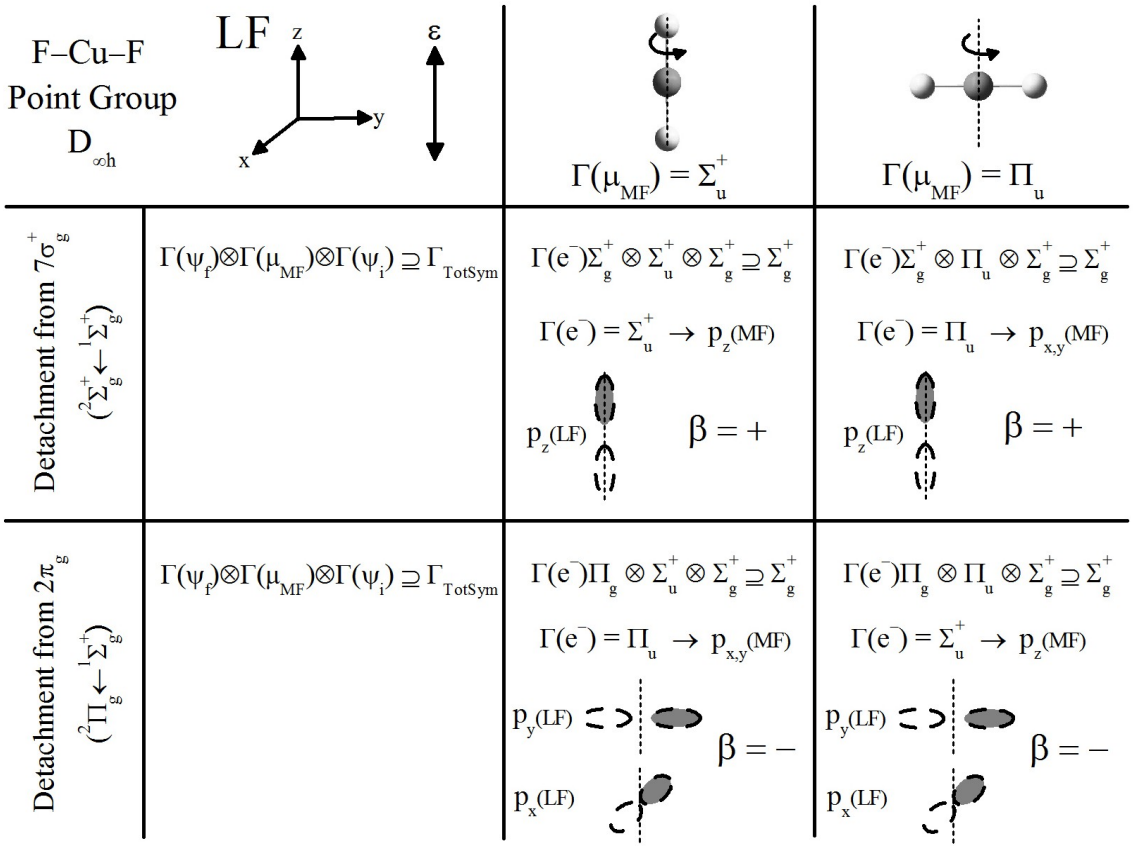

Figure 6.6: Predicted angular distributions, with respect to the laser polarization axis (ε), for detachment from two different orbitals of CuF_2^-, $7\sigma_g^+$ and $2\pi_g$, based on the s and p model [75]. The molecule is initially viewed in the molecular frame (MF) orientation, but the anisotropy (β) is interpreted from the laboratory frame (LF) z-axis, defined by ε.

polarization axis (positive β). For detachment from the $2\pi_g$ orbital, the allowed free electron symmetries correspond to laboratory frame p_x and p_y waves, correlating to strong perpendicular detachment along the laser polarization axis (negative β). The positive nature of the PAD for the vibrational progression (0,1,2←0) beginning at 3.50 eV [Figure 6.1(b)] suggests detachment from $7\sigma_g^+$ over $2\pi_g$.

To further gain insight on detachment, Table 6.1 provides charges on each atom from various theoretical studies of the anion and neutral ground states.

TABLE 6.1: Linear CuF_2 Atomic Charges

		F	Cu	F
Anion	Ref[129]	−0.86	+0.71	−0.86
Neutral	Ref[129]	−0.77	+1.55	−0.77
	Ref[132]	−0.70	+1.40	−0.70
	Ref[131]	−0.72	+1.44	−0.72

Removal of the excess electron from the anion takes away an average charge of 75% from the Cu atom and 25% from the collective F atoms, suggesting the detachment is mainly from an orbital with large Cu character. Combination of this charge analysis with the observed PAD, qualitatively described by the s and p model, for the vibrational progression beginning at 3.50 eV, we find the data is in good agreement with detachment from the $7\sigma_g^+$ orbital; hence, correlating to a ground state of $^2\Sigma_g^+$ for neutral CuF_2.

The assignment of the x_0,x_1,x_2←0 vibrational progression is less straightforward. By process of eliminating the $^2\Sigma_g^+$ state as a potential candidate for this progression, let us initially presume this progression to be associated with the electronic $^2\Pi_g$ state. One immediate problem with this assumption is the observed versus predicted trends in the PAD of the vibrational channels [Figure 6.4]. These transitions are only clearly observed during near threshold detachment, putting into question whether the recorded PAD for

this short energy region accurately represents direct detachment from the parent orbital. The sharp changes in the integral cross sections for the $x_0,x_1,x_2 \leftarrow 0$ channels near threshold are reminiscent of resonance effects, and deviations in PADs have been correlated with such phenomena for detachment from CuF^- in the previous chapter. This could account for differences between the predicted negative PAD trend from the s and p model [Figure 6.6] and the observed isotropic/slightly positive PAD [Figure 6.4].

A previous ESR experiment reported the asymmetric stretching mode of the $^{63}CuF_2$ $^2\Sigma_g^+$ state to be 769 cm^{-1}, but observed no other electronic transitions (from the $^2\Sigma_g^+$ ground state) within the energy range 0.036−3.72 eV, with the exception of the unexplored energy gap 0.62−1.364 eV [133]. They concluded, based on calculations and previous studies on $CuCl_2$, that the $^2\Pi_g$ state must lie near ~0.62 eV. The highest photon energy used in our experiments on CuF_2^- was 4.43 eV (280 nm), which corresponds to 0.93 eV above the $^2\Sigma_g^+$ ground state. With the exception of the $x_0,x_1,x_2 \leftarrow 0$ vibrational progression, no other electronic transitions were observed up to 0.93 eV, which disagrees with the ESR based assessment. Combining our experimental data with Ref[133], the only unexplored energy region above the ground state is 0.93−1.364 eV. Aside from this gap, it is also noticeable that the ESR study did not report data from 0−0.036 eV (above the $^2\Sigma_g^+$ state), in which our observed $x_0,x_1,x_2 \leftarrow 0$ transitions lie. Theoretical studies predict a wide range of energies for the $^2\Pi_g$ state, sometimes lying even below the $^2\Sigma_g^+$ state, which are highly method and basis set dependent. Of the studies which predicted $^2\Sigma_g^+$ as the ground state, one predicted $^2\Pi_g$ to lie 0.44−0.53 eV [32], while the other predicted an energy difference between 0.26−0.50 eV [139], both alluding to a close lying electronic state. In addition to the energies, the symmetric stretching mode

frequencies of the $^2\Pi_g$ state were calculated to be between 588−645 cm^{-1} [32] and 632−645 cm^{-1} [139], both comparable to our measured $x_0,x_1,x_2 \leftarrow 0$ frequency (630 cm^{-1}).

To better locate the $^2\Pi_g$ state, we turn to the experimental X-ray photoelectron spectra [123]. The He(I) and He(II) spectra show an ionization feature centered at 13.2 eV, which was attributed to ionization from the $7\sigma_g^+$ and $2\pi_g$ orbitals [136]. Even though this feature has a broad FWHM (~0.6 eV), it would still imply that the two orbitals must lie within 0−0.6 eV from each other. Hence, we conclude that the $^2\Pi_g$ state cannot lie in the region unexplored by either the ESR or our photodetachment experiments (0.93−1.364 eV).

Using our experimental findings and comparing to past ESR/XPES experiments [123,133] and theoretical studies [32,139], we conclude that the CuF_2 $x_0,x_1,x_2 \leftarrow 0$ vibrational progression [Figure 6.3] should be assigned to the $^2\Pi_g$ state lying ~20 meV above the $^2\Sigma_g^+$ ground state. Assigning this progression to the $^2\Pi_g$ state now allows for interpretation of the abnormal intensity variations seen in Figure 6.3.

6.4.1.1 Relative vibrational channel intensity fluctuations

The $^2\Pi_g \leftarrow {}^1\Sigma_g^+$ vibrational transitions ($x_0,x_1,x_2 \leftarrow 0$) [Figure 6.3] show similar behavior to detachment from CuO^- [Chapter 3], where the cross sections of certain vibrational transitions were enhanced over narrow excitation energy ranges. In the case of CuO^-, a dipole bound state (DBS) briefly captures the ejected electron prior to detachment. However, CuF_2 is a linear centrosymmetric molecule and the dipole moment is zero (i.e. the neutral molecule cannot support a DBS). The previous chapter on CuF^- reported deviations in the relative vibrational channel intensities, attributable to excitation to

electronic Feshbach resonances. In light of these observations, we performed a time-dependent DFT (TDDFT) calculation for CuF_2^-, using the same method and basis sets described in Section 6.3.1, and found many anion excited states lying near the calculated AEA = 3.56 eV (experimental AEA = 3.50 eV). Accounting for error in the TDDFT calculations, the two most likely candidates for possible Feshbach resonances close to the AEA are promotion of an electron from the $2\pi_g$ [Figure 6.5] to the lowest unoccupied molecular orbital (LUMO) (~3.39 eV), of σ_g^+ symmetry, and excitation of a $1\delta_g$ electron to the LUMO (~3.72 eV). These represent the absorption transitions $^1\Pi_g \leftarrow {}^1\Sigma_g^+$ and $^1\Delta_g \leftarrow {}^1\Sigma_g^+$ respectively. In order to interpret the observed intensity deviations in the $^2\Pi_g$ state, the one photon pathways for electronic detachment to the $^2\Pi_g$ state are shown in Equation 6.1:

$$\begin{aligned} CuF_2^-(X^1\Sigma_g^+) &\xrightarrow{h\nu} CuF_2(A'^2\,\Pi_g) + e^- && \text{(I)} \\ &\xrightarrow{h\nu} [CuF_2^-]^*(B^1\Pi_g) \longrightarrow CuF_2(A'^2\,\Pi_g) + e^- && \text{(II)} \\ &\xrightarrow{h\nu} [CuF_2^-]^*(C^1\Delta_g) \longrightarrow CuF_2(A'^2\,\Pi_g) + e^- && \text{(III)} \end{aligned} \qquad (6.1)$$

Pathway (I) represents direct detachment, while pathways (II) and (III) represent excitation to a temporary anion state (respectively $^1\Pi_g$ and $^1\Delta_g$) followed by autodetachment to the $^2\Pi_g$ state. For the autodetachment process to be feasible, a vibrational level of the CuF_2 $^2\Pi_g$ state must be near isoenergetic with a vibrational level of the excited anion state. Hence, the absorption cross section will be enhanced over narrow ranges of photon energies.

Based on the energy ranges these brief intensity fluctuations are observed, it is apparent the width of the resonance is relatively narrow, meaning the lifetime of the resonance is large. Although we have not measured the lifetimes, as we did in Chapter 3, we can still make assertions about the excited anion state from which autodetachment

occurs. Pathway (II) promotes an electron into the LUMO, an orbitally allowed transition ($\Delta\Lambda$=1), and produces an electronic hole in the $2\pi_g$ orbital [Figure 6.5]. Autodetachment of the electron in the LUMO produces the $^2\Pi_g$ state electronic configuration, without the need for electronic rearrangement. Alternatively, pathway (III) promotes an electron into the LUMO and produces an electronic hole in the $1\delta_g$ orbital [Figure 6.5]. Autodetachment from the LUMO would then involve rearrangement in the electronic configuration to produce the $^2\Pi_g$ state, corresponding to a longer lifetime than pathway (II). However, in pathway (III), the initial absorption to the $^1\Delta_g$ state is orbitally forbidden ($\Delta\Lambda\neq2$). Based on the above considerations we tentatively assign the $x_0,x_1,x_2\leftarrow0$ transitions to a vibrational progression associated with the $^2\Pi_g$ neutral state symmetric stretching mode. Further, we tentatively suggest that an excited ($^1\Pi_g$) anion state (based on $\Delta\Lambda$) plays a role in enhancing the absorption cross sections, and therefore detachment cross sections, for the $^2\Pi_g$ vibrational progression ($x_0,x_1,x_2\leftarrow0$).

The CuF_2 ground state $^2\Sigma_g^+$ sees no such intensity effects in the vibrational channels. The $0\leftarrow0$ transition for detachment from this state serves as our reference to observe the intensity fluctuations in the $^2\Pi_g$ vibrational channels ($x_0,x_1,x_2\leftarrow0$), so the effects could potentially go unnoticed. We find this unlikely, as the $^2\Sigma_g^+$ v'>0 channels show no effects relative to the v'=0 channel intensity. The more likely explanation is the resonant states are nearly isoenergetic with the $^2\Pi_g$ state, preferentially autodetaching to the closest lying neutral state; hence, seeing the intensity effects in the $^2\Pi_g$ state but not the $^2\Sigma_g^+$ ground state.

6.4.2 Superhalogen properties of CuF_n^- molecules

Recent theoretical studies on CuF_n^- clusters have predicted n≥2 clusters to possess superhalogen properties [125,129], indicating the addition of one F atom to CuF^- changes from non-superhalogen to superhalogen properties. No previous experimental studies have been performed on copper fluoride anions, but the work presented in this chapter is perfectly suitable to verify this assertion. Table 6.2 provides a comparison of theoretically calculated EAs and our experimental data:

TABLE 6.2: Comparison of EAs for CuF_n ($n \leq 2$)

Molecule		**EA (eV)**
CuF	Ref[125]	1.30
	Ref[129]	1.53
	Theoretical*	1.32
	Experiment*	1.271 (0.002)
CuF_2	Ref[125]	3.63
	Ref[129]	3.79
	Theoretical*	3.56
	Experiment*	3.498 (0.003)

*This work [Theoretical details: Section 5.4.1.1(CuF) & Section 6.3.1(CuF_2)]

Even though the calculated EAs for the first couple CuF_n molecules overestimate the experimental value, they are close to the experimental data. Superhalogen properties arise from the extra electron being delocalized over the ligand halogens; hence, increasing the EA of the molecule. It is clear that CuF_2 is very close to the superhalogen limit, possessing an EA higher than F (3.40 eV) but lower than Cl (3.61 eV). The definition of superhalogen is broad and based on the molecule having a higher EA than its atomic ligand (i.e. EA[CuF_2]>EA[F]), we conclude CuF_2^- is a superhalogen.

With this newly acquired information, trends in the EA of these molecular anions can be studied as the ligand halogen is altered. Experimental studies have reported $CuCl_2$ and $CuBr_2$ to have nearly identical EAs (4.35±0.05 eV) [122,137], and CuI_2 to have an EA of 4.26±0.01 eV [138]. All three species were reported to have ground states of $^2\Pi_g$. This a major difference to our experimental findings on CuF_2, which suggest $^2\Sigma_g^+$ is the ground state and possessing a significantly lower EA (~3.5 eV). The differences in EAs can be attributed to the atomic size of the ligands, causing larger spin-orbit effects for larger nuclei, shifting the $2\pi_g$ orbital higher in energy than the $7\sigma_g^+$ orbital [see Figure 6.5]. The $2\pi_g$ orbital processes significantly more π character than the $7\sigma_g^+$ orbital, for which the extra electron can become more delocalized over the ligands, raising the EA.

Trends in the EAs upon addition of more ligands around the central Cu atom has been theoretically investigated previously for $CuCl_n^-$ (n=1-5) [122] and CuF_n^- (n=1-6) [125]. According to theory, when n≥4 CuF_n^- cluster EAs exceed that of $CuCl_n^-$ clusters. This indicates that the effects from the size of the nuclei become less important allowing the electron to become more delocalized in the ligand framework. Thus far, experimental values presented here and in other works [122] seem to agree with theoretically calculated EAs, bringing a level of validity to these theoretical studies.

6.5 Summary

The first experimental evidence of the CuF_2 anion has been presented in the preceding sections. The ground state for neutral CuF_2 was determined to be $^2\Sigma_g^+$ with a close lying neutral excited state ($^2\Pi_g$) ~20 meV higher in energy. The vibrational progression of the $^2\Pi_g$ state [Figure 6.3, (x_0,x_1,x_2←0)] showed sharp increases in its

vibrational channels absorption cross sections near their respective channel thresholds. These resonance features were tentatively assigned as absorption to a temporary excited anion state ($^1\Pi_g$), whereupon the extra electron autodetaches to the neutral $^2\Pi_g$ state. The electronic resonance is assumed to preferentially autodetach to the $^2\Pi_g$ state based on the excited state lying nearly isoenergetic.

The superhalogen characteristics of CuF_2^- were examined and it was determined that the species is termed a "superhalogen", possessing an EA of 3.50 eV. This is found to be a relatively low EA in comparison to other copper dihalides, CuX_2^- (X = Cl, Br, I), in which the extra electron becomes more delocalized in the ligand framework as the ligand size is increased to a point. Based on the agreement between theoretical studies and our experimental data, this effect is suggested to diminish with a high number of ligands.

Chapter 7

Conclusion

In concluding remarks, this dissertation has provided the reader with a wealth of information on copper molecular anions containing oxygen and fluorine. The prior chapters have displayed the effectiveness of monitoring the PADs and relative intensities of vibrational transitions in relating to various electronic resonance phenomena, and also the combined use of frequency and time domain experiments to probe dissociation processes.

The copper oxide anion CuO^- provided interesting scattering dynamics on dipole bound state (DBS) resonances. Probed near the energy threshold region of the ground state neutral $^2\Pi$, a DBS was observed (using the relative intensities of vibrational channels) to lie near the threshold for the next highest vibrational level from the effected vibrational channel. Lifetimes of these resonances suggested that electronic detachment occurred on the timescale of nuclear motion. The ability to detect such non-adiabatic processes and their resonance lifetimes shows the effectiveness of using tunable laser sources, and has served as a major advantage when studying electron-dipole interactions.

Experimental work on linear copper dioxide anion CuO_2^- showed the potential for combining frequency and time domain experiments to study dissociation reaction

dynamics. The linear isomer anion was found to dissociate to Cu^-, via selective isomer isolation in our source, and maximum production of ion fragments was found to take ~150 ps, giving a timescale for dissociation. This relatively long timescale is indicative of a substantial barrier to dissociation and possibility of interstate coupling after initial excitation, which correlates well with the assertion that the starting linear configuration is excited to a relatively low energy dissociative channel and exits the channel with fragments $Cu^- + O_2$. The dissociation dynamics associated with this anion isomer are admittedly unexpected, but through rigorous analysis using nanosecond and femtosecond technology we showed the underlying details behind this anion dissociation. There have been several other metal oxides that are known to produce dissociative fragments reported in the literature [48,49], and we hope our findings for linear CuO_2^- initiate both an experimental and theoretical effort for further details on dissociation pathways for other anionic transition metal complexes.

To the best of the author's knowledge, the results presented in Chapters 5 & 6 are the first experimental data reported for copper fluoride anions, which will hopefully spark interest in the X-ray/vacuum UV photoelectron community to experimentally observe the predicted high EAs for larger copper fluoride anions CuF_n^- ($n \geq 3$). Aside from characterization of these species, it was also discovered that both anions CuF_n^- ($n = 1,2$) possessed anionic excited states exceeding the energy of the neutral ground state. Excitation to these excited states allowed for temporary capture of an electron before relaxation by coupling to the electronic continuum, resulting in electron detachment and electronic rearrangement in the residual species. We have shown previously that the photoelectron angular distributions (PADs) are very sensitive to such processes, but

proved that monitoring relative vibrational channel cross sections can also serve as a more quantitative technique to follow these pathways.

7.1 Future Directions

The results contained in this dissertation show the effectiveness of negative ion photoelectron imaging and how it can be a powerful tool for characterization of chemical structure, probing resonances, and monitoring reaction dynamics. With this knowledge, the possible experimental directions one can take are seemingly endless. The method of generation for these copper based molecular anions alone provides the user with an effective method for generating other metal based anions by simply altering the cathode composition, but more importantly it provides a safe and effective method for generating fluorine based anions. Chapters 5 & 6 presented the first ever experiments conducted on copper fluoride anions, but this is just breaching the surface for the capabilities of the discharge source.

7.1.1 Various Other Metal Based Molecular Anions

Figure 2.3 showed the complexity of the mass spectrum for a copper cathode with pure oxygen flowing through the source. With only two stable copper isotopes (^{63}Cu & ^{65}Cu) and oxygen/fluorine being the only elements present in the source, there appears to be no shortage of mixtures in the mass spectrum. Of the peaks listed in Figure 2.3, other anions that have been observed include $CuOF^-$ and CuO_2F^-. It is important to point out that these mixed halogen, chalcogen Cu anions have not been studied previously and therefore have no structural characteristic assignments. Judging from our source

generation of CuO_2^- and the relatively high binding energies (respectively 3.14 & 3.09 eV), it would be appropriate to assume the transition metal is semi-centralized in the molecular structures, however, further analysis is required to make any additional assertions.

Aside from using copper as the cathode, our group has already previously explored a variety of metal cathodes with moderate success. Upon initial experimental testing of the discharge apparatus, metal anions ranging from Ag, Ni, Zn, and W were generated within the source. As a comparison to CuF^-, altering the metal atom to Ag would be interesting to study the changes in dynamical effects from the size of the transition metal atom, as both Cu and Ag have isoelectronic valence configurations. Alternatively, one can also modify the ligand of choice. An emerging field in the photoelectron community is the study of a new class of molecular anions termed "hyperhalogens" [121,140]. Like the superhalogens discussed in Chapter 6, the hyperhalogens contain ligands for which the electron can become delocalized, raising the EA of the species. The difference lies in the choice of ligands, where in a superhalogen the ligand is atomic, the hyperhalogen ligand is polyatomic. The dynamics of such species are largely unexplored, and if the study presented in this dissertation on copper fluorides reflects similar trends in super/hyperhalogens, it would show great promise for possible high energetic resonances within these complexes.

References

[1] A.T.J.B. Eppink and D.H. Parker, Review of Scientific Instruments **68**, 3477 (1997).

[2] E.W. Hansen and P. Law, J. Opt. Soc. Am. A **2**, 510 (1985).

[3] V. Dribinski, A. Ossadtchi, V. A. Mandelshtam, and H. Reisler, Review of Scientific Instruments **73**, 2634 (2002).

[4] J.L. Hall, The Journal of Chemical Physics **48**, 943 (1968).

[5] J. Cooper and R.N. Zare, Journal of Chemical Physics **48**, 942 (1968).

[6] C.G. Bailey, C.E.H. Dessent, M.A. Johnson, and K.H. Bowen, Journal of Chemical Physics **104**, 6976 (1996).

[7] M. Van Duzor, J. Wei, F. Mbaiwa, and R. Mabbs, The Journal of Chemical Physics **131**, 204306 (2009).

[8] M. Van Duzor, F. Mbaiwa, J. Lasinski, D. Dao, N. Holtgrewe, and R. Mabbs, The Journal of Chemical Physics **134**, 184315 (2011).

[9] F. Mbaiwa, M. Van Duzor, J. Wei, and R. Mabbs, Journal of Physical Chemistry A **114**, 1539 (2010).

[10] S.T. Manson and A.F. Starace, Review of Modern Physics **54**, 389 (1982).

[11] P.M. Morse, Physical Review **34**, 57 (1929).

[12] M. Born and J. R. Oppenheimer, Ann. Physik **84**, 457 (1927).

[13] J.C. Rienstra-Kiracofe, G.S. Tschumper, H.F.S. Iii, S. Nandi, and G.B. Ellison, Chem. Rev. **102**, 231 (2002).

[14] D.A. McQuarrie, Quantum Chemistry 2nd ed.; University Science Books: Sausalito, California, 466-470, 2008.

[15] O.H. Crawford and W. R. Garrett, J. Chem. Phys. **66**, 4968 (1977).

[16] O.H. Crawford, Mol. Phys. **20**, 585 (1971).

[17] R.N. Zare, Angular momentum: understanding spatial aspects in chemistry and physics; Wiley: New York, 1988.

[18] G. Herzberg, Molecular spectra and molecular structure: Spectra of diatomic molecules 2nd ed.; Krieger: Malabar, FL, 1989; Vol 1.

[19] G. Herzberg, Atomic Spectra and Atomic Structure (Dover Publications, 1944), p. 135.

[20] J.W. Farley, Physical Review A **40**, 6286 (1989).

[21] E.P. Wigner, Phys. Rev. **73**, 1002 (1948).

[22] H. Hotop, T. A. Patterson and W. C. Lineberger, J. Chem. Phys. **60**, 1806 (1974).

[23] P. A. Schulz, R. D. Mead, P. L. Jones and W. C. Lineberger, J. Chem. Phys. **77**, 1153 (1982).

[24] B. K. Janousek and J. I. Brauman, J. Chem. Phys. **72**, 694 (1980).

[25] E. Fermi and E. Teller, Phys. Rev. **72**, 399 (1947).

[26] A. S. Wightman, Phys. Rev. **77**, 521 (1950).

[27] M. Gutowski, P. Skurski, A. I. Boldyrev, J. Simons, and K. D. Jordan, Phys. Rev. A **54**, 1906 (1996).

[28] M. Gutowski and P. Skurski, J. Chem. Phys. **107**, 2968 (1997).

[29] W. R. Garrett, J. Chem. Phys. **77**, 3666 (1982).

[30] J.H. Hendricks, S.A. Lyapustina, H.L. de Clercq, J.T. Snodgrass, and K.H. Bowen, J. Chem. Phys. **104**, 7788 (1996).

[31] S. Midda, N.C. Bera, I. Bhattacharyya, and A. K. Das, Journal of Molecular Structure: THEOCHEM **725**, 251 (2005).

[32] P. Schwerdtfeger, P.D.W. Boyd, G.A. Bowmaker, and L.P. Aldridge, Structural Chemistry **1**, 405 (1990).

[33] D.M. Neumark, Ann. Rev. Phys. Chem. **52**, 255 (2001).

[34] G. Ganteför, S. Kraus, and W. Eberhardt, Journal of Electron Spectroscopy and Related Phenomena **88-91**, 35 (2009).

[35] R. Mabbs, K. Pichugin, and A. Sanov, The Journal of Chemical Physics **122**, 174305 (2005).

[36] M.T. Zanni, B.J. Greenblatt, A. V. Davis, and D.M. Neumark, The Journal of Chemical Physics **111**, 2991 (1999).

[37] L. Sheps, E.M. Miller, S. Horvath, M.A. Thompson, R. Parson, A.B. McCoy, and W.C. Lineberger, Science **328**, 220 (2010).

[38] D. H. Parker and A. T. J. B. Eppink, J. Chem. Phys. **107**, 2357 (1997).

[39] D. L. Osborn, D. J. Leahy, D. R. Cyr and D. M. Neumark, J. Chem. Phys. **104**, 5026 (1996).

[40] W. C. Lineberger and M. A. Johnson, Techniques for the Study of Ion Molecule Reactions, Volume 20, Chapter 11, pages 591–631, (Wiley, New York, 1982).

[41] G. Ganteför, H. R. Siekmann, H. O. Lutz, and K. H. Meiwes-Broer,, Chem. Phys. Lett. **165**, 293 (1990).

[42] C. Cha, G. Ganteför, and W. Eberhardt, Rev. Sci. Instrum. **63**, 5661 (1992).

[43] D. W. Chandler and P. Houston, J. Chem. Phys. **87**, 1445 (1987).

[44] L. A. Posey, M. J. Deluca, and M. A. Johnson, Chem. Phys. Lett. **131**, 170 (1986).

[45] R. E. Carley, E. Heesel, and H. H. Fielding, Chem. Soc. Rev. **34**, 949 (2005).

[46] Idaho National Engineering and Environmental laboratory, SIMION 3D VERSION 7.0 (SOFTWARE FOR ION OPTICS), Published by Bechtel BWXT Idaho, LLC (2000).

[47] C.N.R. Rao, Annual Review of Physical Chemistry **40**, 291 (1989).

[48] H. Wu and L.-S. Wang, The Journal of Chemical Physics **107**, 16 (1997).

[49] H. Wu, S.R. Desai, and L. Wang, Journal of Physical Chemistry A **101**, 2103 (1997).

[50] V.D. Moravec, S.A. Klopcic, B. Chatterjee, and C.C. Jarrold, Chemical Physics Letters **341**, 313 (2001).

[51] D.H. Andrews, A.J. Gianola, and W.C. Lineberger, The Journal of Chemical Physics **117**, 4074 (2002).

[52] H. Zhai, B. Kiran, L. Cui, X. Li, D.A. Dixon, and L. Wang, Journal of the American Chemical Society **126**, 16134 (2004).

[53] Y. Gong, M. Zhou, and L. Andrews, Chemical Reviews **109**, 6765 (2009).

[54] E.L. Uzunova, The Journal of Physical Chemistry A **115**, 1320 (2011).

[55] L. Wang, H. Wu, S. Desai, and L. Lou, Physical Review B: Condensed Matter **53**, 8028 (1996).

[56] G. V Chertihin, L. Andrews, and C.W. Bauschlicher, Journal of Physical Chemistry A **101**, 4026 (1997).

[57] Y. Pouillon and C. Massobrio, Applied Surface Science **226**, 306 (2004).

[58] G.-T. Bae, B. Dellinger, and R.W. Hall, The Journal of Physical Chemistry A **115**, 2087 (2011).

[59] P. V. Madhavan and M.D. Newton, The Journal of Chemical Physics **83**, 2337 (1985).

[60] M.L. Polak, M.K. Gilles, J. Ho, and W.C. Lineberger, Journal of Physical Chemistry **95**, 3460 (1991).

[61] H. Xian, Z.X. Cao, X. Xu, X. Lu, and Q.E. Zhang, Chemical Physics Letters **326**, 485 (2000).

[62] L.F.A. Ferra, O. Roberto-Neto, and F.B.C. Machado, International Journal of Quantum Chemistry **108**, 2512 (2008).

[63] J.S. Shirk and A.M. Bass, The Journal of Chemical Physics **52**, 1894 (1970).

[64] O. Appelblad, A. Lagerqvist, Y. Lefebvre, B. Pinchemel, and J. Schamps, Physica Scripta **18**, 125 (1978).

[65] A. J. Merer, Annual Review of Physical Chemistry **40**, 407-438 (1989).

[66] K. M. Ervin, J. Ho, and W. C. Lineberger, J. Phys. Chem. **92**, 5405 (1988).

[67] K. P. Huber and G. Herzberg, "Molecular Spectra & Molecular Stucture: Volume 4" 1979.

[68] S. Tauro and K. Liu, Journal of Physics B: Atomic, Molecular and Optical Physics **41**, 225001 (2008).

[69] H. Chen and W. Sheu, Journal of the American Chemical Society **122**, 7534 (2000).

[70] Ugo Varetto, MOLEKEL 5.4; Swiss National Supercomputing Centre: Lugano (Switzerland).

[71] P. Skurski, M. Gutowski, and J. Simons, International Journal of Quantum Chemistry **80**, 1024 (2000).

[72] a) Cu atom basis set: N.B. Balabanov and K.A. Peterson, J. Chem. Phys. **123**, 064107 (2005); N.B. Balabanov and K.A. Peterson, J. Chem. Phys. **125**, 074110 (2006); b) O atom basis set: T.H. Dunning Jr., J. Chem. Phys. **90**, 1007 (1989).

[73] F. Mbaiwa, D. Dao, N. Holtgrewe, J. Lasinski, and R. Mabbs, The Journal of Chemical Physics **136**, 114303 (2012).

[74] X. Zhuang, S.E. Frey, and T.C. Steimle, The Journal of Chemical Physics **132**, 234312 (2010).

[75] E. Surber, R. Mabbs, and A. Sanov, Journal of Physical Chemistry A **107**, 8215 (2003).

[76] M. J. Frisch, G. W. Trucks, H. B. Schlegel, G. E. Scuseria, M. A. Robb, J. R. Cheeseman, J. A.Montgomery, Jr., T. Vreven, K. N. Kudin, J. C. Burant, J. M. Millam, S. S. Iyengar, J. Tomasi, V. Barone, B. Mennucci, M. Cossi, G. Scalmani, N. Rega, G. A. Petersson, H. Nakatsuji, M. Hada, M. Ehara, K. Toy- ota, R. Fukuda, J. Hasegawa, M. Ishida, T. Nakajima, Y. Honda, O. Kitao, H. Nakai, M. Klene, X. Li, J. E. Knox, H. P. Hratchian, J. B. Cross, V. Bakken, C. Adamo, J. Jaramillo, R. Gomperts, R. E. Stratmann, O. Yazyev, A. J. Austin, R. Cammi, C. Pomelli, J. W. Ochterski, P. Y. Ayala, K. Morokuma, G. A. Voth, P. Salvador, J. J. Dannenberg, V. G. Zakrzewski, S. Dapprich, A. D. Daniels, M. C. Strain, O. Farkas, D. K. Malick, A. D. Rabuck, K. Raghavachari, J. B. Foresman, J. V. Ortiz, Q. Cui, A. G. Baboul, S. Clifford, J. Cioslowski, B. B. Stefanov, G. Liu, A. Liashenko, P. Piskorz, I. Komaromi, R. L. Martin, D. J. Fox, T. Keith, M. A. Al-Laham, C. Y. Peng, A. Nanayakkara, M. Chal- lacombe, P. M. W. Gill, B. Johnson, W. Chen, M. W. Wong, C. Gonzalez and J. A. Pople, Gaussian 03, Revision C.02, Gaussian, Inc.,Wallingford, CT, 2004.

[77] F. Turecek, Mass Spectrometry Reviews **26**, 563 (2007).

[78] H. Yamauchi and M. Karppinen, Materials Science and Engineering B **54**, 92 (1998).

[79] S. Chatterjee, S.S. Weng, I.P. Hong, C.F. Chang, H.D. Yang, and J. Lin, Physica C **312**, 55 (1999).

[80] I.I. Amelin, JETP Letters **70**, 23 (1999).

[81] A.L. Kuzemsky and I.G. Kuzemskaya, Physica C **383**, 140 (2002).

[82] D.E. Tevault, The Journal of Chemical Physics **76**, 2859 (1982).

[83] G.A. Ozin, S.A. Mitchell, and J. Garcia-prietos, Journal of the American Chemical Society **105**, 6399 (1983).

[84] V.E. Bondybey and J.H. English, The Journal of Physical Chemistry **88**, 2247 (1984).

[85] H. Wu, S.R. Desai, and L. Wang, Journal of Chemical Physics **103**, 8 (1995).

[86] G.L. Gutsev, B.K. Rao, and P. Jena, Journal of Physical Chemistry A **104**, 11961 (2000).

[87] T. Baruah, R.R. Zope, and M.R. Pederson, Physical Review A **69**, 1 (2008).

[88] K. Deng, J. Yang, L. Yuan, and Q. Zhu, The Journal of Chemical Physics **111**, 1477 (1999).

[89] Y. Pouillon, C. Massobrio, and M. Celino, Computational Materials Science **17**, 539 (2000).

[90] C.E. Brown, S.A. Mitchell, and P.A. Hackett, Journal of Physical Chemistry **95**, 1062 (1991).

[91] S.A. Mitchell, in Gas-Phase Metal Reactions, edited by A. Fontijn (Elsevier, Amsterdam, 1995), p. 227.

[92] R.C. Bilodeau, M. Scheer, and H.K. Haugen, J. Phys. B: At. Mol. Opt. Phys. **31**, 3885 (1998).

[93] V.I. Vedeneyev, L.V. Gurvich, V.N. Kondrat'yev, V.A. Medvedev, and L.Ye. Frankevich, Bond Energies, Ionization Potentials and Electron Affinities (St. Martin's Press, New York, 1962).

[94] Y. Pouillon and C. Massobrio, Chemical Physics Letters **331**, 290 (2000).

[95] Y. Mochizuki, U. Nagashima, S. Yamamoto, and H. Kashiwagi, Chem. Phys. Lett. **164**, 225 (1989).

[96] C.W. Bawchlicher, S.R. Langhoff, H. Partridge, and M. Sodupe, Journal of Physical Chemistry **97**, 856 (1993).

[97] D. Sulzle, H. Schwarz, K. H. Moock, and J. K. Terlouw, Int. J. Mass Spectrom. Ion Processes **108**, 269 (1991).

[98] J. Hasegawa, K. Pierloot, and O. Roos, Chemical Physics Letters **335**, 503 (2001).

[99] T.-K. Ha and M.T. Nguyen, Journal of Physical Chemistry **89**, 5569 (1985).

[100] T. Baruah, R. Zope, and M. Pederson, Physical Review A **69**, 023201 (2004).

[101] J. Hrušák, W. Koch, and H. Schwarz, The Journal of Chemical Physics **101**, 3898 (1994).

[102] L. Hoeft, T. Tiemann, Zeitschrift fur Naturforschung **25$_a$**, 35 (1970). via K.P. Huber, G. Herzberg, Molecular Spectra and Molecular Structure Vol 4, (1979).

[103] T. Honerjager, Zeitschrift fur Naturforschung **29$_a$**, 1919 (1970). via K.P. Huber, G. Herzberg, Molecular Spectra and Molecular Structure Vol 4, (1979).

[104] (Cu basis set) N.B. Balabanov and K.A. Peterson, J. Chem. Phys. **123**, 064107 (2005).

[105] M. Guichemerre, G. Chambaud, and H. Stoll, Chemical Physics **280**, 71 (2002).

[106] F. Ahmedi, R.F. Barrow, A.H. Chojnickii, C. Dufours, and J. Schamps, J. Phys. B: At. Mol. Phys. **15**, 3801 (1982).

[107] P. Baltayan, F. Hartmann, J.C. Pebay-Peyroula, and N. Sadeghi, Chem. Phys. **120,** 123 (1988).

[108] Y. Shao, L. Fusti-Molnar, Y. Jung, J. Kussman, C. Ochsenfeld, S. T. Brown, A. T. B. Gilbert, L. V. Slipchenko, S. V. Levchenko, D. P. O'Neill, R. A. DiS- tasio, Jr., R. C. Lochan, T.Wang, G. J. O. Beran, N. A. Besley, J. M. Herbert, C. Y. Lin, T. V. Voorhis, S. H. Chein, A. Sodt, R. P. Steele, V. A. Rassolov, P. E. Maslen, P. P. Korambath, R. D. Adamson, B. Austin, J. Baker, E. F. C. Byrd, H. Daschel, R. J. Doerksen, A. Dreuw, B. D. Dunietz, A. D. Dutoi, T. R. Furlani, S. R. Gwaltney, A. Heyden, S. Hirata, C. P. Hsu, G. Kedziora, R. Z. Khaliullin, P. Klunzinger, A. M. Lee, M. S. Lee, W. Liang, I. Lotan, N. Nair, B. Peters, E. I. Proynov, P. A. Pieniazek, Y. M. Rhee, J. Ritchie, E. Rosta, C. D. Sherrill, A. C. Simmonett, J. E. Subotnik, H. L. Woodcock III, W. Zhang, A. T. Bell, A. K. Chakraborty, D. M. Chipman, F. J. Keil, A. Warshel, W. J. Hehre, H. F. Schaefer III, J. Kong, A. I. Krylov, P. M. W. Gill, M. Head-Gordon, Z. Gan, Y. Zhao, D. Schultz, D. G. Truhlar, E. Epi- fanovsky, C. M. Oana, R. Baer, B. R. Brooks, D. Casanova, J. D. Chai, C. L. Cheng, C. Cramer, D. Crittenden, A. Ghysels, G. Hawkins, E. G. Hohenstein, C. Kelley, W. Kurlancheek, D. Liotard, E. Livshits, P. Manohar, A. Marenich, D. Neuhauser, R. Olson, M. A. Rohrdanz, K. S. Thanthiriwatte, A. J. W. Thom, V. Vanovschi, C. F. Williams, Q. Wu, and Z. Q. You, Q-CHEM, Qchem, Inc., Pittsburg, PA, 2007.

[109] Q-Chem User's Manual Version 4.0, Sept. 2011, pg. 259.

[110] M. Van Duzor, J. Wei, F. Mbaiwa, and R. Mabbs, J. Chem. Phys. **133**, 144303 (2010).

[111] F. Mbaiwa, J. Wei, M. Van Duzor, and R. Mabbs, J. Chem. Phys. **132**, 134304 (2010).

[112] F. Wang and T.C. Steimle, The Journal of Chemical Physics **132**, 054301 (2010).

[113] C. Koukounas and A. Mavridis, The Journal of Physical Chemistry A **112**, 11235 (2008).

[114] C.C. Fang and J.M. Parson, The Journal of Chemical Physics **95**, 6413 (1991).

[115] P. Baltayan, F. Hartmann, I. Hikmet, and N. Sadeghi, The Journal of Chemical Physics **97**, 5417 (1992).

[116] N. Barttlett, Proceedings of the Chemical Society, London, 218 (1962).

[117] G. L. Gutsev and A. I. Boldyrev, Chem. Phys. **56**, 277 (1981).

[118] K. Pradhan, G.L. Gutsev, and P. Jena, The Journal of Chemical Physics **133**, 144301 (2010).

[119] Y. Gong and L. Andrews, Inorganic Chemistry **51**, 667 (2012).

[120] C.J. Evans and M.C.L. Gerry, The Journal of Chemical Physics **112**, 9363 (2000).

[121] M. Willis, M. Götz, A.K. Kandalam, G.F. Ganteför, and P. Jena, Angewandte Chem (International Ed. in English) **49**, 8966 (2010).

[122] Y.J. Ko, H. Wang, K. Pradhan, P. Koirala, a K. Kandalam, K.H. Bowen, and P. Jena, The Journal of Chemical Physics **135**, 244312 (2011).

[123] J.M. Dyke, N.K. Fayad, G.D. Josland, and A. Morris, J. C. S. Faraday II **76**, 1672 (1980).

[124] L.F.A. Ferra, O. Roberto-Neto, and F.B.C. Machado, International Journal of Quantum Chemistry **108**, 2512 (2008).

[125] Q. Wang, Q. Sun, and P. Jena, The Journal of Chemical Physics **131**, 124301 (2009).

[126] T. E. Sharp and H. M. Rosenstock, J. Chem. Phys. **41**, 3453 (1964).

[127] F. Duschinsky, Acta Physicochimica U.R.S.S. **7**, 551 (1937).

[128] P. Chen, "Photoelectron Spectroscopy of Reactive Intermediates; in Unimolecular and Bimolecular Reactions Dynamics" (Ng, C.-Y., Baer, T. and Powis, I., eds.), John Wiley and Sons, Chichester, USA, Chapter 8, 371–425 (1994).

[129] P. Koirala, M. Willis, B. Kiran, A.K. Kandalam, and P. Jena, The Journal of Physical Chemistry C **114**, 16018 (2010).

[130] P. Correa de Mello, M. Hehenberger, S. Larsson, and M. Zerner, Journal of the American Chemical Society **102**, 1278 (1980).

[131] C.W. Bauschlicher and B.O. Roos, The Journal of Chemical Physics **91**, 4785 (1989).

[132] S.G. Wang and W.H.E. Schwarz, The Journal of Chemical Physics **109**, 7252 (1998).

[133] P.H. Kasai, E.B. Whipple, and W. Weltner, The Journal of Chemical Physics **44**, 2581 (1966).

[134] I.R. Beattie, J.M. Brown, P. Crozet, A.J. Ross, and A. Yiannopoulou, Inorganic Chemistry **36**, 3207 (1997).

[135] M.P. Barnes, R.T. Carter, N.M. Lakin, and J.M. Brown, Journal of the Chemical Society, Faraday Transactions **89**, 3205 (1993).

[136] L. Benco, S. Biskupic, and R. Boca, Journal of Electron Spectroscopy and Related Phenomena **43**, 1 (1987).

[137] X.-B. Wang, L.-S. Wang, R. Brown, P. Schwerdtfeger, D. Schröder, and H. Schwarz, The Journal of Chemical Physics **114**, 7388 (2001).

[138] Y.-L. Wang, X.-B. Wang, X.-P. Xing, F. Wei, J. Li, and L.-S. Wang, The Journal of Physical Chemistry A **114**, 11244 (2010).

[139] S.Y. Shashkin and W.A. Goddard III, The Journal of Physical Chemistry **90**, 255 (1986).

[140] D. Samanta, M.M. Wu, and P. Jena, Inorganic Chemistry **50**, 8918 (2011).